Imaging Upper Mantle Discontinuities Using Long Period Seismic Data

by

Ramin Mohammad Hosseini Dokht

A thesis submitted in partial fulfillment of the requirements for the degree of

Doctor of Philosophy
in
Geophysics

Department of Physics

University of Alberta

Abstract

Mantle reflectivity structure provides critical information on the temperature and composition of the mantle. So far, these structures are obtained by independent analyses of amplitudes and timing information of reflected and converted seismic phases at mantle discontinuities. These approaches are limited due to their inherent trade-off between velocity and gradient zone depth. This thesis aims to provide high resolution, novel imaging methods based on a nonlinear inversion method and wave spectral characteristics. Substantially improved data constrains, combined with increased imaging resolution and accuracy from this thesis, offer new insights into the process and effects of subduction (both present and past) on mantle stratification, fluid content and magmatism along the major convergent margins.

We explore the regional variations of the 410 km and 660 km discontinuities by careful analyses of the underside reflected S-wave energy (SS precursors) from mantle interfaces using nonlinear, simultaneous inversions of shear velocity and discontinuity topography. We find that the 410 km and 660 km discontinuity depths are strongly anti-correlated if the dipping angles of the non-vertical structures were taken into account. Beneath the volcanic centers in Northeast China, our simultaneous solutions provide compelling evidence for the source of deep-rooted mantle melting in association with the dehydration process of the stagnant Pacific slab.

An independent study using Singular Spectrum Analysis (SSA) for random noise removal and reconstruction of missing traces shows a significant enhancement of signals associated with mantle conversions beneath southwestern Canada. In addition to strong conversions from the transition zone phase boundaries, strong signals from the mid-transition zone reflectors can also be identified.

Finally, our results from pre-stack depth migration of precursory arrivals reveal small-sale variations (<500 km) on the discontinuity topography, due to the focusing of the diffracted energy to its true position. In Southeast Asia, the discontinuity depth measurements indicate maximum undulations of ± 40 km on both transition zone discontinuities along the Sunda and Banda arcs. The correlation between the discontinuity depths and previously reported seismic velocities suggests that the upper mantle phase boundaries are thermally, rather than compositionally, controlled.

Preface

Chapter 2 of this thesis has been published as: Dokht, R. M., Gu, Y. J., & Sacchi, M. D. (2016), Waveform inversion of SS precursors: An investigation of the northwestern Pacific subduction zones and intraplate volcanoes in China, *Gondwana Research*, **40**, 77−90. I was responsible for data collection and analysis as well as manuscript preparation. Y. J. Gu and M. D. Sacchi were the supervisory authors and were involved with concept formation and assisted with manuscript preparation.

Chapter 3 of this thesis has been previously published as: Dokht, R. M., Gu, Y. J., & Sacchi, M. D. (2016), Singular Spectrum Analysis and its applications in mapping mantle seismic structure, *Geophysical Journal International*, ggw473, doi: 10.1093/gji/ggw473. I was responsible for data collection and analysis as well as manuscript preparation. Y. J. Gu and M. D. Sacchi were the supervisory authors and were involved with concept formation and assisted with manuscript preparation.

Chapter 4 of this thesis is an original work and will be published at a later date.

I dedicate this thesis to my dear wife and my beloved parents.

Acknowledgements

First, I would like to express my sincere gratitude to my advisor Dr. Yu Jeffrey Gu for his patience, motivation, guidance and continuous support during the time of research and writing this thesis. I could not have imagined having this thesis finished without his great supervision.

I also would like to thank Prof. Mauricio D. Sacchi for his unconditional support and academic advice during the course of my research.

I appreciate the members of my committee: Prof. Vadim A. Kravchinsky, Prof. Aibing Li, Dr. Jeffrey Kavanaugh, and Prof. Douglas R. Schmitt, for their insightful recommendations, which helped us to improve the quality of this thesis.

I would like to express special thanks to my colleagues and friends including Yunfeng Chen, Ruijia Wang, Yuanyin Zhang, Nasser Kazemi, Yoones Vaezi, Reza Malehmir, and Simon Schneider for the helpful scientific discussions, insightful comments and productive criticism.

Thanks to my soccer teammates, especially our coach MK, who made the past four years in Edmonton more enjoyable than I could have ever imagined.

The present thesis is partially supported by the Helmholtz-Alberta Initiative (HAI grant RES0019262) and Faculty of Science Dean's Excellence Award.

The facilities of IRIS Data Services, and specifically the IRIS Data Management Center, were used for access to waveforms, related metadata, and/or derived products used in this study. IRIS Data Services are funded through the Seismological

Facilities for the Advancement of Geoscience and EarthScope (SAGE) Proposal of the National Science Foundation under Cooperative Agreement EAR-1261681.

Last but not least, I would like to thank my parents, my sister, and my brother for their unconditional love and unending support. Special thanks to my beloved wife, Zohreh, whose unwavering love has made all this possible.

Contents

List of Tables

List of Figures

Chapter 1

Introduction

The upper mantle transition zone (MTZ) plays an important role in the style of mantle circulation and mineralogy (Ringwood 1975, Anderson 1989, Bina & Helffrich 1994). The MTZ is bounded by major seismic discontinuities near 410 km and 660 km depths (for short, the 410 and 660, respectively), which are characterized by sharp changes in elastic parameters in global reference models (e.g., PREM by Dziewonski & Anderson (1981) and IASP91 by Kennett & Engdahl (1991)). The impedance (i.e., the product of seismic velocity and density) contrasts across these seismic discontinuities are interpreted to result from mineralogical phase changes or variation in chemical composition in the upper mantle (Ringwood 1975, Ito & Takahashi 1989).

High-pressure anvil experiments suggest that the MTZ discontinuities are associated with solid-state phase transformations of olivine to its higher pressure polymorphs (Akaogi et al. 1989, Ita & Stixrude 1992). For an olivine-rich upper mantle (where olivine comprises greater that 40% of the volume fraction, Figure 1.1a), exothermic phase transition from olivine to wadsleyite and endothermic dissociation of ringwoodite to perovskite and magnesiowustite are generally attributed to the 410 and 660, respectively (Duffy & Anderson 1989, Katsura & Ito 1989). Pioneering studies of mineral physics estimate an average pressure/temperature of

13 GPa/1400 K and 24 GPa/1900 K for the olivine phase changes at the 410 (the former) and 660 (the latter) (Katsura & Ito 1989, Akaogi et al. 2007). These two mineralogical phase boundaries exhibit opposite Clapeyron slopes (Akaogi et al. 1989, Weidner & Wang 1998), which would result in a narrow MTZ in hot (i.e., mantle upwelling) and a thicker MTZ in cold (i.e., subduction zone) regions (Figure 1.1b). There are other controversial mantle discontinuities, one of which resides from 500 km to 560 km depths. The presence of this interface was supported by long-period data (Shearer 1990, 1991, Revenaugh & Jordan 1991, Flanagan & Shearer 1998, Gu et al. 2003, Deuss 2009), which have been less convincing. In mineral physics, a weak reflector could be caused by phase transformation from wadsleyite to ringwoodite (Bina 2003) under the pressure-temperature condition at nearly 520 km depth (also known as the 520 km discontinuity, called the 520, hereafter). The global existence of the 520 is highly variable and its observations are mostly limited to oceanic regions (Gu et al. 1998, Deuss & Woodhouse 2001). The characteristics of these boundaries, such as their topographies or changes in elastic parameters across them, are effective barometers of local temperature and/or chemical composition.

The connection between mantle temperature, mineralogy and seismic observations are far from simple, however. Although the upper mantle discontinuities are attributed to the olivine phase transitions, the structure within the MTZ can be affected by several other factors such as water and Fe contents and contribution from the pyroxene components of the upper mantle (Ita & Stixrude 1992, Agee 1998, Weidner & Wang 2000). For instance, increasing Fe content would reduce the sharpness of the MTZ phase boundaries, thus resulting in weak impedance contrasts across both the 410 and 660 (Akaogi et al. 2007, Deon et al. 2011, Gu et al. 2012).

In comparison with the upper mantle, the MTZ minerals have higher water solubility and are capable of storing up to 3 wt% water (Inoue et al. 1995, Ohtani et al. 2004, Bolfan-Casanova 2005). The presence of water in the MTZ, potentially carried by the subducting oceanic lithosphere (Bercovici & Karato 2003), can increase the MTZ thickness and significantly reduce the reflection amplitudes from the seismic discontinuities (Ohtani et al. 2004, Fukao et al. 2009). The origin of the intraplate magmatism has also been linked to the deep dehydration of hydrous minerals in subducting slabs (Zhao & Tian 2013), as water can induce partial melting and possibly form a thin layer of low velocity zone (melt) atop the 410 (Bercovici & Karato 2003, Karato et al. 2006). This has been clearly identified near the subduction zones, though its presence has been suggested around the globe (Revenaugh & Sipkin 1994*a*, Vinnik & Farra 2002, Bercovici & Karato 2003, Fee & Dueker 2004, Courtier & Revenaugh 2006, Schmerr & Garnero 2007).

The contribution from the pyroxene components of the upper mantle is another major complication in the interpretation of the topography of the MTZ discontinuities. At higher temperatures, the phase transition from the majorite garnet to perovskite becomes dominant at the base of the MTZ (Ita & Stixrude 1992, Weidner & Wang 2000), which can depress the 660 (Deuss 2007, Cao et al. 2011). This observation contradicts the expected effect of temperature, tending to elevate the 660, and may contribute to the reported decorrelation (Flanagan & Shearer 1998, Gu et al. 1998), rather than anti-correlation (Revenaugh & Jordan 1991, Gossler & Kind 1996, Gu et al. 2003, Li & Yuan 2003), between the 410 and 660 depths. The post-garnet phase transitions could also contribute to the complexity of seismic observations beneath the subduction zones (Deuss & Woodhouse 2002, Ai & Zheng 2003, Tibi et al. 2007, Gu et al. 2012), where a deeper reflector (>700 km) has been reported in association with the phase transition from ilmenite to perovskite (Vacher et al. 1998, Akaogi et al. 2002).

In the past three decades, a wide range of seismological observations has been utilized to investigate the existence and properties of the 410 and 660 km discontinuities (Revenaugh & Jordan 1991, Shearer & Masters 1992, Shearer 1993, Revenaugh & Sipkin 1994*b*, Flanagan & Shearer 1998, Gu et al. 1998, 2003, Lebedev et al. 2003, Chambers et al. 2005, Lawrence & Shearer 2006*a*, 2008, Tauzin et al. 2008, Deuss 2009). These seismic arrivals can be categorized into regional and global phases. The regional phases, such as triplications (Helmberger & Wiggins 1971, Wang et al. 2008) and mantle conversions (Rondenay 2009, Liu et al. 2015, Gu et al. 2015), are usually studied at shorter periods (<15 s), which provide higher lateral resolution and reveal the finer-scale thermal/chemical heterogeneities on the order of few hundred kilometers. The converted phases (also known as receiver functions) have been widely used to investigate the mantle stratification beneath the continents (Li et al. 1998, Farra & Vinnik 2000, Li et al. 2002, Schaeffer & Bostock 2010) and subduction zones (Li et al. 2000, Kind et al. 2002, Ai & Zheng 2003). However, these observations are limited to certain regions dependent on the distributions of sources and receivers. On the other hand, global phases (such as *SS* precursors and *ScS* reverberations) are less restrictive (path-dependent) and, thus, more suitable for investigations away from the subduction zones (Revenaugh & Jordan 1991, Shearer & Masters 1992, Deuss 2009). Two prominent examples of these phases are the *SS* and *PP* precursors, secondary specular reflections off the mantle interfaces, which are sensitive to the mantle structure half-way between the sources and receivers. However, due to the longer-period nature (>25 s) of the precursors, their measurements have a lateral resolution of that of their effective Fresnel zone (i.e., on the scale of few thousand kilometers) (Shearer 1993, Rost & Thomas 2009).

A robust imaging technique must produce an accurate model of the reflectivity structure. Unfortunately, studies of the MTZ discontinuities mostly rely on the travel times of the secondary arrivals, and therefore, much of the information embedded in the waveform is conventionally discarded. The improvement in imaging method is crucial for the understanding of weak reflections/conversions in association with the mid-transition zone reflectors, particularly when data coverage is less than ideal.

1.1 Thesis Outline

In this thesis, we employ different methods to analyze the waveforms of *SS* precursors and *P*-to-*S* converted waves and examine the characteristics of MTZ discontinuities in 1) northwestern Pacific subduction zones, 2) southwestern Canada, and 3) Southeast Asia.

In Chapter 2, we quantitatively investigate the timing and amplitude information of a global data-set of *SS* precursors adequately sampling the northwestern Pacific region. We model the full waveform of *SS* precursors using the Genetic Algorithm (GA) (Stoffa & Sen 1991), and properly take the compromise between the shear wave velocity variations and discontinuity depths into our consideration. By using GA we can produce a suit of all possible solutions that are consistent with our observations from precursory waveforms. The purpose of this study is to explore the fate of the subducted Pacific slab and investigate the possible link between the intraplate volcanism in Northeast China and subduction processes. Our results provide compelling evidence for the source of deep-rooted mantle melting in association with the horizontally deflected, stagnant, Pacific slab. This work has been published in *Gondwana Research*, vol. 40, p. 77-90 under Dokht, Gu and Sacchi (2016).

In Chapter 3, we explore another new novel imaging method that bridges the gap between the exploration and global seismology. Furthermore, accurate assessment of mantle reflectivity structure requires a combination of imaging techniques across scale. This is particularly true in the case of incomplete date coverage, high noise levels and interfering seismic phases, especially in tectonically complex regions such as subduction zones and margins.

To overcome these challenges, we apply Singular Spectrum Analysis (SSA) to reduce random noise, reconstruct missing data and enhance the robustness of P-to-S conversions and SS precursors from the MTZ discontinuities. This method performs a rank reduction using singular value decomposition (SVD) by taking advantage of the predictability of time series in the frequency-space domain. We apply SSA to seismological observations of the mantle interfaces from the northwestern Pacific subduction zones and Western Canada Sedimentary Basin. The SSA enhanced reflectivity maps show a greater resolution, which is attributed to the suppression of incoherent noise through rank reduction and the emphasis of principle singular values. The improvements relative to conventional approaches (e.g., normal averaging procedure) are most significant in under-sampled regions. This work has been published in *Geophysical Journal International*, ggw473. doi: 10.1093/gji/ggw473 under Dokht, Gu and Sacchi (2016).

The waveforms of SS precursors are usually sorted into the common midpoint (CMP) areas and stacked, which assumes there is no variation in the discontinuity depth over the averaging area, thereby resulting in over-smoothing for large stacking bins. The resolution of mantle imaging can be further improved by considering scattering and diffraction from the finer-scale depth anomalies. In Chapter 4 we expand our SS precursor coverage to Southeast (SE) Asia to sample the MTZ beneath the Sunda arc, a tectonically complex region where the unimpeded, near vertical penetration of the Indo-Australian slab into the lower mantle has been reported (Fukao & Obayashi 2013, Hall & Spakman 2015). To explore the morphology of the subducting slab and its effect on the topography of the discontinuities, we adopt a pre-stack depth migration of *SS* precursors which can effectively relocate the diffractions from point-scatterers to their true location and improve the resolution of *SS* precursors to approximately 500 km laterally. This chapter will be submitted to the *Journal of Geophysical Research* prior to, or soon after, the thesis defense.

In Chapter 5, we will summarize the key results obtained in this thesis and discuss the potential future works.

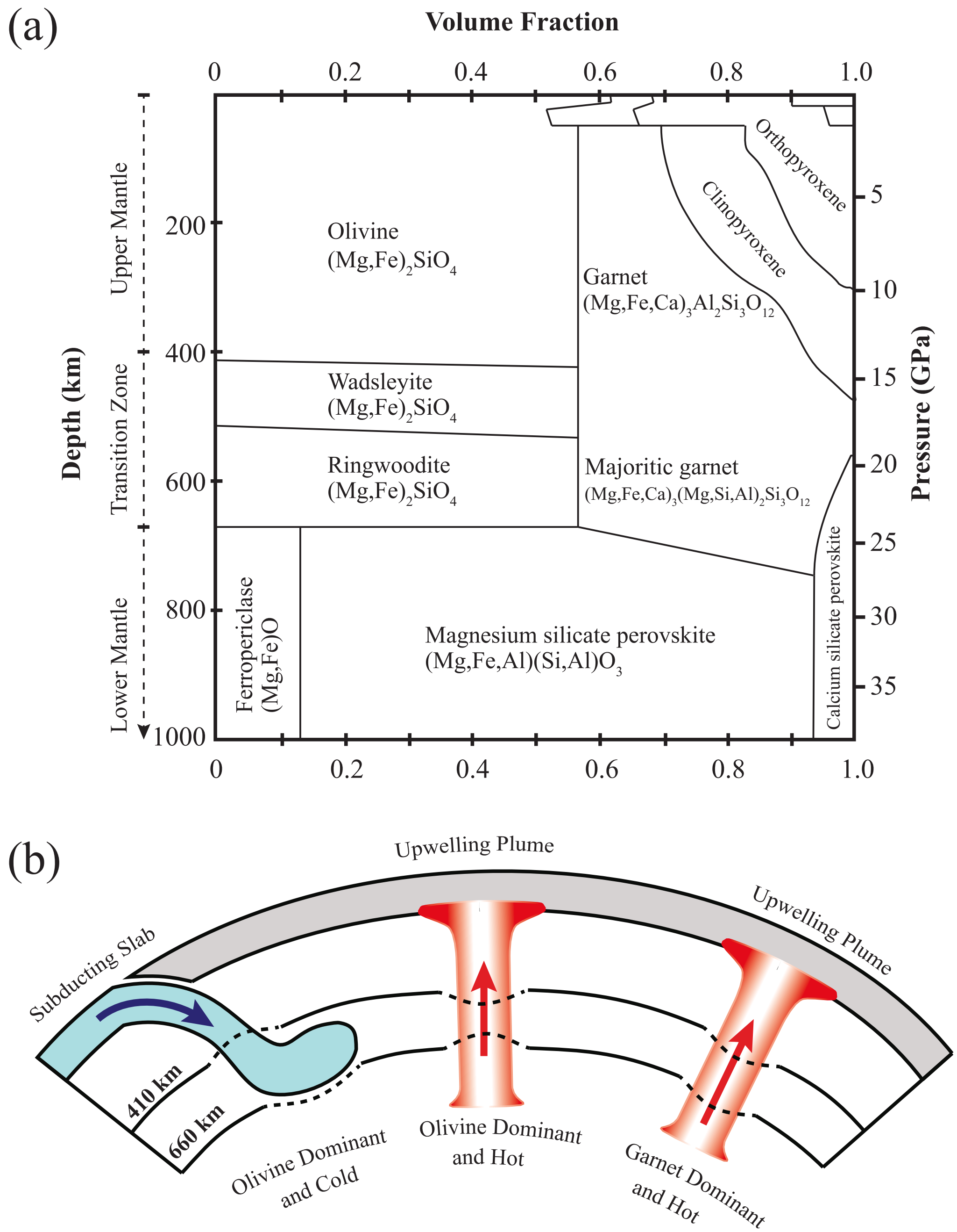

Figure 1.1: (a) Mineral volume fraction of the mantle composition over the depth interval from 0 to 1000 km (modified after Frost (2008)). The upper mantle is composed of nearly 60% olivine and approximately 40% garnet and pyroxene minerals. (b) Topography of the 410 and 660 km discontinuities in the presence of different thermal regimes for olivine (left and middle) and garnet (right) rich mantle compositions (adapted from Deuss (2007)).

Chapter 2

Waveform inversion of *SS* precursors: An investigation of the northwestern Pacific subduction zones and intraplate volcanoes in China

2.1 Introduction

Intraplate volcanic activities have been well documented in both continental and oceanic regions at distances of hundreds to thousands of kilometers away from plate boundary zones. The origin and mechanism of intraplate volcanism vary broadly (Niu 2005, Zhao 2007, Tang et al. 2014) and often require the presence of deep mantle plumes (Campbell 2007, Chen & Tseng 2007, Zhao 2007). An ideal laboratory for the study of intraplate volcanism is northeastern (NE) Asia, where Cenozoic magmatic centers are densely distributed along the north-south oriented Changbai Mountain range and Wudalianchi volcanic field. The former is a stratovolcano located approximately 1200 km west of the Japan trench, while the latter consists of cinder volcanoes covering an area of 500 km^2 toward the north. The origin of these volcanic fields has been linked to mantle plumes as well as subduction-related back-arc spreading and thinning of the lithosphere (Basu et al. 1991, Niu 2005), though compatible helium isotopic compositions between the Cenozoic basalts from the same region and mid-ocean ridge basalt favor an upper mantle origin (Chen & Tseng 2007). Further insights were provided by seismic tomography where a horizontally deflected and stagnant Pacific plate at the base of the upper mantle could play a key role in melt generation (Gorbatov & Kennett 2003, Zhao et al. 2004, Obayashi et al. 2006, Lebedev & van der Hilst 2008, Li & van der Hilst 2010).

Models of seismic velocities are complemented by observations of mantle transition zone (MTZ) discontinuities. For the upper mantle assemblage of olivine composition, phase transitions from olivine to wadsleyite and ringwoodite dissociation are widely accepted origins of the 410 km discontinuity (from here on, 410) and 660 km discontinuity (from here on, 660), respectively, at the top and bottom of the MTZ (Anderson 1967, Ito & Takahashi 1989). These two mineralogical phase boundaries exhibit opposite Clapeyron slopes (Navrotsky 1980, Ito & Takahashi 1989, Katsura

& Ito 1989, Weidner & Wang 1998), and their sensitivities to temperature and composition have been frequently explored in mantle seismic imaging (Shearer 1993, Gu et al. 1998, Gu & Dziewonski 2002, Lawrence & Shearer 2006*b*, Deuss 2009). Based on mantle reflections (Heit et al. 2010, Gu et al. 2012) and conversions (Li & Yuan 2003, Liu et al. 2015), a depression in excess of 30 km has been observed at the base of the MTZ beneath the intraplate volcanic fields in NE China. This topographic anomaly coincides with a distinctive low velocity asthenosphere, which has been interpreted as the potential source of melting beneath the volcanic centers (Zhao et al. 2004, Lei & Zhao 2005, Niu 2005, Li & van der Hilst 2010, Tang et al. 2014).

A known source of error in the independent analyses of seismic velocity and discontinuity topography is the trade-off between them (Flanagan & Shearer 1998, Gu & Dziewonski 2002, Zhao et al. 2004, Obayashi et al. 2006, Li et al. 2008, Li & van der Hilst 2010). Time corrections are typically adopted to minimize the excess topography caused by heterogeneous mantle structures, whereas models of seismic velocities are mostly derived under the assumption of unperturbed mantle interfacial depths. This trade-off was reduced by Gu et al. (2003) and Lawrence & Shearer (2006*b*) through joint inversions of seismic velocity and discontinuity topography, though much of the information embedded in the waveforms of the secondary reflections remained underutilized. In this study we characterize the upper mantle and MTZ beneath the northwestern Pacific region(Figure 2.1) using waveform inversions of stacked *SS* precursors (Figure 2.1d). Our full waveform nonlinear inversion approach recovers a simultaneous solution for the travel times of *SS* precursors, which are sensitive to mantle temperatures surrounding olivine phase boundaries (Ohtani et al. 2004, Deuss 2009, Lessing et al. 2014), and the impedance contrasts imprinted onto the *SS* precursor amplitudes (Shearer 1991, Chambers et al. 2005, Gu & Sacchi

2009, Lessing et al. 2015). We will demonstrate that the resulting dense precursor data-set alone is sufficient to resolve major upper mantle seismic anomalies in the northwestern Pacific subduction system.

2.2 Data and Method

We utilize a global data-set of broadband and long-period seismograms, recorded between 2006 and 2014, from the Incorporated Research Institutions for Seismology (IRIS). The midpoints of the source-receiver pairs densely sample the structure beneath NE China and the northwestern Pacific subduction zones. We restricted the maximum depth of earthquakes to 75 km to mitigate the interference of depth phases (Schmerr & Garnero 2006, An et al. 2007) and adopt a minimum magnitude (Mw) cutoff of 5.5 to ensure sufficient reflection amplitudes. We further constrain the distance from 100° to 160° to minimize the interferences from *ScSScS* (Shearer 1993, Schmerr & Garnero 2006) and topside reflections from upper mantle discontinuities. After deconvolving the instrument responses, we apply a Butterworth bandpass filter with corner periods at 15 s and 75 s to the transverse component seismograms. We eliminate all traces with signal-to-noise ratios (SNR) less than 4.0 according to the definition of Gu et al. (2012), which is more restrictive than the majority of earlier studies due to a substantially larger data volume. The filtered seismograms are then inspected visually to eliminate duplicate records or overlapping events (Schmerr & Garnero 2006), and a polarity reversal is performed if necessary. This refined data-set contains 7868 waveforms from 1301 events. The densities of earthquakes and stations are particularly high in the southern and northern hemispheres, respectively (see Figure 2.1a).

The amplitudes of *SS* precursors, which are comparable to those of noise, are greatly enhanced through stacking after aligning the waveforms on the first major swing of *SS* and normalizing each seismogram with respect to the peak amplitude of *SS*. We then deconvolved *SS* from the transverse component seismograms to minimize the source effects. To correct for the move-out we apply a constant time shift to each waveform based on the differential time between the predicted *SS*-*S410S* (Dziewonski & Anderson 1981) and the reference time for a source-receiver distance of 130° (Gu & Sacchi 2009). The move-out corrected seismograms are then time shifted to account for variations in crustal thickness and surface topography using CRUST1.0 (Laske et al. 2013) and ETOPO1 (Amante & Eakins 2009), respectively. Finally, the time-shifted seismograms are sorted into common midpoint (CMP) gathers (Shearer 1991, Gu et al. 2012) along three parallel great-circle transects (profiles A to C) with 3° inline spacing (see Figure 2.1b). Circular gathers with a radius of 2° (approximately 15% overlap between two adjacent averaging areas in the inline direction) are adopted to prevent over-smoothing while ensuring a sufficient number of traces in each gather for noise suppression. We refer to these circular data gathers either as "caps" or "bins" for the remainder of this thesis. The stacked seismogram in each cap is calculated as the weighted sum of the time-corrected seismograms (Gu & Sacchi 2009). It is worth noting that the majority of the source and receiver locations do not overlap with those of the topographic anomalies, e.g. the Rocky Mountains, Alps and Apennines, that may cause confounding observations within the MTZ (Figure 2.1c). Moreover, while the azimuthal distribution is dominated by two perpendicular orientations (NE, NW), the crossing ray segments effectively average out the path heterogeneity and enable a reasonable recovery of the velocity and discontinuity depth in most bins (Zheng & Romanowicz 2012).

2.2.1 Nonlinear Waveform Inversion

A potential pitfall during an *SS* precursor analysis is the velocity- discontinuity depth trade-off, as the timing of the secondary reflections is corrected based on relatively smooth shear velocity models obtained from earlier studies of body and/or surface waves. An improvement was proposed by jointly inverting for velocity and discontinuity depth using travel times (Gu et al. 2003) and multiple waveforms (Lawrence & Shearer 2006*b*). In this study we quantitatively investigate the waveform information of an *SS* precursor data-set sampling the northwestern Pacific region. We model the full waveforms of SS precursors using the Genetic Algorithm (GA), an effective nonlinear inversion technique (Stoffa & Sen 1991, Haupt & Haupt 2004). A similar waveform inversion approach was recently utilized to analyze *P*-to-*S* converted phases (Chen & Sacchi 2015) for imaging the continental crust.

As a proof of concept we first apply nonlinear inversions to a synthetic seismogram computed using GEMINI 2.2 (Friederich & Dalkolmo 1995). The Green's function calculation assumes a spherically symmetric Earth model and uses a frequency domain method to numerically solve a system of ordinary first-order differential equations (Friederich & Dalkolmo 1995, Friederich 1999, Fichtner & Igel 2008). We then utilize GA, a global optimization approach simulating the process of natural evolution (Haupt & Haupt 2004), to explore solutions of mantle velocity and discontinuity depths that match the simulated waveform with 10% Gaussian noise. This binary-coded algorithm defines variables as indices to a regular discrete search space. Each model parameter (discontinuity depth and velocity perturbations) is represented by a binary string, while the inversion attempts to minimize the following cost function by adjusting the model parameters:

$$J = ||\mathbf{W}(\mathbf{d}_{obs} - \mathbf{d}(I\widehat{\mathbf{m}}))||_2^2 + \mu||\mathbf{D}I\widehat{\mathbf{m}}||_2^2. \tag{2.1}$$

The symbol I is the interpolation operator sampling the model $\widehat{\mathbf{m}}$, consisting of shear wave velocities at discontinuities, at a constant depth interval and $\mathbf{D}$ is a discrete approximation to the first-order derivative. The symbols $\mathbf{d}_{obs}$ and $\mathbf{d}(I\widehat{\mathbf{m}})$ represent the observed and synthetic seismograms, respectively, and $\mathbf{W}$ is the weighting matrix. Finally, μ is a regularization parameter that controls the trade-off between the first and second terms (i.e., misfit and model norm, respectively); it is determined through trial and error. Due to the interference of crustal phases and the side-lobes of the main *SS* arrival, we mainly target the waveforms corresponding to the structure below 200 km. Our model solution consists of 6 layers, ranging from 220 km to 720 km along the depth axis, and the average spacing is 83.3 km. The *S* velocity is allowed to vary by $\pm 4\%$ from PREM, which is larger than the frequently reported range below the lithosphere $-$ the primary target of this study (Grand et al. 1997, Mégnin & Romanowicz 2000, Fukao et al. 2001, Gu & Dziewonski 2002, Gu et al. 2003, Zhao et al. 2004, Obayashi et al. 2006, Li & van der Hilst 2010, Ritsema et al. 2011). Our experiments suggest that an average of 1.5% shear velocity perturbation in the shallow mantle (above 220 km), which is comparable to the reported value beneath NE China (see Simmons et al. (2010) and Tang et al. (2014)), can cause a 2 km movement on the MTZ discontinuity depths and a perturbation of 0.01 km/s (or less) on the MTZ velocity. Neither artifact is significant enough to alter the main observations of this study.

We fix the ratio between density and shear velocity based on PREM, and the perturbations in density are continuously updated as shear velocities vary during the inversions; this is a subjective choice that scales between velocity and density and is adopted to reduce the computational cost (Marone et al. 2007, Yuan & Romanowicz 2010, Liu & Gu 2012). In general, the arrival times are highly sensitive to velocity and discontinuity depth, whereas the amplitude information embedded in the waveforms constrains both velocity and density. While density plays a minor role due to the strong dependence of the objective function on the phase/timing information, a reasonable input density model (PREM in this study) helps stabilize the solutions, especially the shear velocities.

Figure 2.2 shows the results of the nonlinear inversion based on the synthetic data with 10% Gaussian noise. Our input model is modified from PREM, which consists of a low velocity layer atop the 410 and a high velocity layer at the base of the MTZ. We allow 120 solutions in each generation to ensure diversity at a manageable computation cost and steer clear of local extrema. The input and recovered models (see Figure 2.2b) exhibit only minimal deviations, which are mainly associated with the discretized, relatively coarse, model space. The evolution history suggests almost immediate convergence to the final model from an initial suite of random models (Figure 2.2d).

2.3 Results

2.3.1 *SS* Precursor Amplitude

Stacks of *SS* precursor waveforms show robust reflections off the 410 and 660 (*S410S* and *S660S*, respectively) within a laterally varying upper mantle beneath the northwestern Pacific region (Figure 2.3). To evaluate the standard errors and robustness of the *SS* precursors, we adopt a bootstrap resampling algorithm (Efron & Tibshirani 1991, Shearer 1993, Sacchi 1998, Deuss 2009) that makes automatic measurements from 200 randomly selected subsets of the data. During each trial, the amplitudes of *S410S* and *S660S* are directly determined from the positive peaks associated with the precursors. The amplitude uncertainties of the secondary arrivals are subsequently estimated from the standard deviation of the bootstrapped measurements (Deuss 2009). Overall, the maximum standard error in amplitude is 0.2% based on bootstrap resampling.

We construct interpolated reflectivity maps from the *S410S* and *S660S* amplitudes (Figures 2.3a and 2.3b), which are defined as the maximum amplitudes within a 30 s time windows centered on the PREM predicted arrival times of these phases. Large-scale low and high reflectivity zones are detected at the top of the MTZ (see Figure 2.3a). A SW-NE trending high reflectivity zone is present landward from the Wadati-Benioff zone, extending from the North China Craton to the Wudalianchi volcanic center and reaching the maximum value of ~7% (amplitudes are normalized with respect to the *SS* phase amplitudes) beneath the Changbai hotspot (see Figure 2.3a). A second reflectivity zone is observed to the ocean-ward side of the subducting Pacific plate, approximately 500 km away from the Japan trench. The centers of these two anomalies are approximately 1500 km apart.

Strong *S660S* reflections are also observed in the vicinity of the Wadati-Benioff zone (see Figure 2.3b). The largest *S660S*, which attains ~8% of the *SS* amplitude, is identified within the reported slab contours (Hayes et al. 2012). While some of the amplitude variations may be affected by the data uncertainties (Figure 2.3c and 2.3d), especially in the southern part of the study region due to low data density, the largest amplitudes of *S410S* and *S660S* are resolved to 95% confidence levels.

In comparison with PREM, which suggests respective reflection amplitudes of 3.9% and 6.1% relative to *SS* at a source-receiver distance of 130° for *S400S* and *S670S*, the observed values are 1.6-2.3 times higher beneath China (the former) and the Japan Basin (the latter). Part of the amplitude may be affected by the differential attenuation (Q factor) between *SS* and its precursors. However, our experiment, which is based on conservative choices of Q values, suggests a contribution no greater than 0.15%, well within the measurement uncertainties (see Appendix A).

2.3.2 Shear Velocity Variation

We perform nonlinear waveform inversions to simultaneously recover the shear wave velocities and depths of the upper mantle discontinuities. Following the steps of the iterative forward modeling procedure described in Section 2.2.1, the *SS* precursor waveforms are inverted based on 15 generations, each of which contains 120 simulated waveforms computed based on parallel programming. For consistency, the synthetic waveforms are filtered between the same corner periods as the observed data and the source mechanism is removed by isolating and deconvolving *SS* (Figure 2.4). In general, the waveforms of *S410S* and *S660S* are accurately modeled by the synthetic seismograms, especially in view that 1) PREM contains no velocity and density jumps at mid MTZ depths (Dziewonski & Anderson 1981), causing slight mismatches of the waveforms between *S410S* and *S660S*, and 2) the expected misfit between the data and synthetics is nonzero due to the uncertainties (e.g., random noise and imperfect structural corrections) in precursor amplitude and arrival time. The 520 km discontinuity (for short, the 520) is locally enhanced within the Wadati-Benioff zone (Gu et al. 2012), though its lateral variations are complex in all three cross-sections (see Figure 2.4).

We determine a local 1D velocity model for each cap based on the stacked *SS* precursor waveform. A 3D model of the study region is then constructed from the resultant 1D models using a linear interpolation algorithm. The inverted shear velocities under NE China and the northwestern Pacific subduction regions (Figure 2.5) highlight the morphology of the Japan-Kuril trench, showing an average velocity anomaly in excess of 1.5% relative to PREM. This high velocity structure intersects the base of the upper mantle near the Sea of Japan and extends westward toward Central Asia. Its presence and the contrasting discontinuity topography of the 410 (elevated by 10-25 km) and 660 (depressed by 10-27 km) are required to match the low amplitude precursory arrivals (see Figures 2.3 and 2.4). The presence of a high velocity anomaly (interpreted to be the cold subducting oceanic lithosphere) within the MTZ can reduce the impedance contrast across the 660 and produce low *S660S* amplitudes (see Figures 2.4 and 2.5). The eastern side of this dipping high velocity structure shows a distinct low velocity zone, reaching its minimum value (approximately 1.5% slower than that of PREM) within the MTZ beneath the NE Honshu arc. The presence of this anomaly is required by a high amplitude, early-arriving *S410S* oceanward of the subducting Pacific plate (see Figures 2.3 and 2.4), which is partially accommodated by a relative depression (∼15 km) of the 410. This low velocity structure appears to continue to the base of the MTZ under the Japan and Ryukyu trenches.

The most intriguing low velocity zone is observed in the upper mantle beneath NE China, potentially extending 1000 km further inland from the eastern end of the Wudalianchi volcanic belt to the northwestern facade of the Greater Hinggan Mountains (see Figures 2.5a and 2.5b). The center, and deepest part, of this broad anomaly resides beneath the Changbai Mountain Range, initiating at shallow depths and persisting down to a depth of ∼500 km (see Figures 2.5a-c). This low velocity structure is accompanied by a 5-10 km depression of the 410, which reflects an increased *SS-S410S* differential time in this region (see Figure 2.4). The observed low velocity structure under the Wudalianchi volcanic field is limited to depths above 350 km, which is significantly shallower in comparison with that beneath the Changbai hotspot.

Changes in MTZ thickness across the study region, which are calculated from the inverted discontinuity depths (Figure 2.6a), are consistent with those of Gu & Dziewonski (2002) using a correlation based method (Figure 2.6b). Both studies show increased MTZ thickness north of the Ryukyu trench and beneath the Songliao Basin, especially in the present study where values exceed the global average of 242 km (Gu et al. 1998, Gu & Dziewonski 2002, Lawrence & Shearer 2006*a*). The largest difference, which reflects improvements in methodology and spatial resolution, is an anomalously thick MTZ in this study beneath NE China due to a 25-30 km depression of the 660 (see Z1 in Figure 2.6a). This anomaly is consistent with the recent findings of Liu et al. (2015) based on migrated receiver functions (see the dashed-line box, Figure 2.6a). To a lesser extent, the MTZ beneath the Ryukyu trench is approximately 15 km thicker in this study than Gu & Dziewonski (2002), despite similar shapes and signs (see Z2 in Figure 2.6a).

As will be discussed in Section 2.4, the combination of a depressed and amplified 410, a severely deformed 660 and a low velocity asthenosphere beneath the Changbai-Wudalianchi hotspot has major implications for the intraplate volcanism in NE China.

2.4 Discussion

2.4.1 General Assessment

This study presents a nonlinear optimization method that accurately determines the large-scale mantle shear velocity and discontinuity topography based on SS waveform information alone. In comparison with a recent study of *SS* precursors for the same region by Gu et al. (2012), the current study benefits from denser data coverage, especially in the northern flank of the study region where data density increased by ∼50% due to four extra years of recordings. The resolution improved further from the SS precursor amplitude information, which is essential in resolving the impedance contrast at major seismic discontinuities, as well as from the reduced trade-off between velocity and discontinuity depth. While the scale of the reported features (>300 km) may be smaller than the nominal resolution (>1200 km), the use of multiple stations (Rost & Thomas 2009, Schmerr & Thomas 2011) and dense sampling (Cao et al. 2011, Gu et al. 2012, Zheng & Romanowicz 2012) can significantly reduce the effective Fresnel zone and smearing along an isochron (Rost & Thomas 2009, Cao et al. 2010).

The westward dipping high velocity structure beneath the back-arc region (Figures 2.7a-c), which is consistent with earlier findings from P and S-wave travel time (van der Hilst et al. 1991, Fukao et al. 1992, Gorbatov & Kennett 2003, Huang & Zhao 2006, Obayashi et al. 2006, Li & van der Hilst 2010, Zhao et al. 2012) and waveform (Mégnin & Romanowicz 2000, Friederich 2003) inversions, has been widely associated with the subducted Pacific lithosphere beneath the Japan and Kuril islands. The general morphologies of the high velocity structures are concordant with those of Obayashi et al. (2006) (see Figures 2.7d-f), both of which are well supported by the locations of deep focus earthquakes in the study region.

The fate of the subducted Pacific plate has been a source of considerable debate (van der Hilst et al. 1993, Grand 2002, Huang & Zhao 2006, Schmerr & Thomas 2011). While relatively unimpeded penetration into the lower mantle has been documented along the Mariana (Creager & Jordan 1986, Bijwaard et al. 1998, Zhao et al. 2004, Huang & Zhao 2006, Li et al. 2008) and Kuril (Jordan 1977, Li et al. 2008, Schmerr & Thomas 2011, Gu et al. 2012) islands, substantial deformation and changes in slab dip have been frequently suggested at the base of the upper mantle as evidence of slab deflection or bending (Zhao et al. 2004, Fukao et al. 2001, Huang & Zhao 2006, Gu et al. 2012). Beneath the Sea of Japan, the seismic structure in the MTZ is dominated by a 1.5-2.0% increase in P velocity (Fukao et al. 1992, Huang & Zhao 2006, Obayashi et al. 2006), but the deflected slab segment is less well imaged by shear velocities across the study region (Gorbatov & Kennett 2003, Fukao et al. 2009). The result of our waveform inversion of *SS* precursors provides further evidence for the slab deflection below the Sea of Japan and stagnation beneath eastern China (see Figures 2.7a-c).

2.4.2 MTZ Structure and Dynamics

The simultaneous solutions of velocity and discontinuity depth enable a detailed examination of the effective mantle temperatures within the MTZ (Schmerr & Garnero 2006). On the global scale, the depths of the 410 and 660 are either uncorrelated (Flanagan & Shearer 1998, Gu et al. 1998) or slightly anticorrelated (Revenaugh & Jordan 1991, Gossler & Kind 1996, Gu et al. 2003, Li & Yuan 2003). The lack of correlation is largely attributable to smaller-scale heterogeneities (Schmandt & Humphreys 2010), compositional variations (Weidner & Wang 1998, Schmerr & Garnero 2007), or non-vertical structural geometry (Gu et al. 2012). Considerations for localized dipping thermal-chemical structures are crucial in these correlation analyses, especially in the vicinity of major subduction zones. To properly account for slab dip, we compute the correlation coefficients between MTZ thickness and the average MTZ shear velocity for slab dip angles ranging from 15 to 90°. The maximum correlation coefficient (0.72) from all three profiles is attained at 30°, which is 22% higher than the uncorrected (90° dip) value (Figure 2.8). This effective slab dip is in agreement with previously reported values (van der Hilst et al. 1993, Gudmundsson & Sambridge 1998, Huang & Zhao 2006, Hayes et al. 2012), which highlights 1) the need to properly consider the inclined slab morphology, and 2) the dominance of thermal, rather than compositional, variations within the MTZ. However, due to the relative complex morphology, the apparent dip of the slab in Figure 2.8 may not precisely match that of the Wadati-Benioff zone; therefore, it can result in marginal uncertainties in our correlation-based dip estimates. A closer examination of the correlation coefficient at the optimal slab dip (see Figures 2.8c and 2.8d) suggests substantial improvements over the conventional vertical structure assumption in global analyses (Flanagan & Shearer 1998, Gu et al. 1998, Tauzin et al. 2008, Houser & Williams 2010). The strength of the correlation (0.72) largely reflects the severity of thermal perturbations, relative to the ambient mantle, within the subducting oceanic lithosphere. It is enhanced further by a dipping low velocity structure east of the Wadati-Benioff zone (see A5 in Figures 2.7a and 2.7b), which has been previously reported by Obayashi et al. (2006) and Gu et al. (2012) in possible connection with 1) convective return flow in connection with slab dynamics (Bercovici & Karato 2003, Ohtani et al. 2004), and 2) partial subduction of a residual Mesozoic hot thermal plume (Larson 1991, Tatsumi et al. 1998, Honda et al. 2007).

2.4.3 Mantle Beneath the Changbai-Wudalianchi Hotspot

A notable seismic anomaly that reduces the anticorrelation between the depths of 410 and 660 is the low velocity zone beneath the Changbai-Wudalianchi hotspot. The geometry of this low velocity structure (see A3 and A4 in Figures 2.7b and 2.7c) is in excellent agreement with those from earlier studies of this proposed back-arc region (Tatsumi et al. 1990, Lei & Zhao 2005, Huang & Zhao 2006, Li & van der Hilst 2010, Tang et al. 2014). This anomaly has been linked to the horizontally deflected Pacific slab and the subsequent upwelling of hot asthenospheric material (Tatsumi et al. 1990, Li & van der Hilst 2010, Zhao & Liu 2010), though more recent studies (Tang et al. 2014, Liu et al. 2015) have suggested a slab gap west of the stagnant slab.

In this study, the depressed 410 and 660 beneath the Changbai and Wudalianchi volcanic fields imply discontinuous seismic velocities within the MTZ (see A2 in Figures 2.7b and 2.7c), above which a low velocity structure (see A3 and A4 in Figures 2.7b and 2.7c) continues to the shallow mantle. Anomaly A3 appears to terminate at mid-MTZ depths (~500 km), which is moderately deeper than the earlier estimates (Zhao & Ohtani 2009, Li & van der Hilst 2010). Judging from the MTZ velocity characteristics, the transition from low to high velocity appears to be gradational rather than abrupt. The presence of the low velocity zone does not significantly impact the amplitude of the 520, which is diffuse above the stagnant part of the Pacific slab (see Figures 2.4b and 2.7b).

To examine the robustness and resolution of mantle velocities and discontinuity depths, we conduct a hypothesis test, a frequently adopted technique for linearized inversions. In this test we introduce a low velocity structure resembling that beneath the Changbai hotspot (Figure 2.9). This hypothetical anomaly terminates near 410 km, overlying a high velocity structure similar to the stagnant oceanic lithosphere. The input depths of the 410 and 660 are both depressed by more than 10 km near the largest shear velocity perturbations. After the synthetic seismograms are computed for each cap location based on these input parameters, we add up to 0.2% Gaussian noise depending on the observed standard errors from bootstrap resampling (Section 2.3.1). The recovered models through the same inversion procedure show two well-defined seismic velocity anomalies with the same signs and shapes as the inputs (see Figure 2.9). The maximum amplitudes of the recovered anomalies are about 80% and 95% of the assumed values of the respective low and high velocities; the recovery of the latter anomaly is superior due to a larger, more laterally coherent input structure. The amplitudes near the edges of the major anomalies are preferentially reduced due to the lateral averaging with a substantially weaker structure to the west. The depressions of the phase boundaries near the center of the profile are recovered to 90-95% relative to the input values. The performance of the inversion is equally effective in resolving a relatively shallow low velocity zone beneath the Wudalianchi hotspot. In this case, the inversion recovers over 75% of the maximum input velocity and discontinuity topography, as well as a minor lateral gradient east of the volcanic center (see Figure 2.9). Our hypothesis test demonstrates that 1) a restoring resolution analysis is equally effective in nonlinear inversions as their linear counterpart, and 2) the morphologies of the low velocity zones beneath the volcanic centers and the underlying stagnant slab can be sufficiently resolved in our study region.

To further validate the recovered images from the 1D waveform inversions of *SS* precursors (see Figure 2.7), we implement 2D waveform tomography using the same nonlinear inversion technique (Figure 2.10). The mantle is discretized into cells of 3° (in the horizontal direction) by 50 km (in the vertical direction). To simplify this problem, we assume known discontinuity depths from the 1D inversions (see Figure 2.7) and only solve for perturbations of shear velocities within each cell; it is worth noting that we define a finer vertical cell size of 10 km around the discontinuity depths of 220, 300, 400, 520 and 670 km. In this approach, the travel times of the precursors and their corresponding reflection coefficients are calculated using the 2D ray tracing method (Lebedev et al. 2003, Zhao et al. 2004, Priestley et al. 2006, Lawrence & Shearer 2006*b*). Then, the reflectivity profiles are convolved with the source time functions extracted from the stacked waveforms (Shearer et al. 1999). We generate over 2000 solutions at each generation, while 5% of the initial random solutions are replaced by the shear velocities from GyPSuM (Simmons et al. 2010). The optimized synthetic waveforms from 2D nonlinear inversions closely match the observations along profile B (see Figure 2.10b). The velocity model shows a westward dipping structure similar to that recovered by the 1D waveform inversions, which appears to flatten toward NE China. The maximum velocity anomaly of the slab (1.5%) is comparable to that of the 1D inversion, whereas the low velocity zone above the 410 (-1.1%) is slightly weaker than the 1D counterpart. Part of the amplitude difference between the 1D and 2D inversion outcomes could be explained by the inclusion of a more realistic, low velocity lithosphere in the latter experiment.

Our models consistently suggest a relatively warm mantle in the vicinity of the 410. The observed 5-10 km depression of the 410 beneath the intraplate volcanic fields in mainland China can be attributed to the response of the olivine to wadsleyite phase transition, an exothermic reaction with a positive Clapeyron slope of 1.5-4.0 MPaK^{-1} (Akaogi et al. 1989, Houser & Williams 2010, Lessing et al. 2014), to the presence of a high temperature anomaly above or across this boundary. By assuming the temperature dependence of the shear wave velocity ($\frac{\partial lnV_s}{\partial T} = -7 \times 10^{-5}$/K) for a dry upper mantle (Houser & Williams 2010), an S wave velocity reduction of 1.5% results in an approximate temperature increase of 215 K relative to the average value of 1694 K for the olivine phase change (Houser & Williams 2010). The phase boundary moves toward the higher pressures (by 320-860 MPa) and greater depths, which are consistent with recent reports of 20-30 km of depression in the same region (Li et al. 2000, Li & Yuan 2003, Liu et al. 2015). Different mechanisms have been proposed to explain the origin of a widely distributed low velocity regime in the upper mantle beneath NE China, most of which are associated with the subducting Pacific plate. An incomplete list of these mechanisms include 1) partial melting induced by the deep dehydration of the slab (Zhao & Ohtani 2009), 2) passive upwelling of asthenospheric material in response to slab accumulation within the MTZ (Bercovici & Karato 2003, Kuritani et al. 2009, Faccenna et al. 2010), and 3) mantle upwelling from a slab gap (Tang et al. 2014, Liu et al. 2015), whose lateral dimension ($\sim$ 200 km) remains beyond the resolution of SS precursors from this study.

The first mechanism infers significant amount of water near the 410, while up to 3 wt% water could be present in the MTZ (Bercovici & Karato 2003). A relatively wet mantle around the 410 would elevate the olivine to wadsleyite phase boundary. While the extent of the elevation in the presence of water remains questionable (Frost & Dolejš 2007, Schmerr & Garnero 2007), an elevated 410 is simply inconsistent with either the observed depression from this (see Figure 2.7) and earlier studies (Li & Yuan 2003, Liu et al. 2015), or the reported water content in this region (Ichiki et al. 2006, Chen & Tseng 2007, Fukao et al. 2009, Ye et al. 2011). In the case of water saturated mantle, a hydrous melt lens may form atop the 410 and produce multiple phase transitions. This was reported in South America where a relatively deep, modest wet to dry wadsleyite reflection was detected at 415 km (Schmerr & Garnero 2007). Based on numerical experiments from the same study, the expected amplitude (which increases with water content) is significantly lower than the predicted value from PREM and far below those of our observations under the Changbai hotspot.

A favorable solution for the observed 410 amplitude and depth requires a significantly increased impedance contrast across a depressed 410, which could be satisfied by the presence of a melt layer in a relatively dry, warm mantle. Increasing the Mg content by up to 4% within the melt layer can effectively depress the 410 by approximately 10 km (Fei & Bertka 1999, Schmerr & Garnero 2007), which corroborates our observations in NE China. Both decompression melting associated with passive upwelling (Bercovici & Karato 2003, Faccenna et al. 2010) and a significant subslab component from the slab window (Tang et al. 2014) can induce partial melting atop the 410. This melt layer would depress the 410 phase boundary, enhance the impedance contrast and substantially increase the S wave reflection amplitude, which are all supported by our observations beneath the Changbai hotspot. Insufficient resolution around the suggested slab window (see Figures 2.7 and 2.11) makes it difficult to clearly differentiate between these two candidate mechanisms, however.

Further inferences could be made regarding the mantle beneath the two volcanic centers examined in this study. Despite the considerable depth difference between the Changbai (about 500 km) and Wudalianchi (about 350 km) hotspots, trace element analyses (Basu et al. 1991, Kuritani et al. 2009) suggest a comagmatic upper mantle origin with EM1 (Enriched Mantle 1) composition (Jackson & Dasgupta 2008). Hence, it is conceivable that the mantle upwelling beneath the Changbai hotspot is responsible for the source of partial melt for both volcanic centers in view of its greater vertical extent and strength (see Figures 2.5a and 2.11). Further work will be needed to quantify the accuracies of the aforementioned mechanisms and interpretations.

Finally, increased seismic velocities at the base of the MTZ under NE China and a deep 660 (>680 km) relative to the regional average of 655-665 km (Shearer 1993, Gu et al. 2003, Houser & Williams 2010) are consistent with the respective measurements based on analyses of receiver functions (Li et al. 2000, Li & Yuan 2003, Liu et al. 2015) and migration of long period *SS* precursors (Gu et al. 2012). A maximum depression of 20-30 km is reported on the 660, possibly in association with a decrease of 300-400 K in MTZ temperature (Li & Yuan 2003, Ye et al. 2011). A negative temperature anomaly of ∼300 K and a greater depth of the 660 jointly suggest increased S wave velocities of ∼2% in the presence of a negative Clapeyron slope from the post-spinel phase transition (Houser & Williams 2010, Lessing et al. 2014). The low temperature anomaly and locally depressed 660 could be explained by the existence of water within the MTZ, the amount of which depends on the volume entrained within the slab as well as the residence time of the slab (Fukao et al. 2009). Recent S waveform modeling from NE China detects a 130 km thick high velocity zone at the base of the MTZ, which may contain up to 0.3 wt% water based on the estimates from Ye et al. (2011).

2.5 Conclusion

Our study demonstrates that the shear wave velocity and the topography of MTZ discontinuities beneath NE China and the northwestern Pacific region can be simultaneously recovered using the waveforms of SS precursors alone. A statistically significant positive correlation is observed between MTZ thickness and the average MTZ velocity along an effective slab dip of ∼30°, which reflects the dominant effect of thermal heterogeneity in the upper mantle and MTZ. A strong low velocity zone is found beneath the active volcanoes in NE China, persisting to a depth of ∼500 km, which implies that the Changbai and Wudalianchi hotspots may be fueled by a hot thermal anomaly from MTZ depths.

Passive upwelling and/or a slab window could be responsible for a relatively water-poor melt layer atop the 410, which causes 5-10 km depression and substantially enhances the reflection amplitude on the olivine to wadsleyite transition. A distinctive low velocity structure is also observed east of the Wadati-Benioff zone, which narrows the MTZ by 30 km relative to its regional average. This low velocity zone is possibly associated with (i) a fossil superplume (∼140 Ma) or (ii) upwelling hot mantle material in response to slab-lower mantle interaction. Overall, our findings from nonlinear SS precursor waveform inversions provide a new window into the effects and fate of the subducting oceanic plate in the northwestern Pacific region.

From a technical stand point, the nonlinear joint inversion technique introduced in this study represents a new phase in the retrieval of seismic properties pertaining to large scale thermal/chemical structures in the mantle. This is not aimed to be a replacement of the existing travel time and waveform tomographic approaches, especially in view of the relatively coarse spatial resolution of the *SS* precursor data-set, but an improvement that effectively incorporates the amplitudes of the secondary reflections or conversions from mantle interfaces.

The research described in this Chapter has been published in: Dokht, R. M., Gu, Y. J., & Sacchi, M. D. (2016), Waveform inversion of SS precursors: An investigation of the northwestern Pacific subduction zones and intraplate volcanoes in China, *Gondwana Research*, **40**, 77−90.

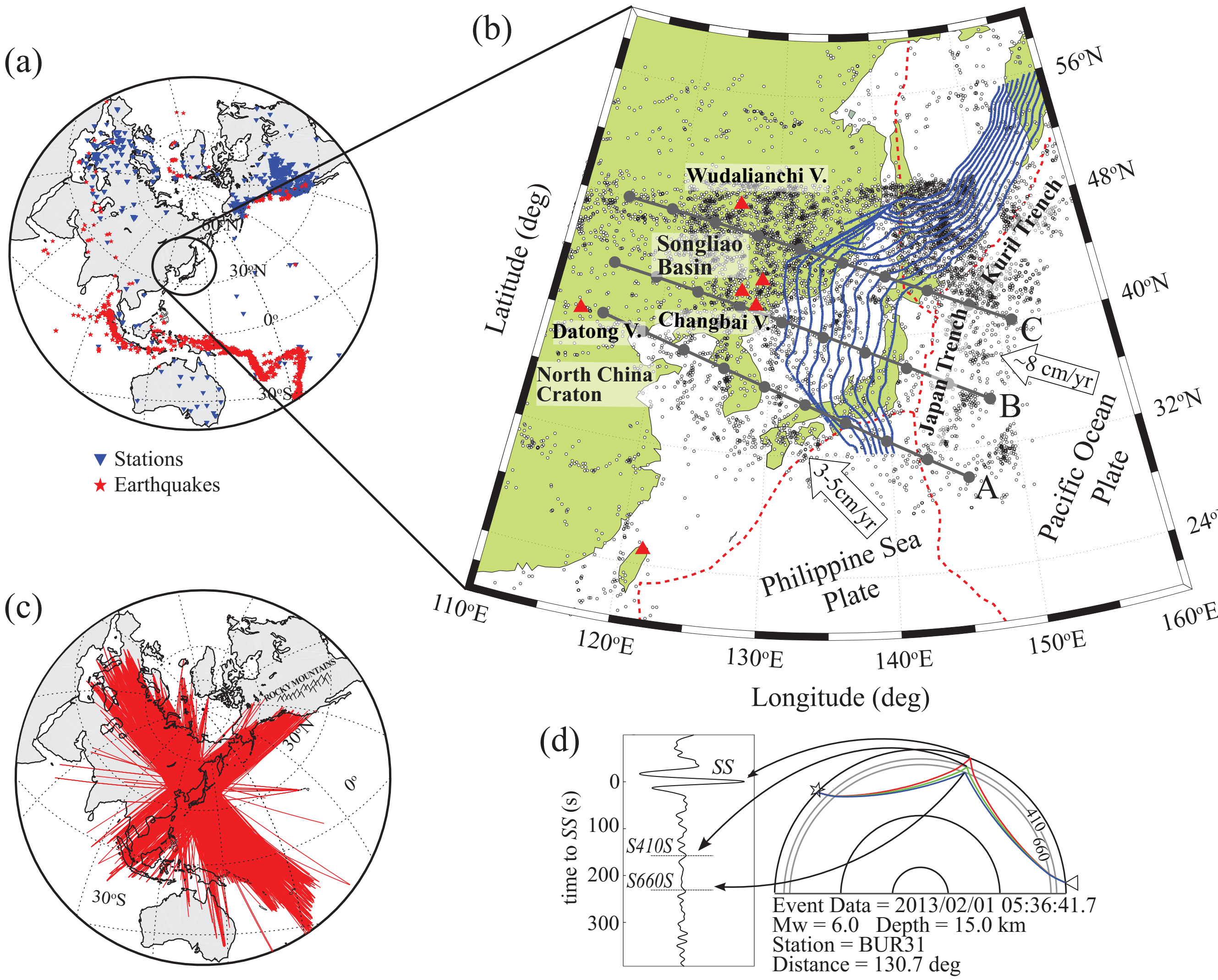

Figure 2.1: (a) Global distribution of the earthquake (red stars) and station (blue triangles) locations used in this study. (b) Distribution of the *SS* bouncepoints from the earthquake-station pairs. The convergent plate boundaries and slab contours are indicated by the red and blue lines, respectively. The contour lines are taken at a constant interval of 50 km starting at 100 km depth (Hayes et al. 2012). The *SS* precursor waveforms are stacked into 30 bins along three parallel profiles A, B and C. (c) Path coverage of the *SS* precursors that are used in the stacking and inversion procedures. (d) A graphical representation of theoretical ray paths of *SS* and its precursors for a source-receiver distance of 130.7 degrees. The left panel shows an observed seismogram aligned on the maximum amplitude of the *SS* phase. *S410S* and *S660* are marked based on the predicted arrival times of PREM (Dziewonski & Anderson 1981).

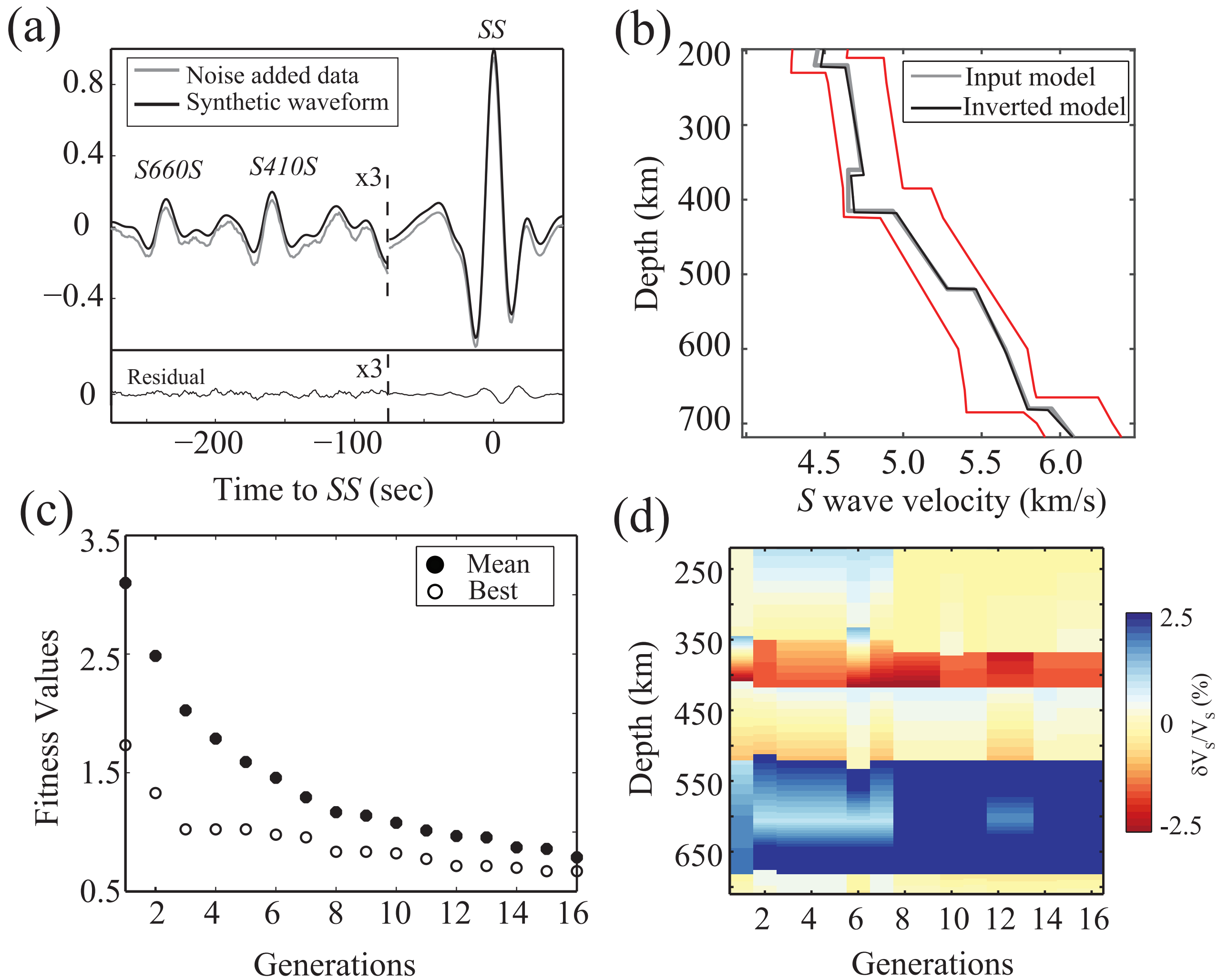

Figure 2.2: (a) An input transverse component seismogram with 10% noise (gray) and the inverted trace after 15 generations (black). The precursors are magnified by a factor of 3 and the difference (data-synthetic) seismogram has been offset by -0.08 for clarity. (b) The input (gray) and the recovered (black) model velocities. The red lines indicate the lower and upper boundaries of the model space. (c) The best and mean values of the objective function in each generation. (d) Color-coded velocity output from nonlinear inversion of the noise-added synthetic seismogram. Random input velocity structures are assumed at the first generation.

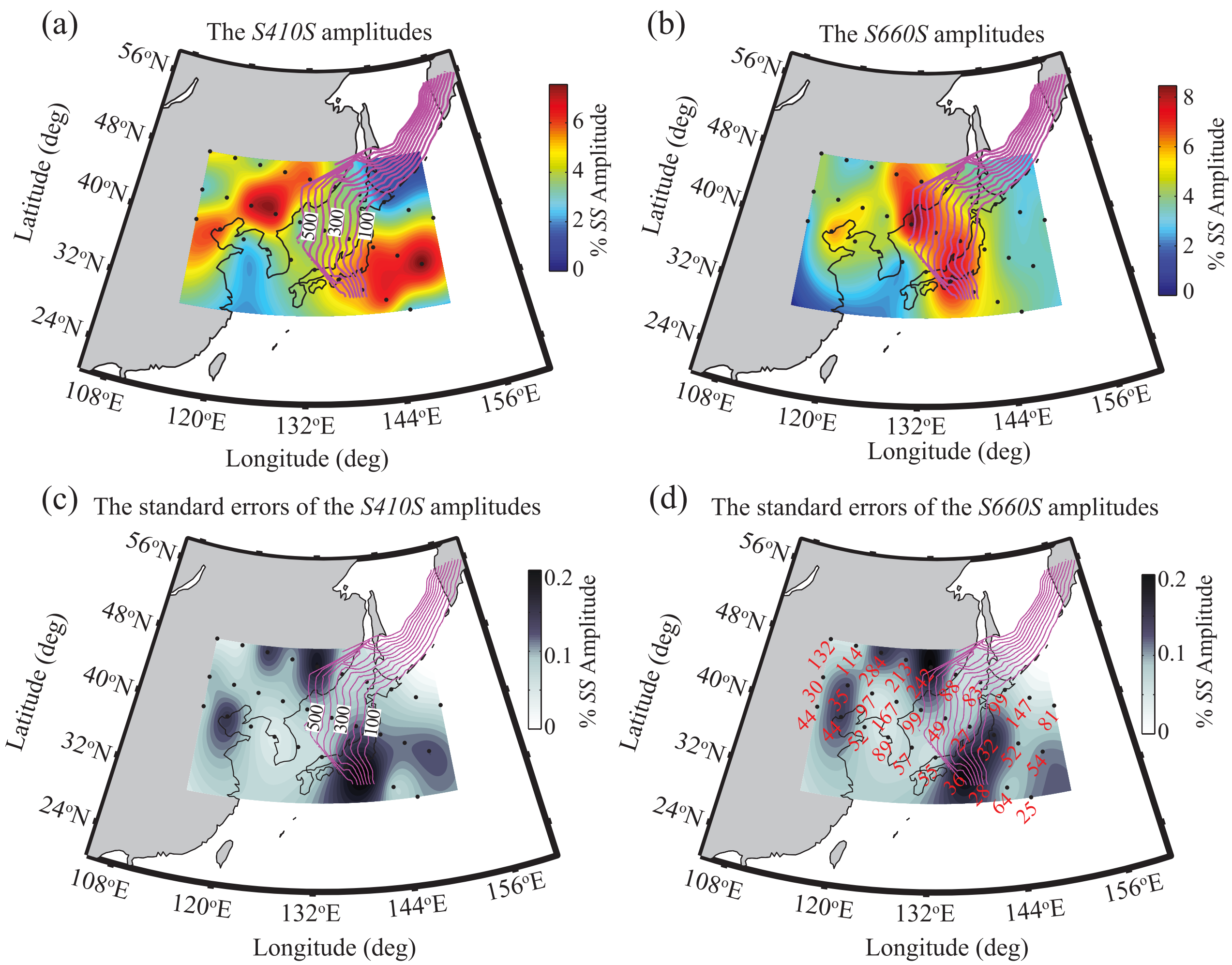

Figure 2.3: The interpolated reflectivity maps of *S410S* (a) and *S660S* (b) amplitude variations. (c) and (d) show the standard errors of the reflection amplitudes based on a bootstrapping analysis. The solid circles denote the centers of the averaging bins and the magenta lines show the slab contours (Hayes et al. 2012). The numbers at the center locations of the averaging bins in panel (d) show the total number of waveforms in each cap used in stacking.

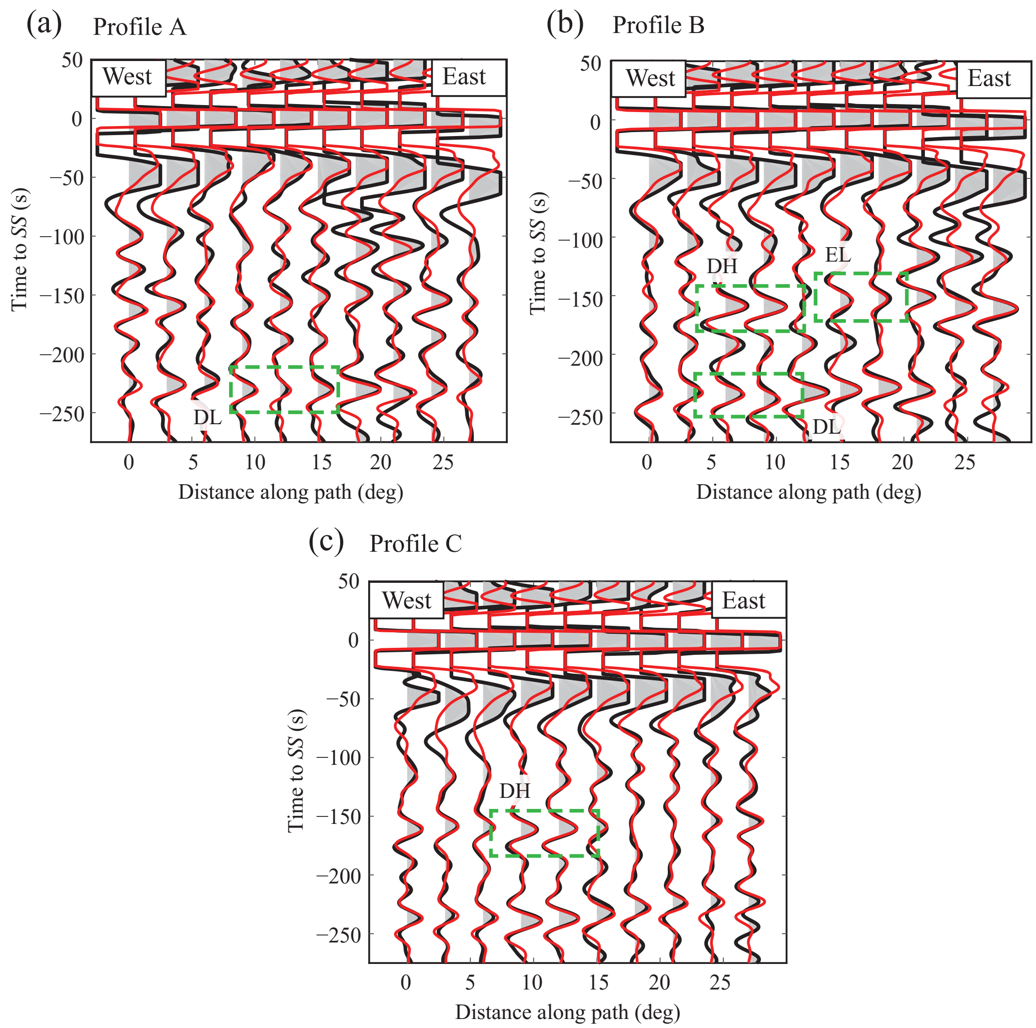

Figure 2.4: *SS* precursor waveform inversion results for profiles A to C. In all panels the black and red lines represent the observed and synthetic stacks, respectively. The key features in the waveform data are highlighted using the dashed boxes. The symbols D and E represent areas with depressed and elevated discontinuity topography, respectively. The letters H and L indicate the high and low amplitude precursory arrivals, respectively.

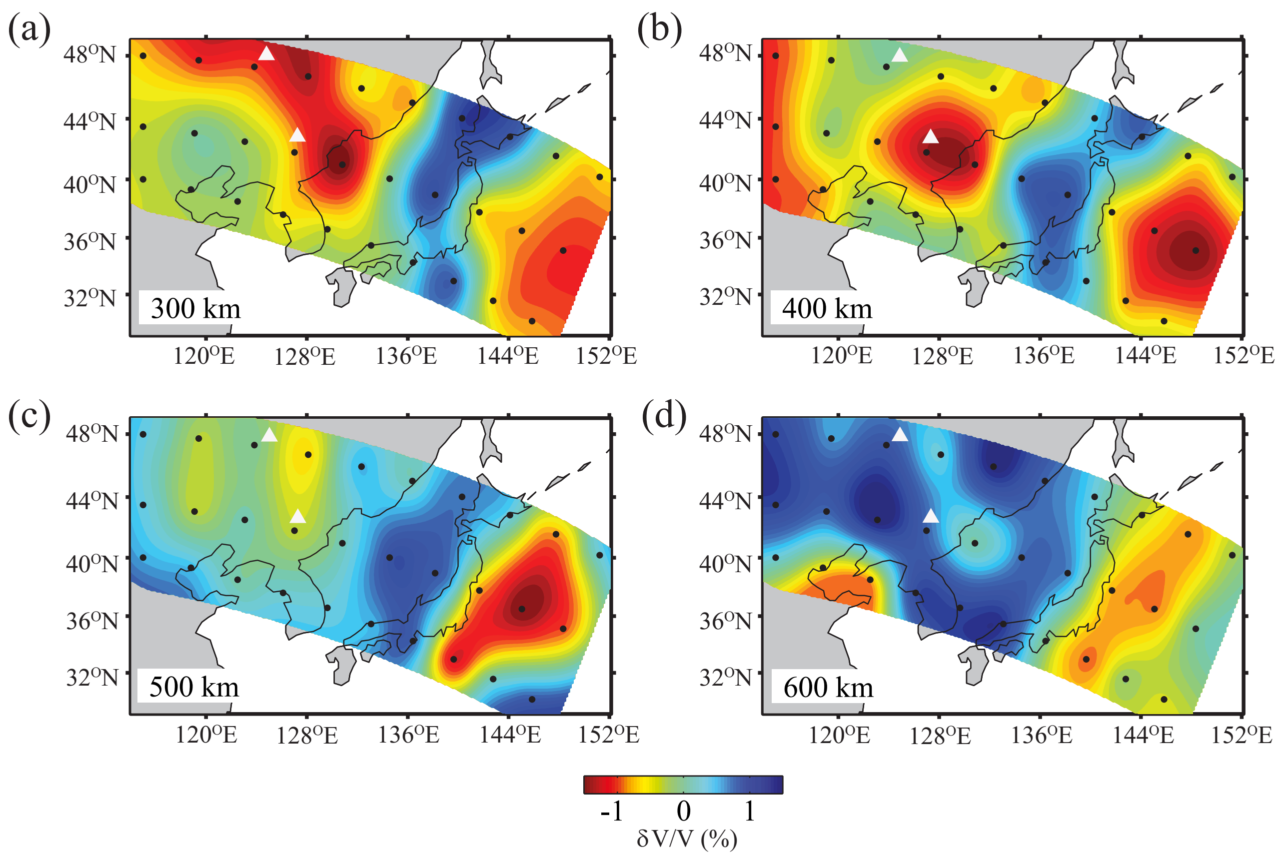

Figure 2.5: Lateral variations in S-wave velocity relative to PREM (Dziewonski & Anderson 1981) at 300 km (a), 400 km (b), 500 km (c), and 600 km (d) depths beneath NE China and the northwestern Pacific region. The blue and red colors represent fast and slow anomalies, respectively. The solid circles mark the centers of the averaging caps and the white triangles denote the locations of major intraplate volcanoes.

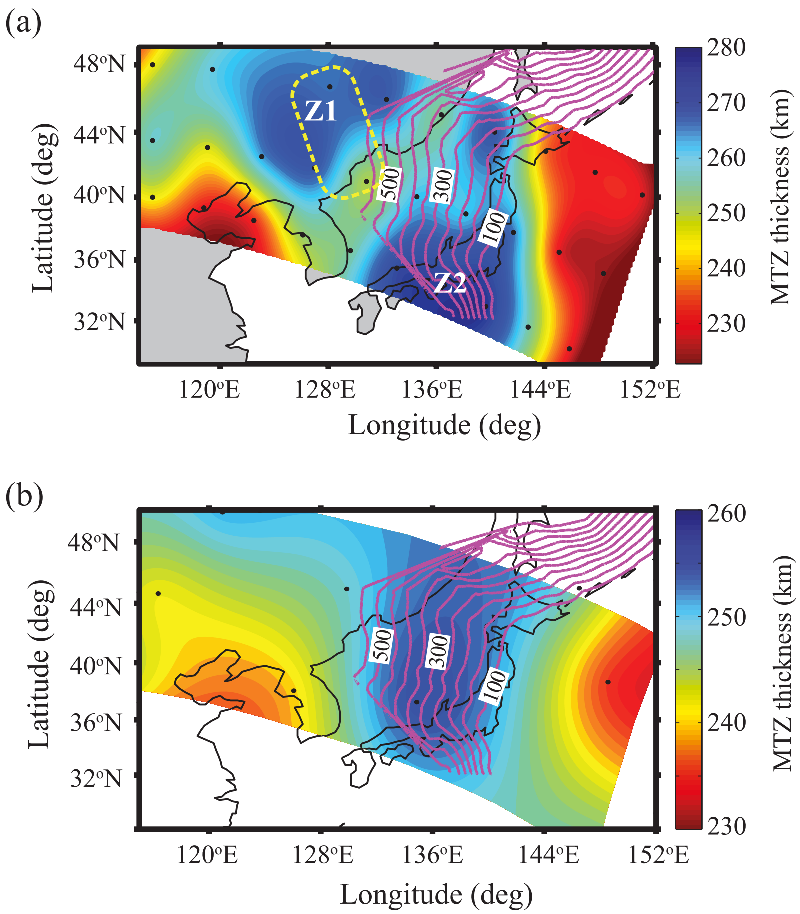

Figure 2.6: (a) MTZ thickness variations inferred from the inverted depths of the 410 and 660 by this study. (b) MTZ thickness variations reported by Gu & Dziewonski (2002). The red and blue colors represent regions of narrow and thick MTZ, respectively. Z1 and Z2 indicate anomalously thick MTZ beneath NE China and the Ryukyu trench, respectively. The dashed-line box in panel (a) outlines a relatively thick MTZ (>270 km) in Liu et al. (2015), obtained from depth migrated P-to-S converted waves.

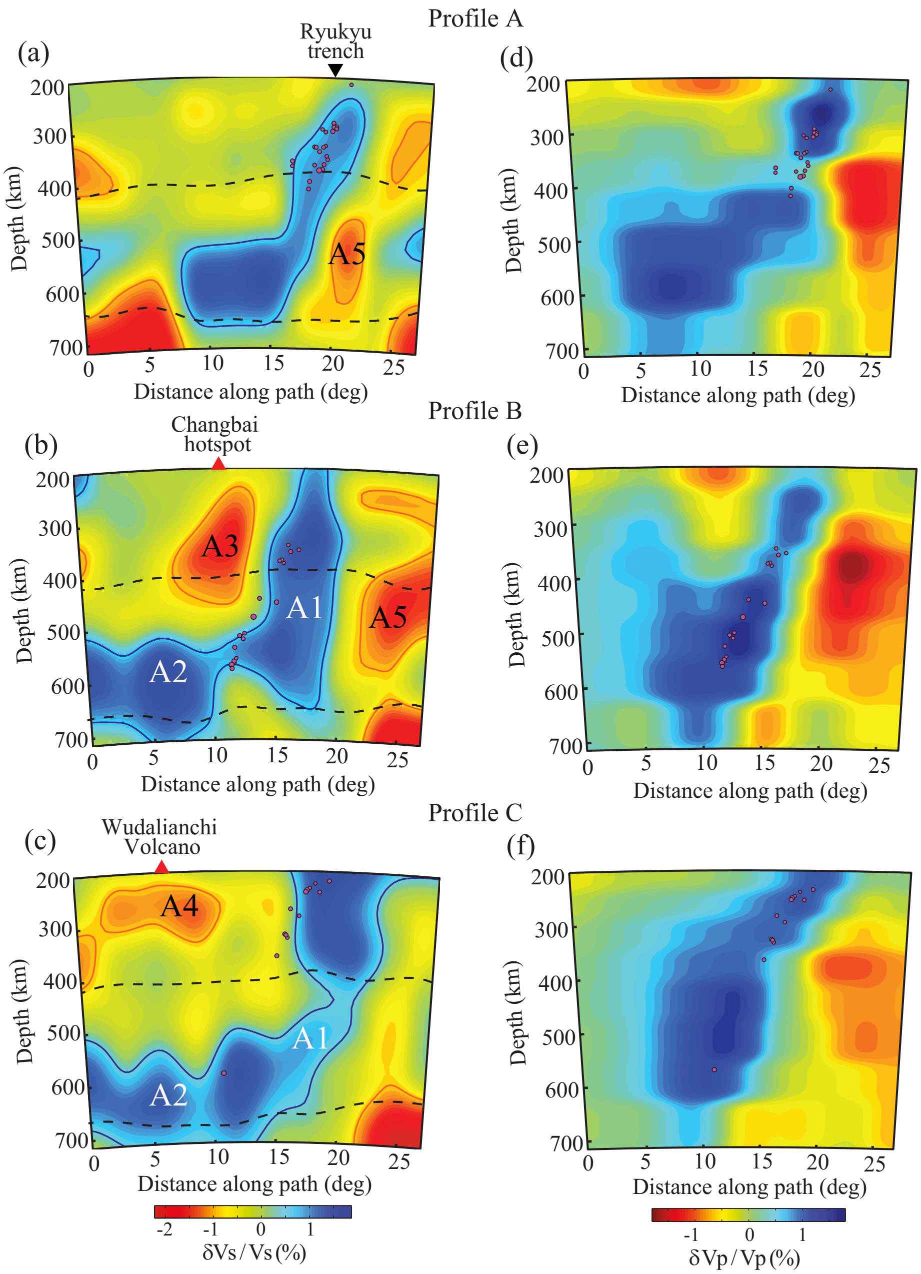

Figure 2.7: (a)-(c) West-east vertical cross-sections of the inverted shear wave velocity anomalies along profiles A to C from 200 to 720 km depth beneath the northwestern Pacific subduction zones and NE China. The magenta circles indicate the locations of deep earthquakes within a 2° distance from each profile. The depths of the 410 and 660 km discontinuities are indicated by the dashed lines. A1 and A2 mark the downgoing and stagnant parts of the Pacific slab, respectively, while A3 and A4 denote low shear velocity anomalies beneath the Changbai-Wudalianchi hotspot. A5 indicates low seismic velocities on the ocean side of the Wadati-Benioff zone. (d)-(f) Similar to (a)-(c), but for an earlier model of *P*-wave velocities (Obayashi et al. 2006).

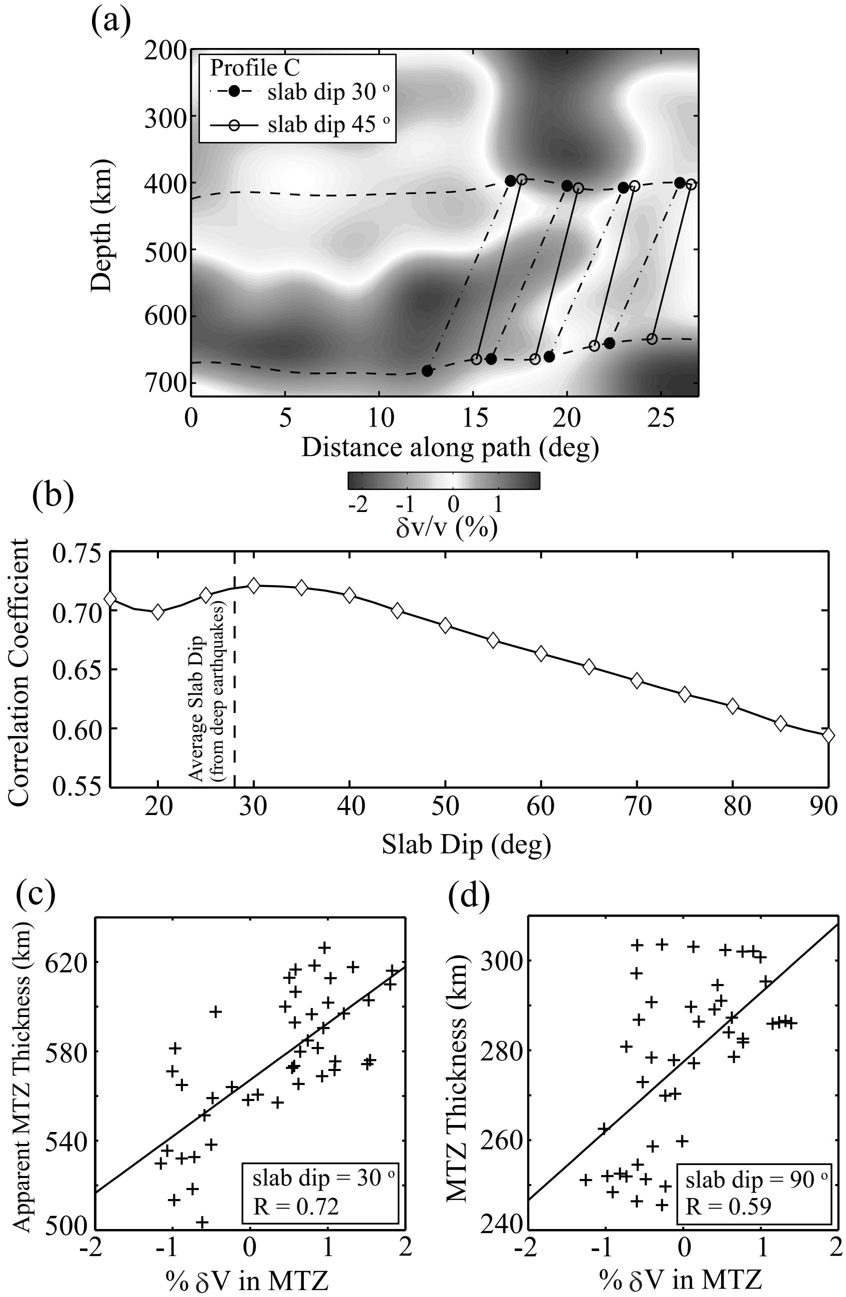

Figure 2.8: (a) A cross-section of our shear velocity model along profile C. The dashed and solid straight lines indicate how the MTZ thickness and average MTZ velocity are measured along slab dips of 30 and 45 degrees, respectively. (b) The correlation between MTZ thickness and the average MTZ shear velocity perturbations at a range of dip angles. (c) Observations of apparent MTZ thickness versus the apparent average MTZ shear velocity along slab dip of 30 degrees. The least-square fit and correlation coefficient are also shown. (d) Similar to (c) but for slab dip of 90 degrees.

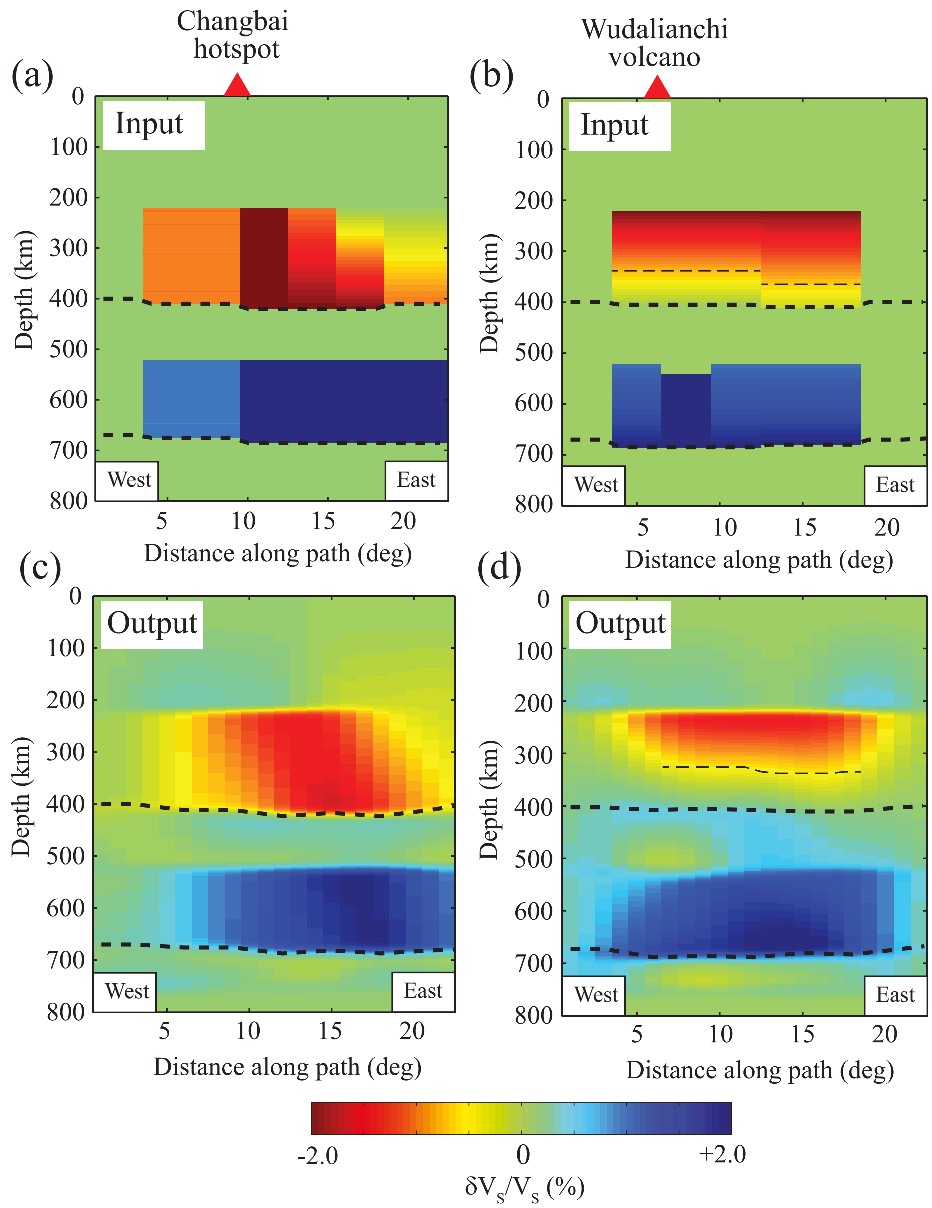

Figure 2.9: Input models (panels a and b) and the inverted results (panels c and d) of the synthetic tests along profiles B and C. The depths of the 410 and 660 are indicated by the thick dashed lines.

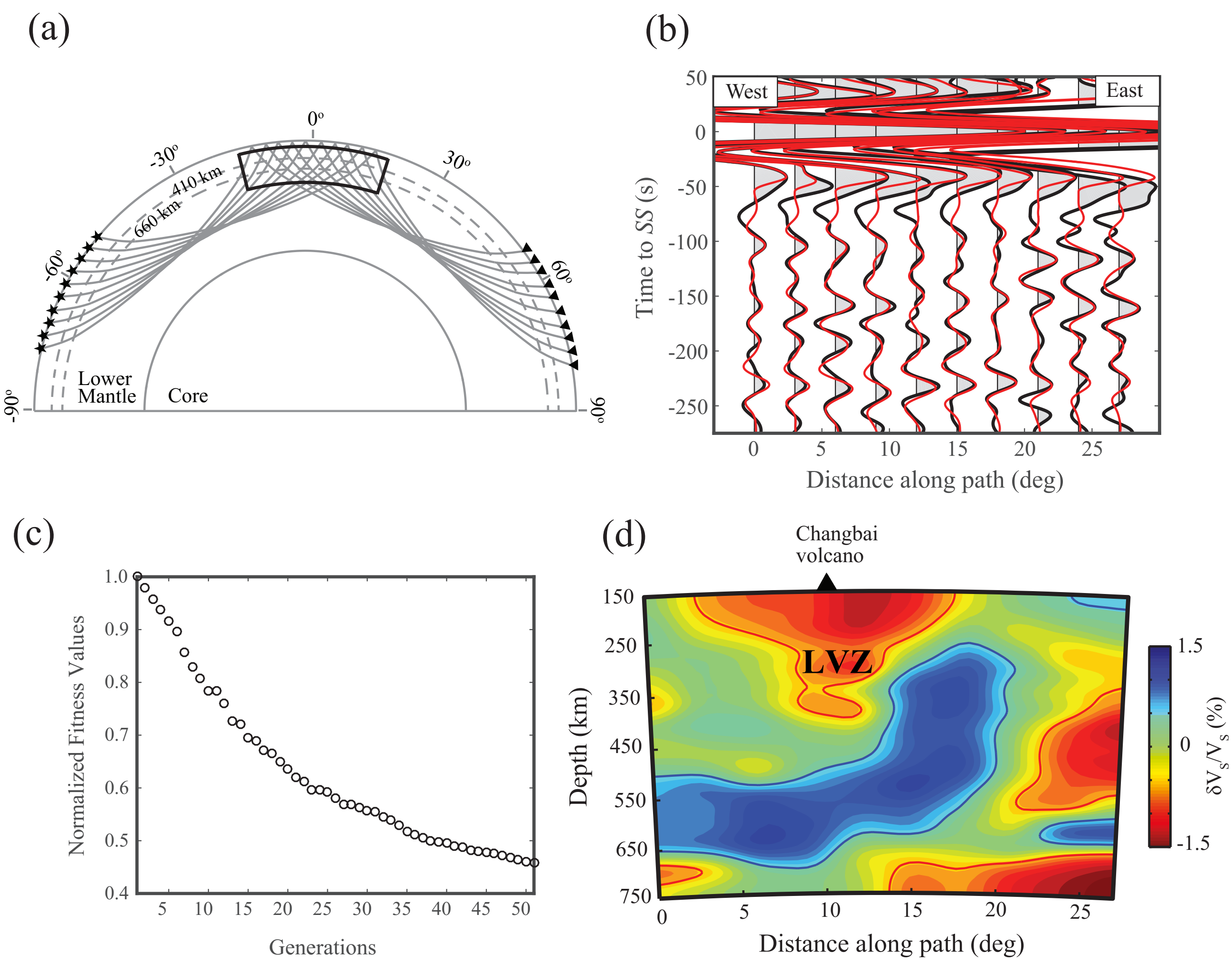

Figure 2.10: 2D waveform tomography results using the stacked waveforms observed along profile B (see Figure 2.4). The results clearly show a high velocity structure, associated with the subducting plate, and reduced shear wave velocities beneath NE China. (a) Schematic view of the *SS* ray paths used in waveform tomography. The sources and receivers are indicated by stars and triangles, respectively. The thick black lines outline the area covered by the waveform tomography approach. The outlined area is zoomed on from 200 km to 750 km depth. (b) The visual comparison between the observed (black) and synthetic (red) waveforms shows a good agreement between the input and modeled waveforms. (c). The normalized fitness values of the objective function in each generation. (d) Color-coded cross-section (outlined area in panel a) of the shear wave velocity perturbations. The blue and red colors represent the fast and slow velocities, respectively. The key features of the recovered image are also labeled (LVZ stands for low velocity zone).

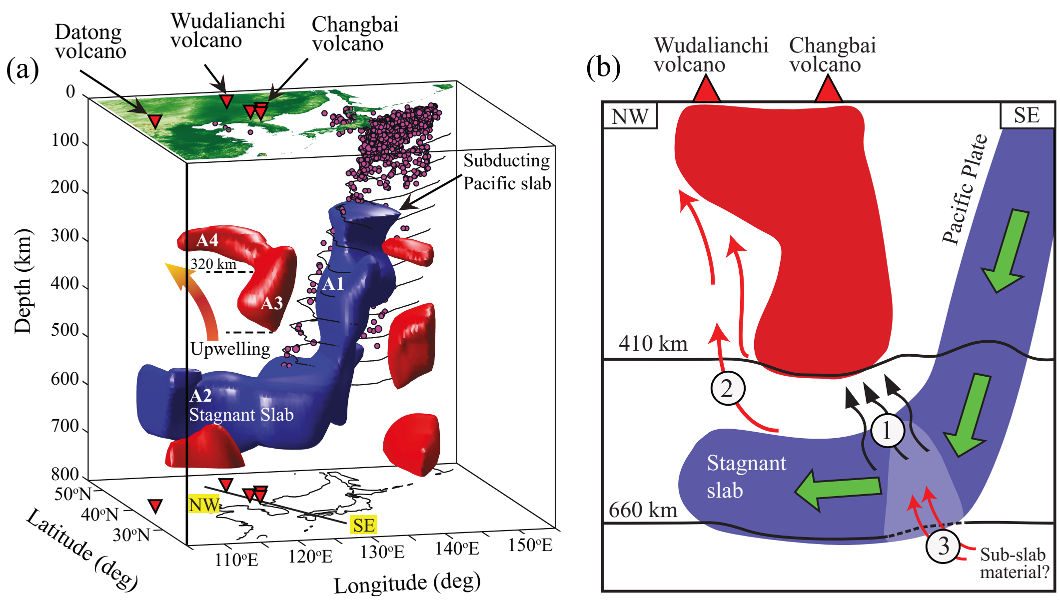

Figure 2.11: (a) Isosurfaces showing the major seismic anomalies beneath Northeast China and the northwestern Pacific subduction zones in the depth range of 200 to 700 km. The blue and red colors represent fast and slow shear velocities, respectively, at the respective isosurfaces of +0.65% and -1.0%. The definitions of major seismic anomalies (A1-A5) are the same as in Figure 2.7. The black lines show the slab contours, which are taken at 50 km depth intervals starting at 100 km (Hayes et al. 2012), and the magenta circles indicate the locations of deep-focus earthquakes. (b) A schematic illustration of a NW-SE vertical section (see Figure 2.11a) showing the possible origins of the intraplate volcanism in Northeast China. Three possible mechanisms for the intraplate volcanism (discussed in Section 2.4.3) are also illustrated: (1) deep dehydration process of the slab, (2) passive upwelling in response to the subduction of the Pacific plate, and (3) escaping of the hot sub-slab material through a slab window.

Chapter 3

Singular Spectrum Analysis and its applications in mapping mantle seismic structure

3.1 Introduction

Enhancement of the signal of interest and suppression of random noise are crucial for achieving superior image quality and signal coherency (Cadzow 1988, Sacchi 2009, Oropeza & Sacchi 2011, Naghizadeh 2012). Over the past decades, different methods have been proposed for data interpolation and noise attenuation by exploring the predictability of seismic signals. These methods may be performed in the time-space (t-x) domain (Abma & Claerbout 1995) or by transforming the data to other domains such as frequency-space (Canales 1984, Gulunay et al. 1986, Spitz 1991), slant-stack (also known as Radon domain; Sacchi & Ulrych (1995), Trad et al. (2002)), and frequency-wavenumber (Naghizadeh 2012). A method that has received significant recent attention is singular spectrum analysis (SSA), a rank reduction-based technique (also known as Cadzow filtering) for the simultaneous random noise removal and data reconstruction in the case of missing samples (Broomhead & King 1986, Cadzow 1988, Sacchi 2009, Oropeza & Sacchi 2011). This technique was first introduced in time domain in the analyses of experimental dynamical systems (Broomhead & King 1986, Fraedrich 1986) in the 1980s. It was later adapted to the frequency-space (f-x) domain and relied on the separation between coherent, linear signals and incoherent noise (Cadzow 1988, Trickett 2003, Yuan & Wang 2011, Oropeza & Sacchi 2011). This algorithm is predicated on the analysis of eigen/singular values but incorporates additional phase or spatial information (Golub & Van Loan 1996, Trickett et al. 2008, Sacchi 2009). To date, SSA has found successful applications in climatology/meteorology (Vautard & Ghil 1989, Ghil et al. 2002), astronomy (Auvergne 1988, Varadi et al. 1999), and economic data series analysis (Hassani & Thomakos 2010, Kumar & Jain 2010).

Despite well-documented successes in seismic data processing (e.g., Trickett & Burroughs 2009, Oropeza & Sacchi 2011, Chen & Sacchi 2015), applications of SSA are rare in the analysis of earthquake records (Gu et al. 2015) and its potentials have not been fully recognized. In this study, we present the basic theory behind SSA and apply the SSA interpolation (an open source Julia-based package) to mantle seismic imaging. The merits of this method are demonstrated through high-frequency P-to-S conversions (Vinnik 1977, Dueker & Sheehan 1997, Rondenay 2009) and long-period shear wave reflections (Shearer 1993, Gu et al. 1998, Deuss 2009) from mantle discontinuities, both of which are known to suffer from low signal-to-noise ratios (SNR) and gaps in data coverage.

3.2 Theory

We apply singular spectrum analysis (SSA), a frequency domain noise attenuation technique, to increase the coherency of conversions or reflections from upper mantle seismic discontinuities. SSA is a model-free method that uses singular value decomposition (SVD) to reduce the rank of the Hankel matrix (Golyandina et al. (2001), Sacchi (2009)). To do so, we first represent seismic events ($d(t, x)$) in a time-space (t-x) matrix

$$\mathbf{d} = \begin{pmatrix} d_{1,1} & d_{1,2} & \cdots & d_{1,n} \\ d_{2,1} & d_{2,2} & \cdots & d_{2,n} \\ \vdots & \vdots & \ddots & \vdots \\ d_{m,1} & d_{m,2} & \cdots & d_{m,n} \end{pmatrix} \tag{3.1}$$

where $d_{j,i}$ corresponds to the jth sample of the ith trace of the data matrix composed of m samples in each seismogram for n total traces. The data in the $t - x$ domain are then transformed to the frequency-space ($f - x$) domain by taking the Fourier transform of each seismogram with respect to time. The $f - x$ transformed data matrix is now

$$\mathbf{D} = \begin{pmatrix} D_{1,1} & D_{1,2} & \cdots & D_{1,n} \\ D_{2,1} & D_{2,2} & \cdots & D_{2,n} \\ \vdots & \vdots & \ddots & \vdots \\ D_{M,1} & D_{M,2} & \cdots & D_{M,n} \end{pmatrix}, \tag{3.2}$$

where $D_{j,i}$ corresponds to the *jth* frequency sample of the *ith* trace. A related trajectory matrix, i.e., the Hankel matrix where each skew-diagonal is constant, can be constructed at a fixed frequency f_j as (Sacchi 2009):

$$\mathbf{M}(f_j) = \begin{pmatrix} D_{j,1} & D_{j,2} & \cdots & D_{j,K} \\ D_{j,2} & D_{j,3} & \cdots & D_{j,K+1} \\ \vdots & \vdots & \ddots & \vdots \\ D_{j,L} & D_{j,L+1} & \cdots & D_{j,n} \end{pmatrix}. \tag{3.3}$$

In this expression L and K are chosen to be $\lfloor$n/2$\rfloor$+1 and n-L+1, respectively, to approximate the Hankel matrix as a square matrix (Trickett & Burroughs 2009, Oropeza & Sacchi 2011). In the presence of a linear event, it can be shown that:

$$D_{j,n} = (e^{-i2\pi f_j p \Delta x}) D_{j,n-1}, \tag{3.4}$$

where p is the ray parameter and Δx is the distance between two adjacent traces. In other words, for equally spaced traces, the event becomes linearly predictable in the spatial direction (Sacchi 2009) and the rank of the Hankel matrix equals to 1. Equation (3.3) can be written in a reduced-rank form as (Sacchi 2009):

$$\mathbf{M}(f_j) = \begin{pmatrix} D_{j,1} & WD_{j,1} & \cdots & W^{K-1}D_{j,1} \\ D_{j,2} & WD_{j,2} & \cdots & W^{K-1}D_{j,2} \\ \vdots & \vdots & \ddots & \vdots \\ D_{j,L} & WD_{j,L} & \cdots & W^{K-1}D_{j,L} \end{pmatrix}, \tag{3.5}$$

where $W = e^{-i2\pi f p \Delta x}$. For the input data, $d(t,\, x)$ consists of k linear events and the transformed data $D(f,\, x)$ contain k complex sinusoids. Consequently, the rank of the Hankel matrix constructed from the transformed data at each frequency is equal to k (Yang & Hua 1996, Oropeza & Sacchi 2011). The rank of the trajectory matrix increases with noise and the number of missing traces (Sacchi 2009, Chen & Sacchi 2015). Furthermore, the SSA filter relies on the approximation of the Hankel matrix by another matrix of a lower rank (Golyandina et al. 2001). Assuming that the signal is linearly predictable in space (Oropeza & Sacchi 2011, Yuan & Wang 2011), rank reduction techniques can be applied to the Hankel matrix, $\mathbf{M}$, to 1) separate the random noise from coherent events and 2) reconstruct the missing observations by reducing the rank of the Hankel matrix. Subsequently, the low rank approximation of the Hankel matrix can be estimated using SVD (Freire & Ulrych 1988):

$$\widehat{\mathbf{M}}(f_j) = \mathbf{U}_k \mathbf{S}_k \mathbf{V}_k^H, \tag{3.6}$$

where $\mathbf{S}_k$ represents a diagonal matrix containing the first k largest singular values of the Hankel matrix $\mathbf{M}$ sorted in descending order, and U_k and V_k are the associated eigenvectors of $\mathbf{M}(f_j)$ (Trickett 2003). While the low-rank matrix $\widehat{\mathbf{M}}(f_j)$ is not a Hankel matrix and the structure of the original trajectory matrix is generally not preserved (Chen & Ma 2014), one can obtain the closest approximation to the Hankel matrix by averaging the anti-diagonal elements of each low rank trajectory matrix, $\widehat{\mathbf{M}}(f_j)$, and reconstruct the *ith* row of the transformed data in the *f*-*x* domain. The aforementioned process is carried out for all frequencies f_j in the band of the seismic signal. Finally, an enhanced seismic image is obtained by transforming data back to the *t*-*x* domain. An iterative algorithm similar to the one suggested by Oropeza & Sacchi (2011) is used to recover the true amplitudes of the missing traces:

$$\mathbf{D}_i = \alpha \mathbf{D}_{obs} + (1 - \alpha \mathbf{T}) F_{SSA}[\mathbf{D}_{i-1}], \quad i = 1, 2, 3, ..., itr_{max}. \tag{3.7}$$

In this equation, $\mathbf{D}_i$ and $\mathbf{D}_{i-1}$ are the interpolated data in the current and previous iterations, respectively, and $\mathbf{D}_{obs}$ denotes the input data matrix with missing observations. The operator $\mathbf{T}$ is a sampling matrix (with the size of the original data), within which the elements equal to 1.0 (where data exist) or 0.0 (otherwise). The operator F_{SSA} represents the SSA filter and the denoising parameter α is a scalar (between 0 and 1) associated with the noise level. F_{SSA} is formed by concatenating the following operators: data Hankelization, rank-reduction and anti-diagonal averaging. Finally, because a true amplitude recovery is usually not achievable after a single iteration, we employ an iterative algorithm that terminates when the maximum number of iterations itr_{max} is reached or when the normalized error function $\|\mathbf{D}_i - \mathbf{D}_{i-1}\|^2/\|\mathbf{D}_{i-1}\|^2 < \epsilon$ with $\epsilon = 10^{-6}$. Examples of SSA in mantle interface analysis will be provided in Section 3.3.

3.3 Application

A wide range of secondary seismic arrivals has been utilized to determine the structure surrounding mantle seismic discontinuities. Two prominent examples are P-to-S converted waves, often calculated from "receiver functions" (Ammon et al. 1990, Kind et al. 1996, Ligorria & Ammon 1999, Lawrence & Shearer 2006*a*, Rondenay 2009, Chen et al. 2015), and long-period *SS* precursors (Shearer & Masters 1992, Flanagan & Shearer 1998, Gu et al. 1998, Deuss & Woodhouse 2002, Houser et al. 2008) (Figure 3.1). The former phase group is usually examined at high frequencies, targeting the seismic structures beneath the receiver (Cassidy 1995, Song et al. 2004, Schaeffer & Bostock 2010, Gu et al. 2015) or source (Wicks & Richards 1993, Castle & Creager 2000) location. In comparison, *SS* precursors are "global phases" less dependent on path geometries (Shearer & Masters 1992, Gu et al. 1998, Zheng et al. 2015). Results from these two approaches are generally complementary, especially in major subduction zones (Li et al. 2000, Gu & Dziewonski 2002, Lawrence

& Shearer 2006*a*). The section below investigates the effectiveness of SSA in the waveform analyses of receiver functions (RF) and *SS* precursors for the imaging of mantle transition zone (MTZ) discontinuities (Ringwood 1975, Dziewonski & Anderson 1981).

3.3.1 *P*-to-*S* Receiver Function

Receiver function analyses have been widely used to constrain the properties of upper mantle interfaces (Langston 1979, Vinnik 1977, Lawrence & Shearer 2006*a*, Tauzin et al. 2008, Schaeffer & Bostock 2010, Gu et al. 2015). The primary conversions from mantle discontinuities are often difficult to identify due to low SNR and potential effects of multiple reverberations or interfering phases (Schaeffer & Bostock 2010). Hence, stacking is generally performed to enhance the SNR and reduce the random noise, but its effectiveness can be compromised under severe noise levels and/or a non-Gaussian noise distributions. Figure 3.2a shows a record section of synthetic RFs containing P-to-S converted phases from mantle interfaces, calculated using a propagator matrix approach (Kennett 1983, Shearer 2009) based on PREM (Dziewonski & Anderson 1981) for source-receiver distances ranging from 45 to 95 degrees. After normalizing and aligning of each seismogram by its peak amplitude, the move-out of the converted phases becomes approximately linear across the record section. We then decimate the data by randomly removing 34% of the traces and contaminate the selected records by 10% Gaussian noise (Figure 3.2b). A comparison between the reconstructed data (Figures 3.2c-3.2h) suggests that the best performance of the SSA interpolation is achieved using the 3 largest singular values; in other words, the optimal desired rank of the Hankel matrix is $k = 3$. On the other hand, the presence of random noise increases the non-zero singular values of the trajectory matrix (Figures 3.3a and 3.3b). To assess the quality of the reconstructions for different ranks, we define

$$Q = 10log\frac{\|\mathbf{d}_0\|^2}{\|\mathbf{d}_0 - \hat{\mathbf{d}}\|^2} \tag{3.8}$$

where $\mathbf{d}_0$ and $\hat{\mathbf{d}}$ denote the noise-free and reconstructed data in the $t - x$ domain, respectively. By this definition, Q approaches infinity in the case of perfect data reconstruction. In this experiment, the calculated Q values for the interpolated data using rank $k = 1$, 2 and 3 are 2.3, 3.6 and 4.6 dB, respectively, suggesting that the highest quality of reconstruction is achieved when $k = 3$. Further increases of rank k lead to systematic decreases in Q due to the elevated levels of recovered noise in the data (Figure 3.3c).

In a second experiment, we utilize a data-set of 1563 high-quality RFs, collected from 6 broadband, three-component seismic stations from the Canadian Rockies and Alberta Network (CRANE; Gu et al. (2011)) and Canadian National Seismograph Network (CNSN). This data-set has been previously examined by Gu et al. (2015) to map the mantle stratigraphy beneath the Western Canada Sedimentary Basin (WCSB). The availability of the published results enables us to quantitatively assess the performance of SSA in noise reduction and reflectivity imaging. We group the RFs into the common receiver gathers and sort them by source-receiver distances. The resulting source-receiver distances are not regularly spaced, which does not satisfy the spatial sampling requirement of SSA (Oropeza & Sacchi 2011). Hence, prior to SSA, we partially stack the traces using a 1-degree running average window. Figures 3.4 and 3.5 show the comparison between the raw RFs and the reconstructed data using SSA interpolation. The rank of the trajectory matrix, k, is determined based on the synthetic experiments and the number of expected linear arrivals in the data section. The input partial stacks (especially those observed at the stations CZA, NOR, PER and SLEB) show no discernible mantle conversions

Table 3.1: Polynomial Coefficients of linear and parabolic fits calculated for *SdS* travel times and path functions using PREM (Dziewonski & Anderson 1981) and IASP91 (Kennett & Engdahl 1991). The coefficients p_0, p_1 and p_2 are sorted in an ascending order, i.e., *SdS* differential times are calculated as $p_0+p_1x+p_2x^2$ (where x represents the source-receiver distance in degrees). The coefficient of determination, R^2, indicates the goodness of fit of each trajectory. R^2 reflects the performance of the regression curve in predicting variations in the original data and it is defined as the normalized variance reduction (Gu & Shen 2015).

		PREM				IASP91			
		p_0	p_1	p_2	R^2	p_0	p_1	p_2	R^2
S410S	linear	-120.8	-0.2523	0.0	0.9988	-123.5	-0.2588	0.0	0.999
	Parabolic	-111.6	-0.3956	0.00055	1.0	-114.9	-0.3947	0.000523	1.0
S660S	Linear	-169.7	-0.4887	0.0	0.9985	-167.9	-0.479	0.0	0.9987
	Parabolic	-149.6	-0.8035	0.00121	1.0	-150.0	-0.7606	0.00108	1.0

due to low SNRs and gaps in the sections of partially stacked RFs. Aside from the successful removal of data gaps, the SSA reconstruction generally enhances the signals associated with mantle conversions (i.e., *P410s*, *P660s* and converted phases from mid-MTZ depths) while effectively reducing the random noise.

3.3.2 *SS* Precursor

Similar to converted phases, the SSA algorithm can also be directly applied to the waveforms of long-period reflections from mantle interfaces. To illustrate this, we calculate a record section of 60 transverse-component seismograms from 100 to 160 degrees of source-receiver distances using PREM (Dziewonski & Anderson 1981) (Figure 3.6a). After the precursor (*SdS*) waveforms are aligned on the peak amplitudes of *SS*, the relative travel times of *SS* precursors can be accurately represented using parabolic functions of epicentral distance (Gu & Sacchi 2009). Based on statistical measures of the goodness of fit (which is defined as R^2 in Table 3.1), however, the differential travel times of *SdS*-*SS* can be further approximated using linear path functions (where the quadratic term is essentially zero).

In the first experiment, we randomly remove 30% of traces and add 10% Gaussian noise to the input section (Figure 3.6b). After the SSA interpolation, the main linear arrivals (e.g., *S410S* and *S660S*) and nearly 93% of their input amplitudes are properly recovered using $k = 1$ at well sampled distances (Figures 3.6c and 3.6d). The topside reflections from the mantle discontinuities (*S410sSdiff/SdiffS410s* and *S660sSdiff/SdiffS660s*, also known as *Sdiff* postcursors (Zheng et al. 2015)) that interfere with *SdS* at distances <130 degrees, are clearly associated with the second largest singular values of the trajectory matrix (Figures 3.6e and 3.6f). Unlike converted waves, only two singular values are needed to recover the key arrivals within the precursor time window.

Figure 3.7 shows the SSA reconstruction of *SS* precursor waveforms from northeastern China. This data-set was recently analyzed by Dokht et al. (2016) in imaging the upper mantle beneath the Changbai/Wudalianchi hotspots. The input record sections (Figures 3.7a and 3.7b), which are obtained from partial stacking, show a series of secondary reflections (i.e., *SS* precursors) prior to the surface reflections. The reconstructed waveforms adequately recover the missing traces in the data gap between the 140 and 145 degrees (Figures 3.7c and 3.7d). Strong signals are also observed between *S410S* and *S660S*, in potential association with a mid-MTZ reflector near 520 km depth (see Figure 3.7c, Gu et al. (2012)). The depths of the discontinuities from the stacks of depth-converted *SS* precursors, calculated using the waveform data presented in Figure 3.7, agree to 99% before (Figures 3.8a and 3.8b) and after (Figures 3.8c and 3.8d) SSA. In comparison with stacks from the original data, SSA enhances the amplitudes of the mantle reflections by an average of 33% and significantly improves their accuracy (see Figure 3.8). The reconstructed data properly recover the major depth anomalies on the discontinuities, i.e., depressions of the MTZ boundaries under the Wudalianchi hotspot, that can be directly linked to the dynamic processes in association with plate convergence.

3.3.3 Limitation and Complication

Like most noise reduction/data reconstruction methods, the effectiveness of SSA is strongly dependent on the data condition (e.g., receiver density/spacing and noise characteristics). To examine the performance of SSA in recovering missing traces, we generate a synthetic seismic section with a single linear event (Figure 3.9a) and reduce the data density to 50% by 1) removing every other trace (Figure 3.9b) and 2) random decimation (Figure 3.9c). The resulting Hankel matrix from the regularly decimated data at a constant frequency of 0.04 Hz (i.e., case 1, Figure 3.9e) is of rank 2. Only the first two singular values of the Hankel matrix are non-zero, although the amplitude of largest singular value is approximately half of the original one (see Figures 3.9g and 3.9h). The second largest singular value at each frequency is associated with zero skew-diagonal elements of the Hankel matrix due to the alternate removal of the input traces (see Figures 3.9e and 3.9h). In comparison, the Hankel matrix constructed from the randomly sampled data shows a higher rank than both the original and uniformly decimated data (see Figures 3.9g-3.9i). However, the Hankel matrix is less structured than that with regular data gaps, and is therefore able to preserve the desired signal. The inability of SSA in recovering the regular data gaps is further illustrated by the results of data reconstruction (Figure 3.10a). The amplitudes of the interpolated missing traces are approximately zero for all distances. In comparison, the reconstruction in the case of irregular data gaps is more accurate (Figure 3.10b). A proper application of SSA on regularly decimated data will require more advanced techniques such as anti-aliasing Cadzow reconstruction (Naghizadeh & Sacchi 2013). For most solid Earth applications, the SSA algorithm examined in this study is sufficient since the distributions of earthquakes and seismic stations are rarely uniform.

It is worth noting that the accuracy of data reconstruction is strongly dependent on the percentage of missing traces (i.e., non-regular data gaps). For a seismic section consisting of two linear arrivals (Figure 3.11a), the quality of the results decreases linearly from $\sim$6.5 dB at 10% data gaps to $\sim$5.3 dB at 50% (Figure 3.11b), below which the quality of the reconstruction drops off more rapidly (see Figures 3.11b and 3.11h). For instance, when 70% of data are missing, SSA is only able to properly recover the timing of the seismic arrivals while the amplitudes of the interpolated traces within data gaps are considerably underestimated (see Figures 3.11g and 3.11h).

To further quantify the performance of SSA in the presence of noise, we contaminate the synthetic section containing a single linear event (Figure 3.12a) with random noise at SNR values of 1 to 6. In all cases, the qualities of the filtered sections are improved through the application of SSA (Figures 3.12b-3.12f). The improvement in the image quality is especially significant at SNR = 1 (see Figure 3.12f) where SNR after filtering is improved by nearly 3 fold. Just as importantly, no coherent arrivals are observed on the residual section (Figures 3.12g and 3.12h), which suggest minimal systematic biases during the reconstruction. Further examinations of the α parameter and spurious outliers are provided in Appendix B (see also Figures B.1-B.3).

3.4 Conclusion

In this study, the upper mantle discontinuities are imaged using SSA, a rank reduction approach that simultaneously removes random noise and reconstructs missing data traces. This method relies on the predictability of mantle conversions and reflections, and it is implemented in the frequency-space domain. The reconstructed seismic images of the upper mantle show more laterally coherent observations of MTZ discontinuities on both the waveforms of *SS* precursors and receiver functions. In addition to consistent MTZ phase boundaries, strong signals near the 520 km discontinuity are successfully identified beneath western Canada and NE China. When utilized properly, this method could be a powerful tool for future analyses of any weak seismic phase from the Earth's interior. Scripts to perform SSA in the frequency-space domain are presented in Julia, which provides free access to open source libraries and portability between different platforms (https://sites.ualberta.ca/∼ygu/projects/ssa/).

The research detailed in this Chapter has been previously published in: Dokht, R. M., Gu, Y. J., & Sacchi, M. D. (2016), Singular Spectrum Analysis and its applications in mapping mantle seismic structure, *Geophysical Journal International*, ggw473, doi: 10.1093/gji/ggw473.

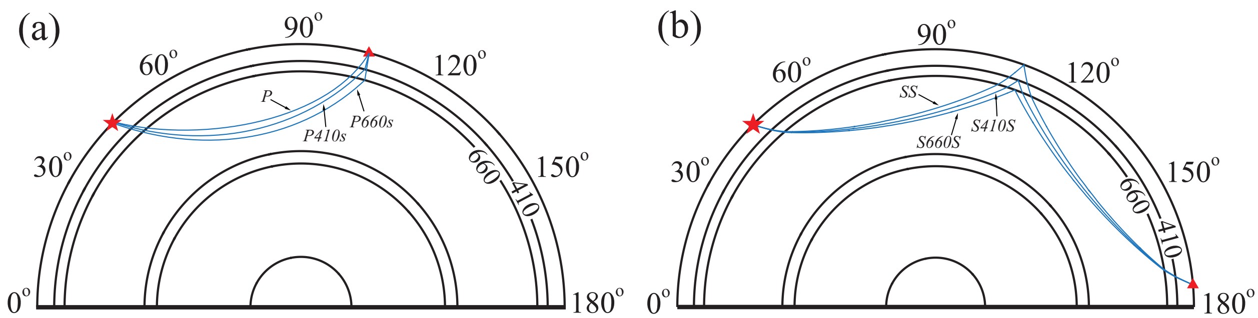

Figure 3.1: (a) Theoretical ray paths of P and P-to-S conversions at a 60-degree epicentral distance. (b) Ray paths of SS and its precursors at a 130-degree distance. These ray paths are computed using PREM (Dziewonski & Anderson 1981). The stars and triangles denote the earthquake and seismic station locations, respectively.

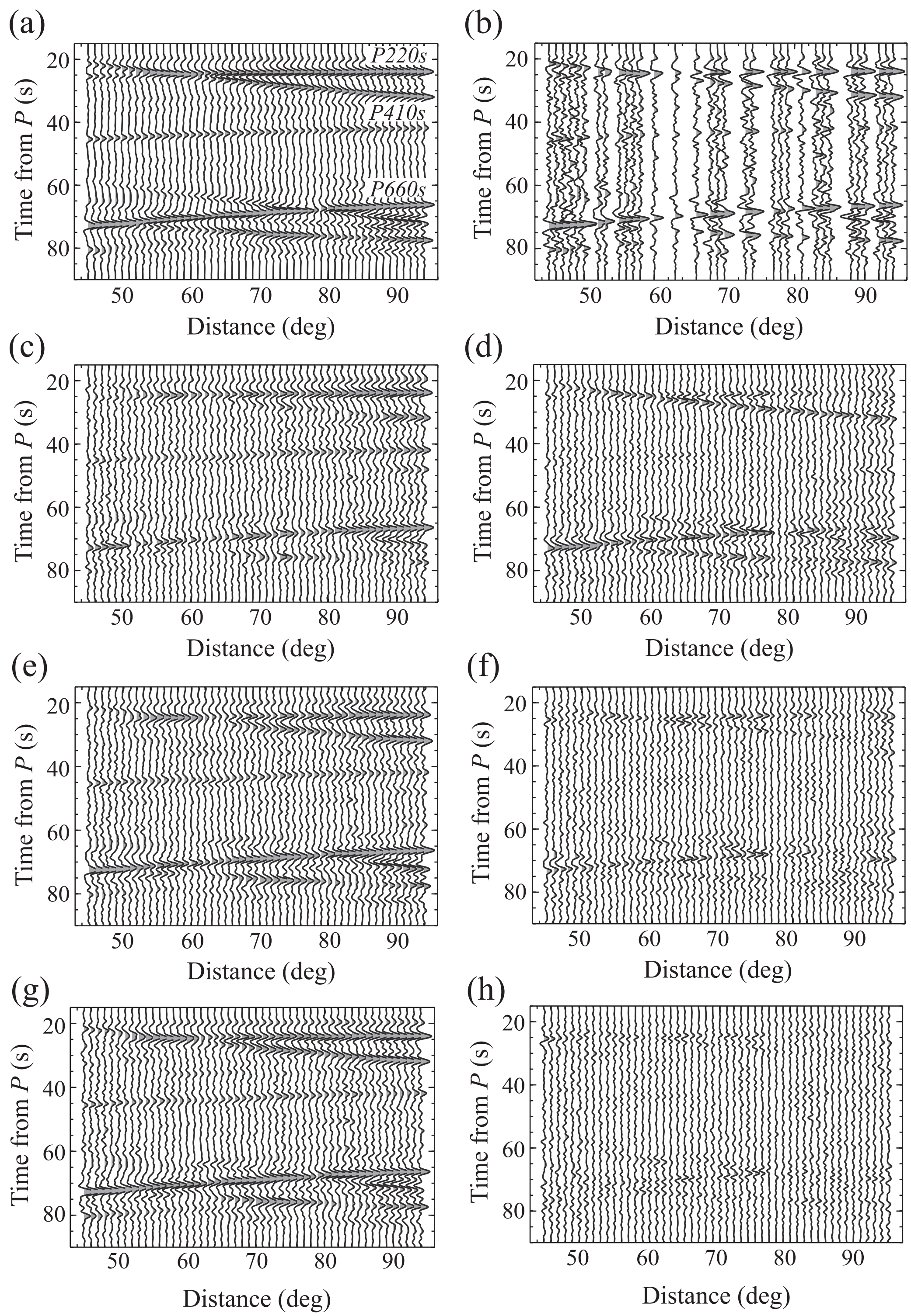

Figure 3.2: Application of SSA on a decimated record section of synthetic receiver functions contaminated with random noise. (a) Original data. (b) Noise-added data decimated to ∼70% of the original number of traces. (c), (e) and (g) Results of SSA filtering at k values of 1, 2 and 3, respectively. (d), (f) and (h) The corresponding differences between the reconstructed (c, e and g) and original (a) data.

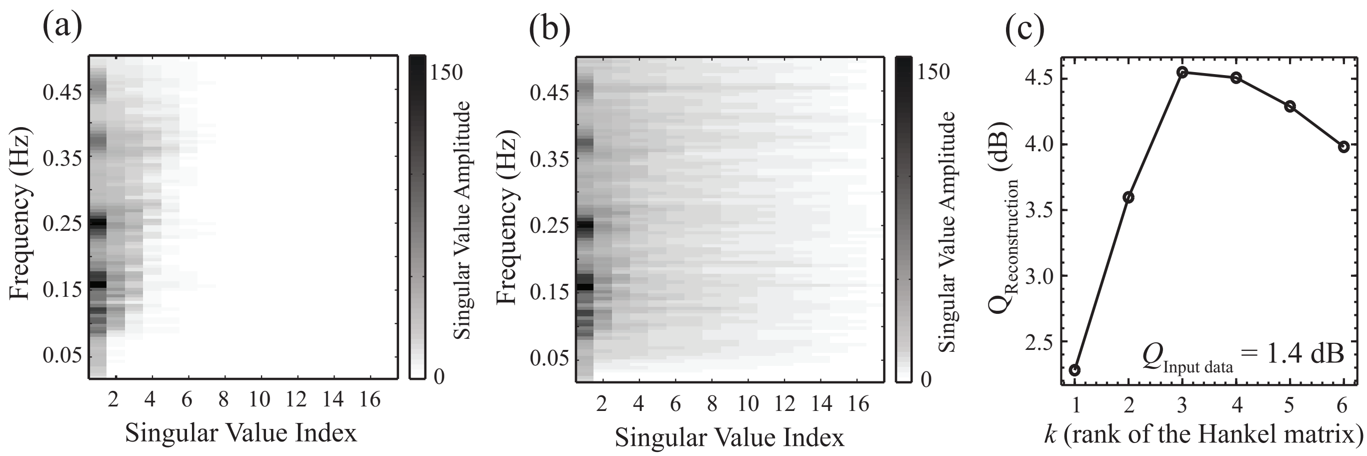

Figure 3.3: Distributions of singular values for (a) noise-free synthetic receiver functions and (b) noise-added, decimated data presented in Figure 3.2. (c) Quality of the reconstruction (Q) versus the rank of the Hankel matrix (k). The input data show a Q value of 1.4 dB. The maximum value of Q is achieved at $k = 3$.

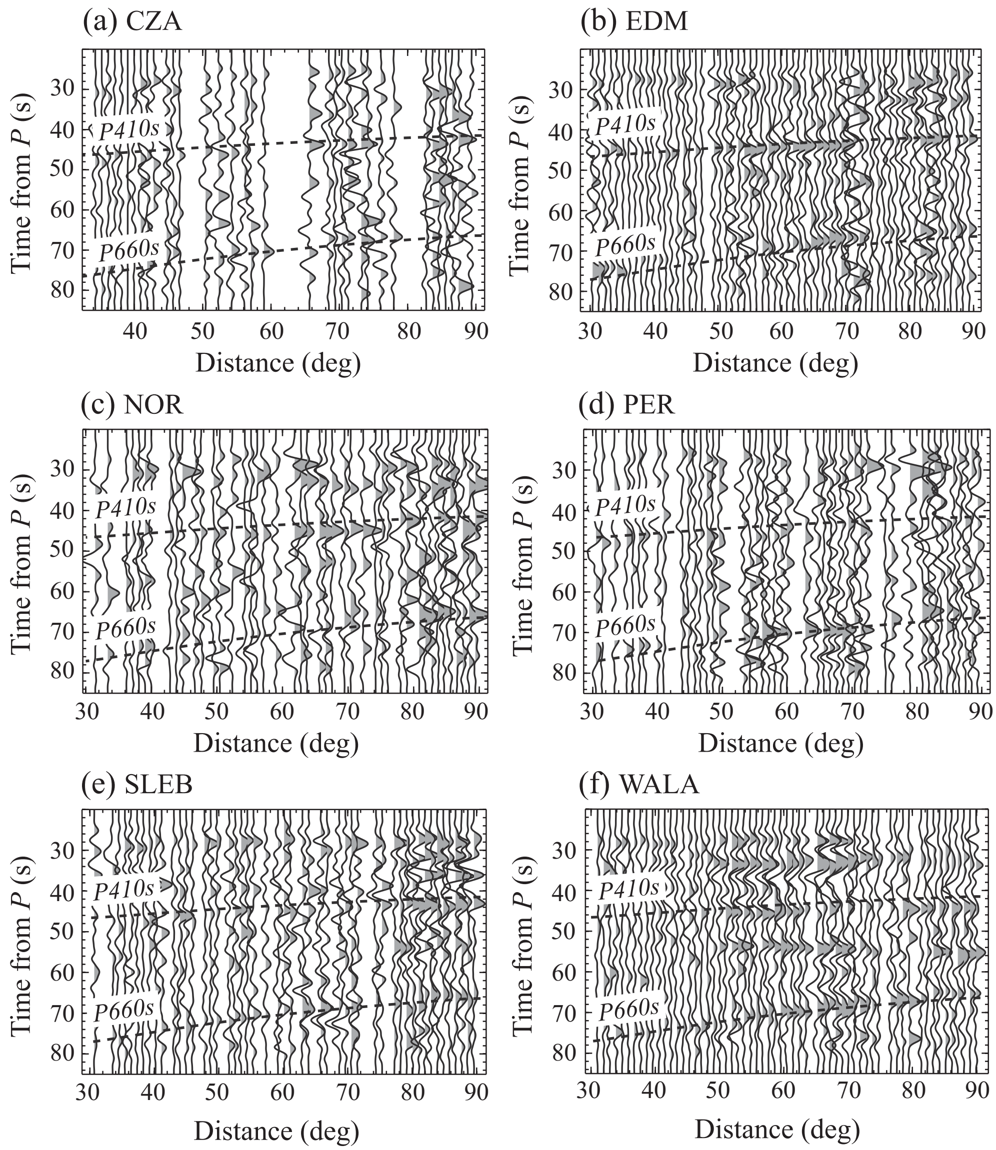

Figure 3.4: Partially stacked radial receiver functions calculated for six seismic stations in southwestern Canada. Approximately 40%, 2%, 30%, 25%, 21% and 3% of data are missing at the stations CZA, EDM, NOR, PER, SLEB and WALA, respectively. The dashed lines indicate the PREM predicted differential travel times of *P410s-P* and *P660s-P* (Dziewonski & Anderson 1981).

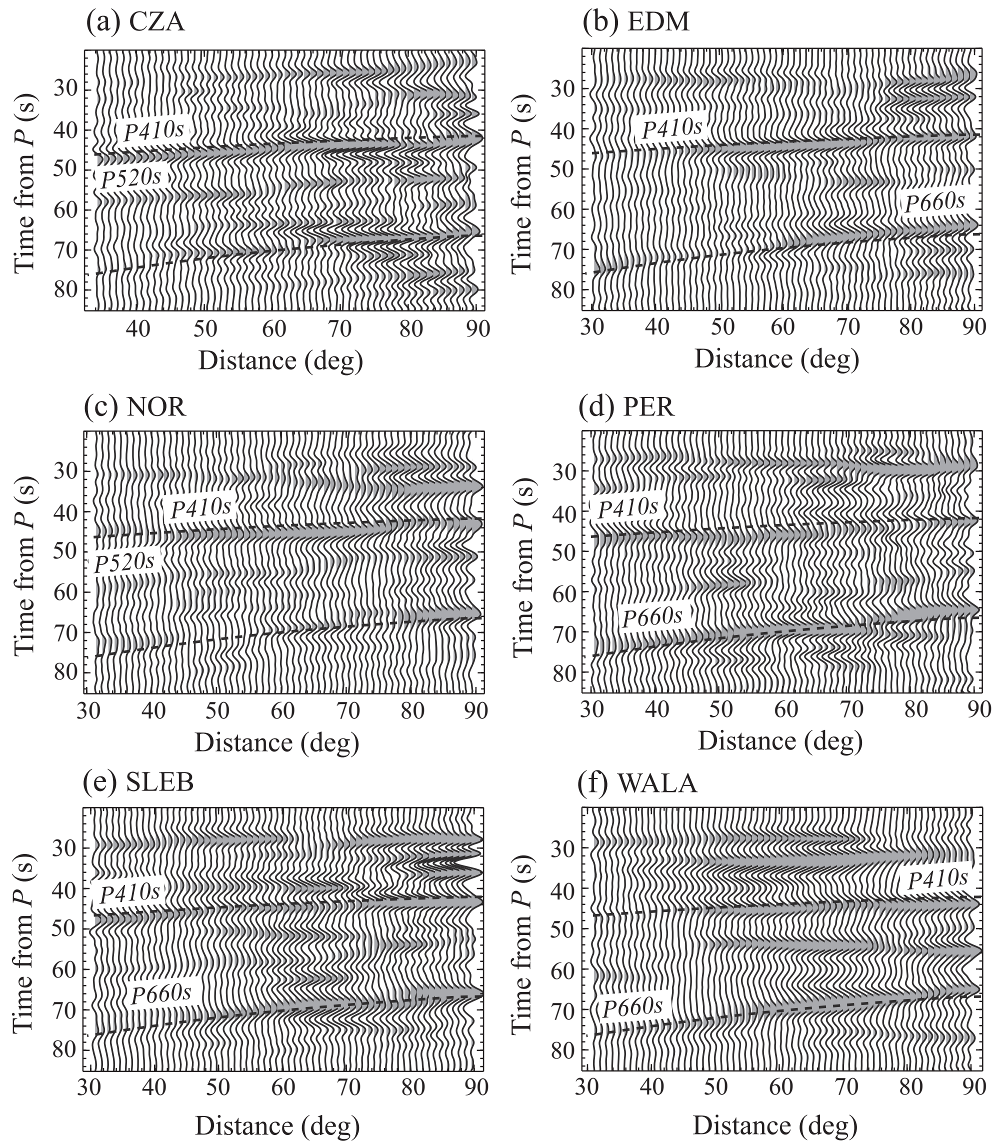

Figure 3.5: Reconstructed and spatially resampled receiver functions by applying the SSA interpolation. SSA is designed to reduce the rank of the Hankel matrix to 3. The dashed lines indicate the PREM predicted differential travel times of *P410s-P* and *P660s-P* (Dziewonski & Anderson 1981).

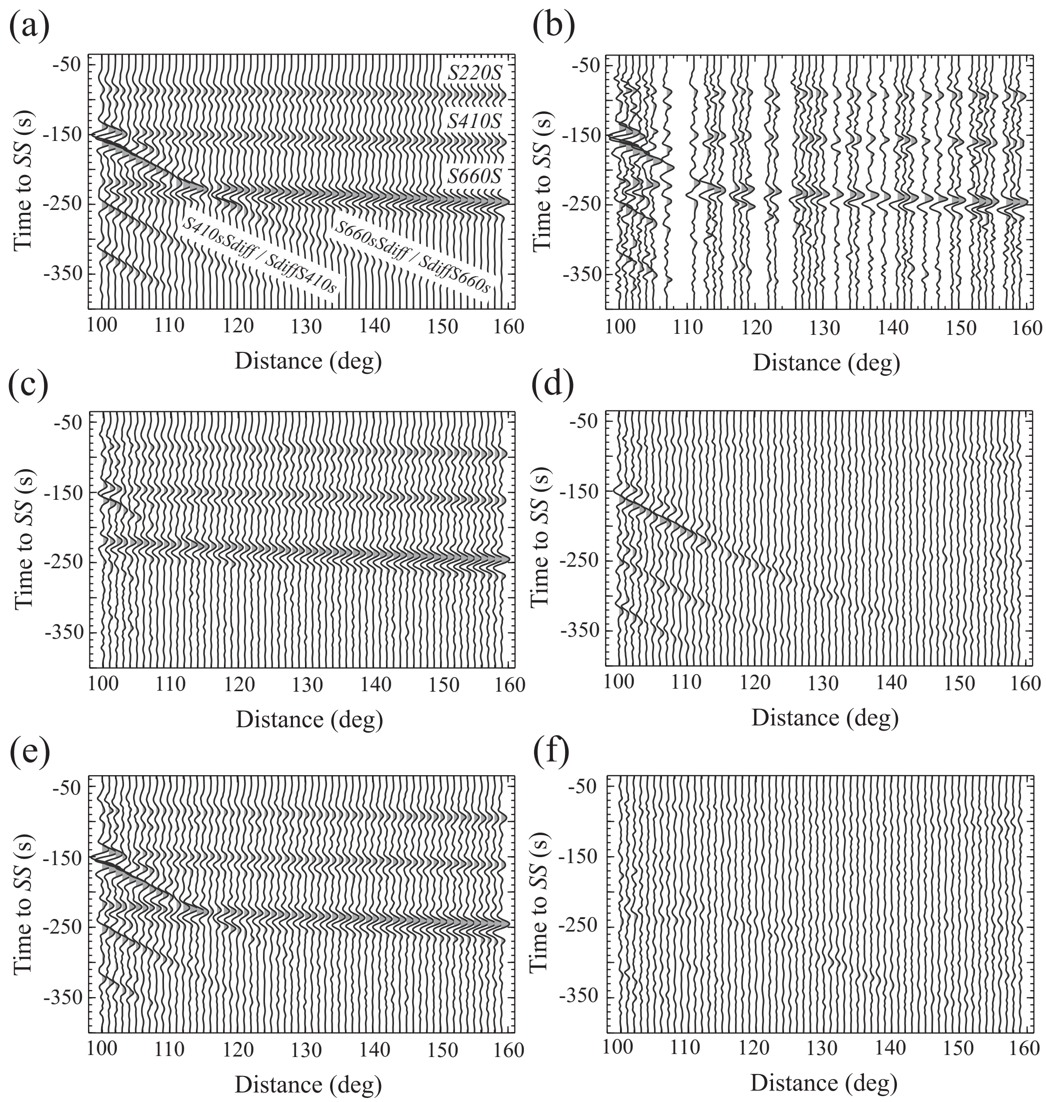

Figure 3.6: Application of SSA on synthetic *SS* precursor waveforms contaminated with random noise. (a) Noise-free synthetic records. (b) Noise-added data with 30% of the traces randomly removed. (c) and (e) Reconstructed data from (b) using k = 1 and 2, respectively. (d) and (f) Differences between the reconstructed data (c and e) and original input waveforms (a).

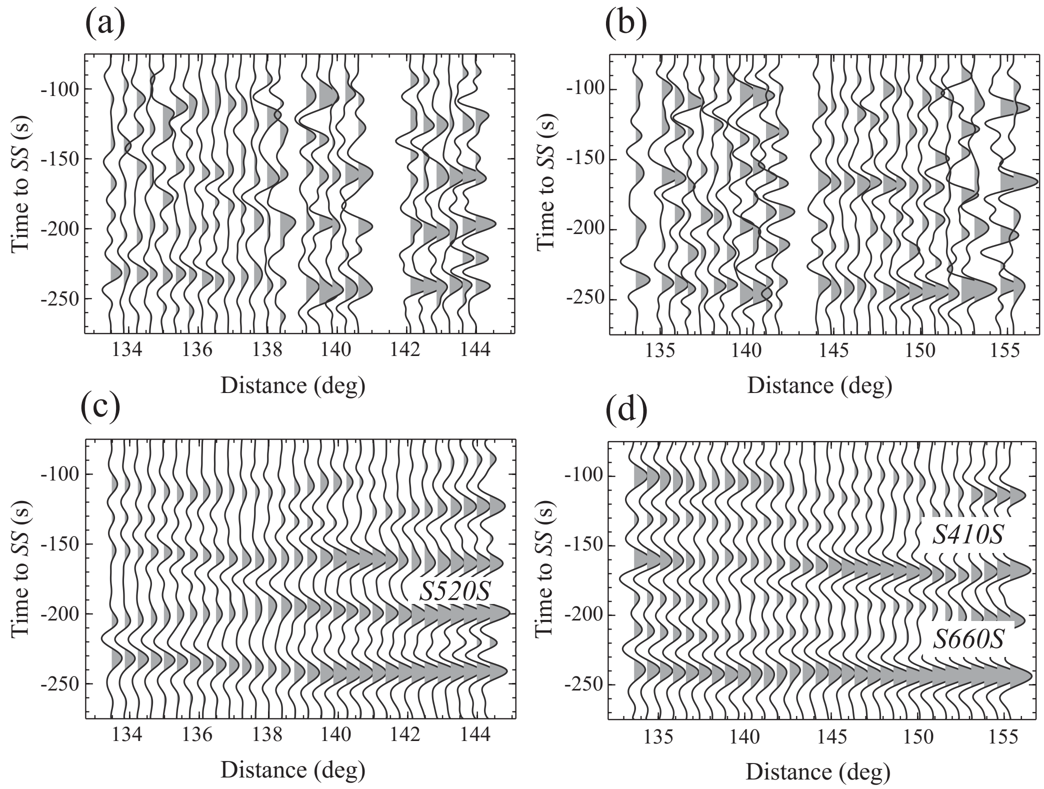

Figure 3.7: (a) and (b) Partially stacked SS precursor waveforms sampling the upper mantle beneath the Wudalianchi hotspot in northeastern China. The running average window sizes are 0.5 and 1.0 degree, respectively, for (a) and (b) with 25% overlaps among the adjacent windows. (c) and (d) Reconstructed SS precursor waveforms from (a) and (b), respectively, using $k = 2$.

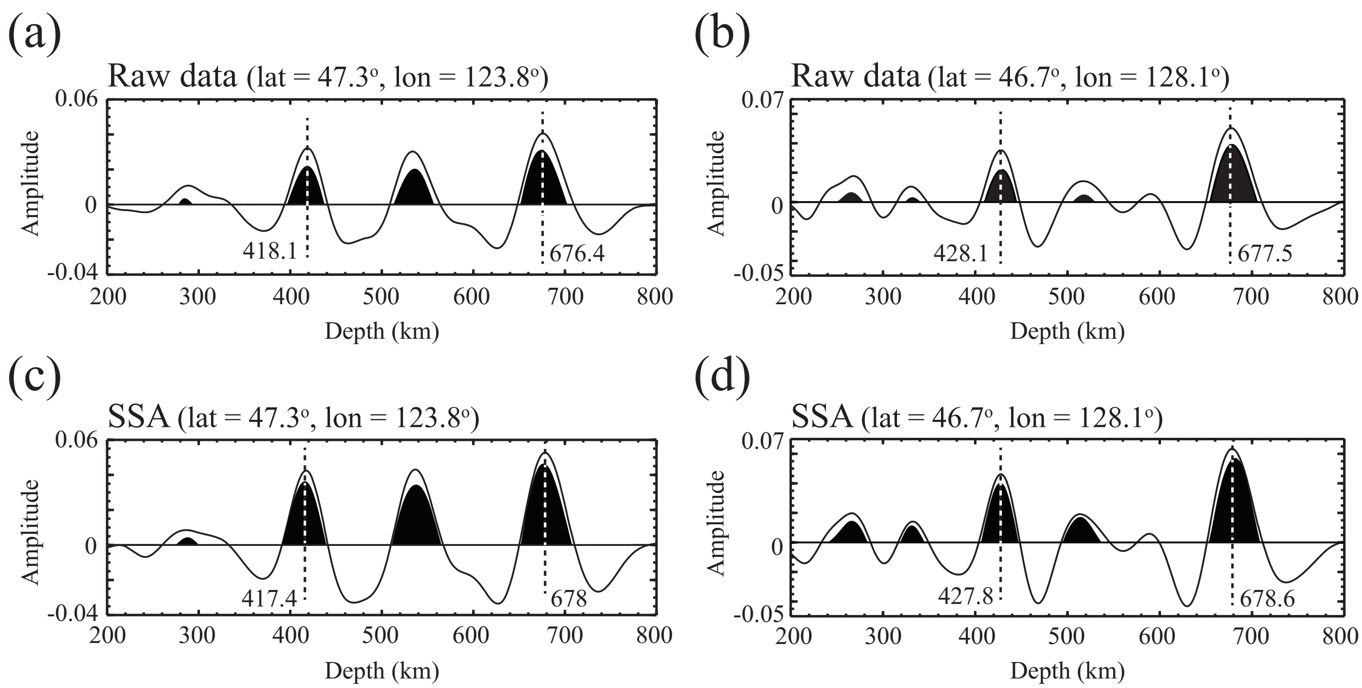

Figure 3.8: Stacks of depth-converted *SS* precursor waveforms before (panels (a) and (b)) and after (panels (c) and (d)) SSA. The stacked seismograms are calculated using the data presented in Figure 3.7. The center locations of the data gathers are as indicated. The shaded areas show the 95% confidence intervals calculated using the bootstrapping resampling algorithm (Efron & Tibshirani 1991).

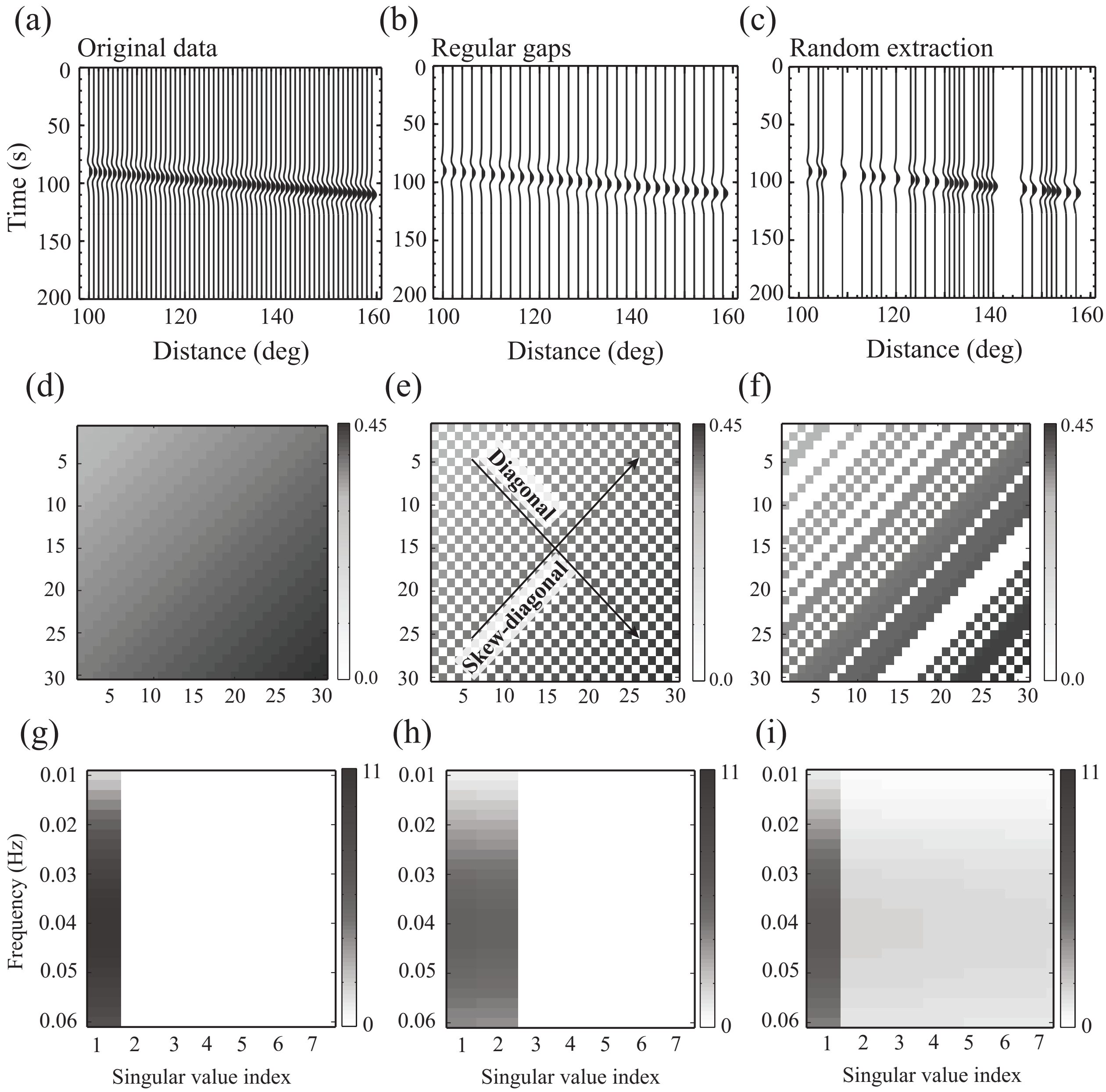

Figure 3.9: (a) Original data containing a linear event. (b) Modified data with regular gaps (50% decimation). (c) Modified data after 50% random extraction. (d)-(f) The corresponding Hankel matrices from (a)-(c) at 0.04 Hz frequency. (g)-(i) Distributions of the singular values calculated from (d)-(f).

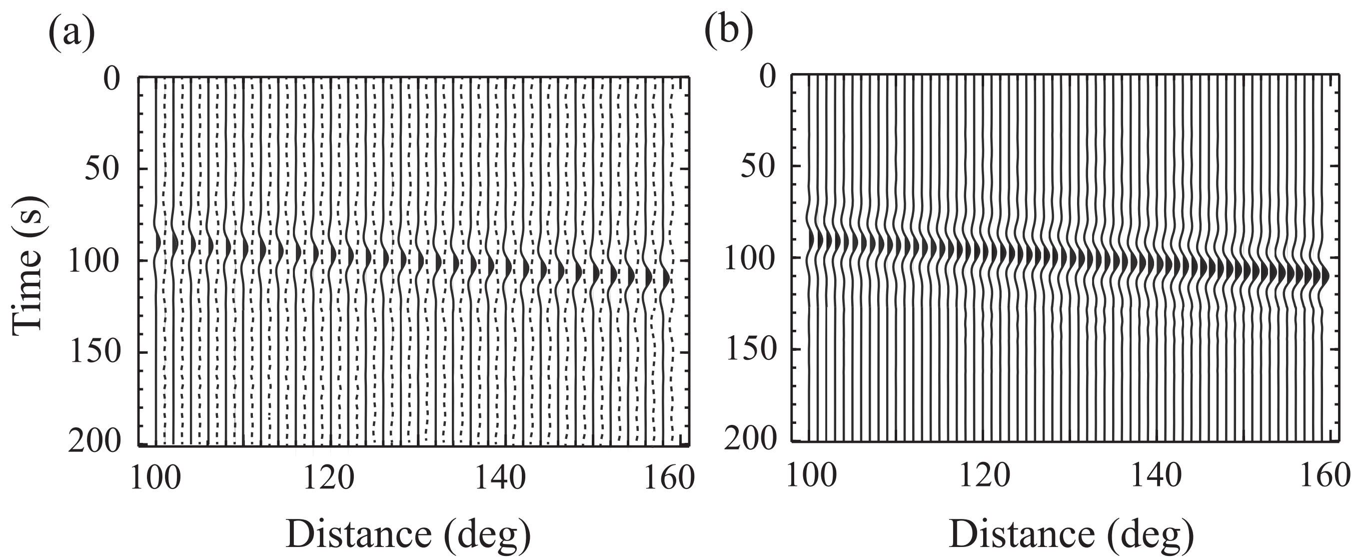

Figure 3.10: A comparison between the SSA interpolation results for (a) regularly and (b) randomly decimated data using $k = 1$. The dashed lines in panel (a) represent the interpolated missing traces.

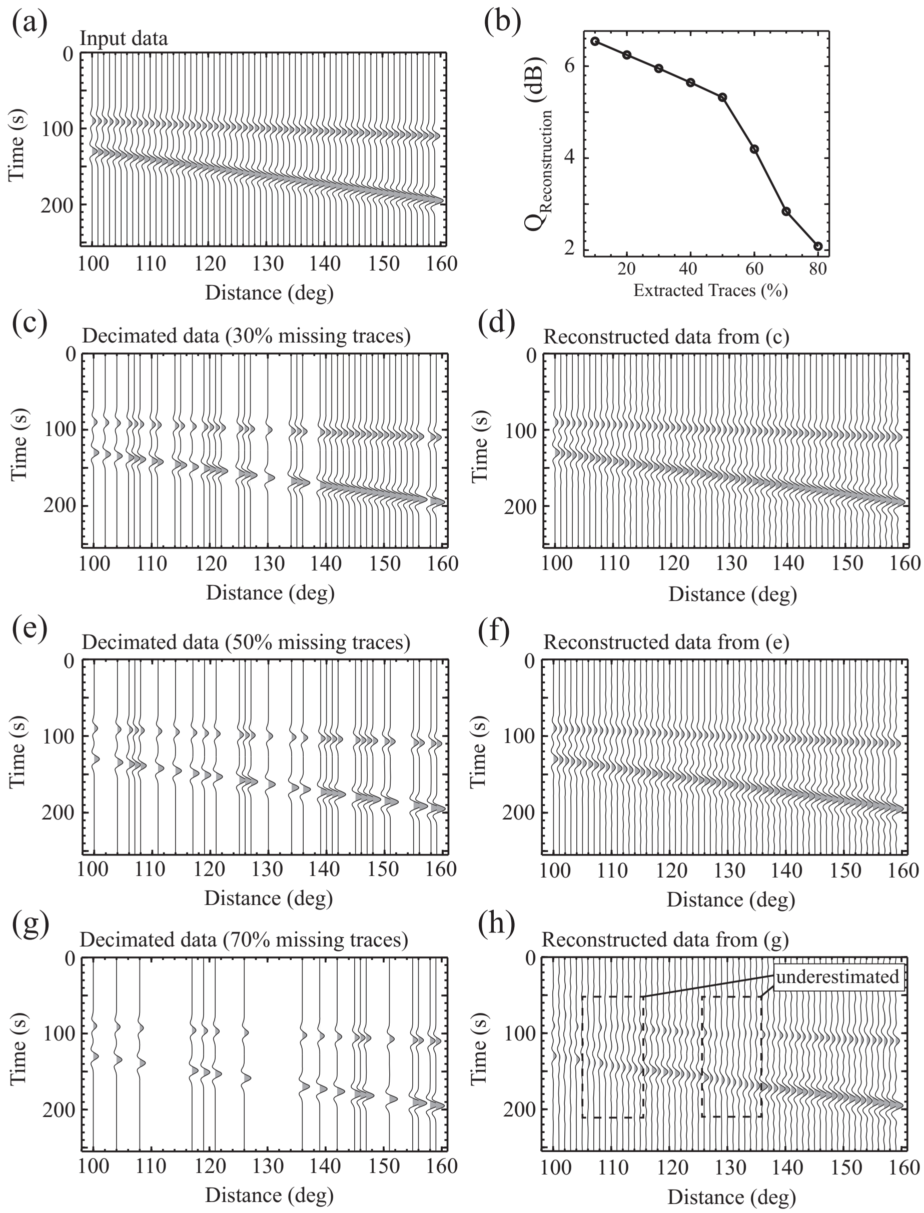

Figure 3.11: The effectiveness of SSA under increasing numbers of missing data traces. (a) Original data. (b) Quality of the reconstructed data versus the percentage of missing traces. (c), (e) and (g) Input data with 30%, 50% and 70% empty entries, respectively. (d), (f) and (h) The corresponding interpolated data from (c), (e) and (g) using $k = 2$.

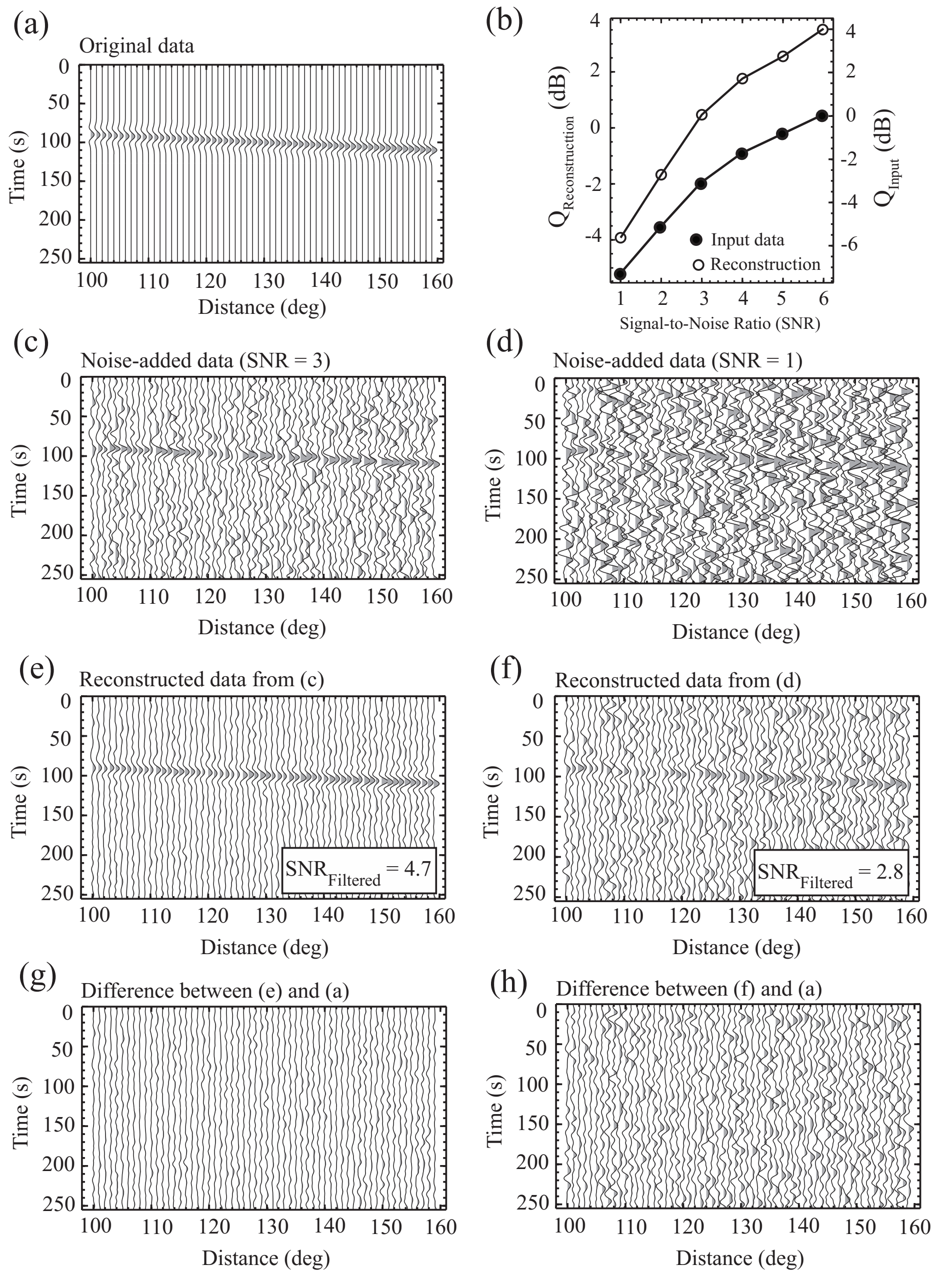

Figure 3.12: Applications of SSA in filtering data that have been contaminated with additive random noise. (a) Original noise-free data. (b) Quality of the input and filtered data for different SNR values. The filled and open circles show the respective qualities of the input noisy data and the reconstructions. The noise added data with SNR $= 3$ and 1 are shown in panels (c) and (d), respectively, and their corresponding filtered sections (using $k = 1$) are shown in panels (e) and (f). (g) and (h) Differences between the filtered and noise-free data.

Chapter 4

Migration imaging of the Java subduction zones

4.1 Introduction

The Sunda trench, located in Southeastern (SE) Asia, is an active convergent plate margin marked by the subduction of the Indo-Australian oceanic lithosphere (slab) beneath the Eurasian plate (Curray et al. 1979, Bird 2003, Simons et al. 2007). The trench extends along-strike for over 5000 km from the Andaman islands to the west of the active Banda arc (Widiyantoro et al. 2011*b*), which is identifiable by its 180° curvature resulting from the collision between the northward migrating Australian continental plate and the arc in the Early Pliocene (Katili 1975, Spakman & Hall 2010). The estimated age of the subducting oceanic lithosphere varies along the trench and decreases from the Late Jurassic (134-154 Ma) in southern Sumatra to the Late Cretaceous (78-100 Ma) in Bali (Widiyantoro & van der Hilst 1996, Hall & Spakman 2015). Plate motion models constructed from seafloor spreading rates, transform fault azimuths, and global positioning system measurements indicate a relatively high convergence rate between the Indo-Australian and Eurasian plates that increases from 5.5 cm/year in Sumatra to 7.3 cm/year near Timor (Minster & Jordan 1978, Bock et al. 2003, DeMets et al. 2010) (Figure 4.1). The morphology and penetration depth of subducted lithosphere are well defined by the earthquake hypocenters that vary substantially along the strike of the plate boundaries. East of Java, the subducted oceanic lithosphere can be traced down to the base of the mantle transition zone, whereas the seismicity is predominantly confined to the top 300 km beneath central and western Sumatra (Hamilton 1974, Cardwell & Isacks 1978). The subducting oceanic lithosphere is further evidenced by the presence of a high velocity zone (Puspito et al. 1993, Widiyantoro & van der Hilst 1996, Amaru 2007, Fichtner et al. 2010, Lekić & Romanowicz 2011, Fukao & Obayashi 2013), which appears to penetrate into the lower mantle at a near-vertical angle beneath Java and Bali and potentially flattens at an approximate depth of 1500 km (Puspito & Shimazaki 1995, Widiyantoro & van der Hilst 1997, Replumaz et al. 2004). In contrast, the slab beneath the Banda trench exhibits a shallower angle and its seismic signature can mainly be detected within and above, but not below, the MTZ (Spakman & Hall 2010).

Characteristics of the MTZ seismic discontinuities offer additional constraints on the morphology and thermochemical effects of the Sunda slab. In an olivine-dominated upper mantle, the solid-solid phase transitions from olivine to β-spinel and γ-spinel to perovskite+magnesiowustite mark the upper and lower boundaries of the MTZ at the nominal depths of 410 and 660 km, respectively (Anderson 1967, Jeanloz & Thompson 1983, Ito & Takahashi 1989). Due to their opposite Clapeyron slopes, the thickness of MTZ is expected to increase in cold areas (e.g., subducting slabs) and decrease in warm regions (e.g., upwelling plumes) (Ito & Takahashi 1989, Katsura & Ito 1989). For this reason, the topography of the 410 km and 660 km seismic discontinuities (for short, the 410 and the 660) have been widely investigated through converted (Saita et al. 2002, Lawrence & Shearer 2006*a*) and reflected (Flanagan & Shearer 1998, Gu et al. 2003, Houser et al. 2008) waves. Both types of observations indicate a local thickening of the MTZ along Java and southeastern Sumatra, ranging from 20-55 km and coinciding with the presence of a high velocity anomaly within the MTZ (Widiyantoro & van der Hilst 1996, Fukao & Obayashi 2013). Based on P-to-S converted waves (Saita et al. 2002), a narrow MTZ is found beneath northern Borneo and western Sulawesi, while the earlier observations from mantle reflections suggested that the thickness of the MTZ could increase by up to 20 km in the same region (Gu et al. 2003, Houser et al. 2008, Lawrence & Shearer 2008).

Limited station distribution, lateral smoothing and low data density remain major hurdles in the interrogation of the MTZ structure and dynamics in the Sunda arc subduction system. In this study we investigate the topography of the 410 and 660 beneath SE Asia from the prestack depth migration of *SS* precursor waveforms. We demonstrate that the migration process using an array of precursors can effectively reduce the size of the Fresnel zone and enhance the resolution, which provides a critical window into the complex geometry and mantle temperature associated with the Sunda arc subduction.

4.2 Data and Method

4.2.1 Data Selection

Our main observational constraint is *SS* precursors, which are shear wave underside reflections off the upper mantle interfaces near the midpoint between the earthquake and receiver (Shearer 1993, Flanagan & Shearer 1998, Gu et al. 1998) (Figure 4.2a). The precursors arrive before the main *SS* phase (i.e., surface reflection) due to their shorter propagation paths. We include broadband, long-period SH-polarized seismograms from Mw >5.5 earthquakes recorded between 1990 and 2015, with epicentral distances ranging from 80° to 160°. We restrict the reported earthquake depths to 75 km or less to avoid the potential interference from depths phases (e.g., *sSS*), while the selected distance range minimizes the interference from top-side reflections (i.e., *Sdiff* postcursors) and *ScSScS* precursors (Schmerr & Garnero 2006, Deuss 2009, Zheng et al. 2015). After removing the instrument responses, all transverse component seismograms are filtered between corner periods at 5 s and 50 s using a Butterworth bandpass filter. The waveforms of *SS* precursors are typically filtered at longer periods (e.g., above 15 s period), but shorter period filters can be effective at reducing the Fresnel zone size and increasing the resolution of mantle reflectivity when dense data coverage is available (Schmerr & Garnero 2006). The filtered seismograms are subjected to a signal-to-noise ratio (SNR, defined as the ratio between the maximum amplitude of *SS* and that of noise in a precursory window; Gu et al. (2012)) criterion and only the traces with SNR greater than 3.0 are retained for the subsequent analysis. The final data-set consists of 1007 high quality, transverse-component waveforms from 322 events (Figure 4.2b).

4.2.2 Time-domain Stacking Method

Due to the path similarity between the *SS* and its precursors (Schultz & Gu 2013), the depths of reflectors can be effectively estimated from the differential times between the surface and mantle reflections. We deconvolve the *SS* waveforms, which share similar source effects with precursors, from the transverse-component seismograms to equalize the source (Shearer et al. 1999, Schultz & Gu 2013). The resulting waveforms are then time shifted to account for variations in crustal thickness, surface topography (CRUST2.0; Bassin (2000)) and mantle heterogeneity (S20RTS; Ritsema et al. (1999)) along the ray paths. To correct for move out, we employ the Local Stretch Zeroing (LSZ) method introduced by Kazemi & Siahkoohi (2012). This method eliminates stretching by dividing data into few time gates confined to the theoretical curves attributed to the reflection events (i.e., the mantle discontinuities). The effectiveness of the LSZ approach in move-out correction of *SS* precursors is investigated for synthetic waveforms calculated using PREM (Dziewonski & Anderson 1981). Figure 4.3 shows the results of the LSZ method where the theoretical curves are calculated using the PREM-predicted arrival times of *SdS* (where d represents a discontinuity depth) and a reference source-receiver distance of 130°. This approach considers the differential move-outs among the precursory arrivals while avoiding distortions of pulse shapes (see Figures 4.3c and 4.3d).

4.2.3 Depth Migration

Migration is a key step in seismic data imaging, which spatially relocates the recorded signals to their true positions to improve the image quality and accuracy (Gazdag & Sguazzero 1984, Sheriff & Geldart 1995, Gray et al. 2001). The migration process is particularly effective in studies of tectonically complex regions (e.g., subduction zones and hotspots), where diffraction and scattering caused by small-scale variations in discontinuity depth can adversely affect the imaging resolution (Neele et al. 1997, Braña & Helffrich 2004, Frederiksen & Revenaugh 2004, Thomas et al. 2004, Rost & Thomas 2009, Schultz & Gu 2013, Lessing et al. 2015). Several depth migration algorithms have been utilized in exploration or global seismic applications, which include Kirchhoff (Schneider 1978, Etgen et al. 2009), reverse time (Baysal et al. 1983, Chang & McMechan 1994, Biondi et al. 2002), and wave-equation (Gazdag 1978, Claerbout & Doherty 1972, Kühl & Sacchi 2003) migrations. In this study we adopt the Kirchhoff method for its simplicity and low computational cost. Pre-stack (rather than post-stack) is utilized to preserve the finer details contained in the *SS* precursor waveforms. Our algorithm searches for the energy arriving before *SS*, which is inundated by non-specular reflections and point-scatterers, and trace rays through 3D models of the crust and mantle shear velocities.

To evaluate the effectiveness and accuracy of Kirchhoff depth migration, we introduce an array of sources and receivers sampling the area indicated in Figure 4.4a. Synthetic seismograms are then calculated based on the global shear velocity model S20RTS (Ritsema et al. 1999), assuming the theoretical reflections occur at 220, 400 and 670 km depths below the center of the targeting area. We then adopt a grid of 32° by 32° with 2° lateral spacing (centered on 0° latitude and 115° longitude) and the depths range from 0 to 800 km at a constant increment of 2 km (see Figures 4.4a and 4.4b). Travel times of mantle reflections are subsequently calculated from each grid point (considered as a point-scatterer) to each source as well as to each seismic station by tracing rays three-dimensionally through the same velocity model. Finally, the interpolated amplitude on each seismogram is assigned to the corresponding gridpoint and stacked (Rost & Thomas 2009, Thomas & Billen 2009). In theory, the diffracted energy should stack constructively at the location of the true reflection point.

The migration results for a single source and receiver pair at 400 and 670 km depths (Figures 4.4c and 4.4d) suggest that the maximum stacked amplitude is distributed along a minimax-shaped isochron (Shearer 1993, Gu & Dziewonski 2002, Rost & Thomas 2009, Schmerr & Thomas 2011). In comparison with a single scenario, the Fresnel zone becomes more regular using an array of precursor waveforms since contributions from multiple raypaths collapse the stacked energy to the true reflection point (Figures 4.4e and 4.4f). Based on the data density, this array migration process can reduce the effective Fresnel zone size to 500-700 km laterally.

Figure 4.5 shows two vertical cross-sections through the center of the three-dimensional volume of migrated *SS* precursors. The minimax shape of the Fresnel zone is responsible for the concave up (see Figures 4.5a and 4.5c) and concave down (see Figures 4.5b and 4.5d) natures of the isochrons along and perpendicular to the great circle path, respectively (Shearer 1993, Neele et al. 1997, Gu et al. 1998). This result implies that the along- (off-) axis scattering would map a hypothetical reflector to a shallower (deeper) depth with the same arrival time (Shearer et al. 1999). By accounting for the contributions from the entire seismic array, the migration process reduces both the effective size of the Fresnel zone and the spreading of the migrated energy along the isochrons (Rost & Thomas 2009) (see Figures 4.5c and 4.5d).

4.3 Results

Based on our resolution test using an array migration process, the data are grouped into equal-sized spherical caps of 5° radius, according to the theoretical reflection points of *SS*, to ensure sufficient resolution and sampling density (Figure 4.6). Circular caps are sorted along 14 parallel profiles (with 2° cross-line spacing) approximately perpendicular to the Java trench (see Figure 4.6). The grid, which consists of 490 imaging points, provides an average nominal lateral resolution of 500 km in the study region. The data coverage is particularly dense in the northwestern and southwestern ends of the study region, where a significant number of caps contain more than 100 reflections. We examine the precursor waveforms in both time and depth domains to provide a cross-check on the accuracy of the recovered depth anomalies.

4.3.1 *SS* precursor Amplitude

Unlike conventional Kirchhoff migration approaches (Hanitzsch 1997), our algorithm weights each seismogram equally to avoid complexity. Hence, the amplitude information is extracted from the time-corrected waveforms. After applying crustal and mantle heterogeneity corrections, we stack the waveforms using the LSZ move-out technique based on the differential times between the *SS*, *S220S*, *S410S* and *S660S* phases (PREM; Dziewonski & Anderson (1981)) relative to a reference source-receiver distance of 130°. The amplitudes of *S410S* and *S660S*, extracted from the maxima within a 30 s window centered on the predicted times (PREM; Dziewonski & Anderson (1981)), reveal large-scale reflectivity structures at the MTZ discontinuities beneath SE Asia (Figure 4.7a and 4.7b). A NW-SE trending low-amplitude zone is observed near the 410 (see Figure 4.7a) along the Java trench, roughly parallel to the strike of the northward dipping Wadati-Benioff zone of deep-focus earthquakes (see Figure 4.6); the minimum amplitude of *S410S* reaches ~0.02% of that of *SS* beneath Western Java and the Timor trough. The measured reflectivity at the top of the MTZ does not vary significantly beneath Borneo and northern Sundaland, showing similar values to the regional average of 0.053%. On the other hand, a strong *S410S* is observed east of the Philippine trench, below which the maximum amplitude is nearly twice the regional average.

The reflection amplitude of *S660S* shows markedly increased amplitudes along the Java trench relative to its regional average of 0.048% (see Figure 4.7b). East of Sumbawa, enhanced reflections continue northward and reach their maximum at approximately 0.1% beneath the Banda Sea. Similar to *S410S*, *S660S* exhibits low to moderate reflection amplitudes beneath the Borneo and Sunda plates (see Figure 4.7b).

Inherent noise and limited data coverage could cause significant uncertainties in the amplitude measurements. To assess the amplitude robustness and reliability, we introduce a bootstrap resampling procedure (Efron & Tibshirani 1991, Deuss 2009, Dokht et al. 2016) to estimate the standard errors by repeating the measurements using 200 randomly selected subsets of the data traces (Figures 4.7c and 4.7d). Based on the distribution of bootstrap measurements, we conclude that the major amplitude anomalies lie within the 95% confidence level and the estimated errors do not exceed 0.021% and 0.025% for *S410S* and *S660S*, respectively.

4.3.2 *SS* precursor Travel Time

Using the same stacked seismograms, we are able to determine the arrival times of *SS* precursors accurately (Figure 4.8). The *S410S* times (see Figure 4.8a) indicate early arrivals with respect to *SS* in the vicinity of the Wadati-Benioff zone beneath western Java and the entire Banda Sea, ~8-10 s earlier than the regional average of -156.4 s. Most notably, the *S660S* times in the eastern part of the study area are 8-15 s shorter than the regional average of -229.25 s, extending from the Indian ocean side of the Flores island northward toward the Molucca Sea. Both *S410S* and *S660S* are, however, delayed beneath Borneo and the western Sulawesi regions (see Figures 4.8a and 4.8b).

To assess the effect of time corrections, which can introduce unwanted variations in both the amplitude and timing of the secondary reflections, we repeated the time-domain stacking procedure using a different shear velocity model (TX2007, Simmons et al. (2007)) and found no apparent changes in reflectivity. In other words, a reasonably accurate model of the mantle structure should produce reliable reflections from the major discontinuities.

4.3.3 MTZ Discontinuity Depth

The topography of MTZ discontinuities can be constructed from the depth-migrated volume of the *SS* precursor data-set (Figure 4.9). For reliable results we independently migrate the precursor waveforms using *S*-wave models of TX2007 (Simmons et al. (2007), Figures 4.9a and 4.9b) and S20RTS (Ritsema et al. (1999), Figures 4.9c and 4.9d). The results based on these two different velocity models are generally consistent, despite slightly deeper (1.2-3 km) discontinuity depths form TX2007 (see Figure 4.9). The calculated regional averages for the 410 and 660 are 403 km and 662 km, respectively, comparable to their respective global averages of 410-420 km and 650-660 km (Flanagan & Shearer 1998, Gu et al. 2003). The 410 is elevated beneath Eastern Sumatra-Western Java, the Flores and Banda Seas by up to 29, 35 and 37 km (see Figures 4.9a and 4.9c), respectively. In Eastern Sumatra and Western Java, the topography of the 410 is strongly anti-correlated with that of the 660, which is depressed by 20-40 km with respect to its regional mean (see Figures 4.9b and 4.9d). On the other hand, the depth of the 410 beneath the Banda Sea and Flores island positively correlates with that of the 660, showing 40-45 km elevation in this area. Both discontinuities are depressed beneath Borneo, western Sulawesi and the Celebes Sea, although the undulations on the 410 (+5 to +10 km) are significantly less than those on the 660 (+10 to +35 km).

Our measured MTZ discontinuity depths are generally consistent with those of Saita et al. (2002) from receiver function migration and Gu et al. (2003) based on joint inversion of the MTZ velocity and discontinuity topography (Figure 4.10). Despite differences in absolute depths, all three studies clearly identify elevated 410 and 660 beneath the eastern part of the study area. The lone exceptions are Sumatra and Java, where the underlying 410 is elevated by up to 50 km in the two regional studies, but appears to be average in the former global analysis (Gu et al. 2003) (see Figures 4.9 and 4.10). We attribute this discrepancy to the different data densities and lateral resolutions.

The transition zone thickness beneath eastern Sumatra and western Java exceeds the global average of 241-242 km (Flanagan & Shearer 1998, Gu et al. 1998, Lawrence & Shearer 2006*a*) by as much as 60 km (Figures 4.11a and 4.11b). These observations are comparable to the earlier reported values by Saita et al. (2002) and Gu et al. (2003), although the increase in MTZ thickness is less significant in the later study (approximately 15 km thicker than the global average, Figure 4.11c). The MTZ beneath the Banda Sea shows only minor thickness variations, but becomes 20-30 km narrower toward the north (the Molucca Sea) and south (the Australian side of the Timor trough) due to substantial elevations of the 660 (see Figures and 4.9 and 4.11). The most noteworthy difference among these studies is the MTZ beneath northern Borneo and western Sulawesi, where the present study shows a thick MTZ (270-275 km), while it was found to be narrower (approximately 200 km) in the earlier study by Saita et al. (2002) (see Figure 4.11).

4.4 Discussion

The mantle structure beneath SE Asia has been previously investigated using body wave travel time (Fukao et al. 1992, Widiyantoro & van der Hilst 1997, Gorbatov & Kennett 2003, Fukao & Obayashi 2013) and waveform (Fichtner et al. 2010, Lekić & Romanowicz 2011) tomography. The most prominent feature in the upper mantle in this region is a narrow, northward dipping high velocity structure, which extends from the Sunda arc (in the west) to the Banda arc (in the east) (Figures 4.12a and 4.12b) and has been commonly attributed to the subducted Indo-Australian oceanic lithosphere underneath the Eurasian plate. Both P and S-wave data generally suggest a 1-2% increase in the seismic velocities within the MTZ beneath Sumatra, Java, the Flores and Banda Seas (Widiyantoro & van der Hilst 1996, Replumaz et al. 2004, Amaru 2007) along the Wadati-Benioff zone of the descending slab (Hamilton 1974, Cardwell & Isacks 1978, Hayes et al. 2012). The detailed morphology of subducting slab exhibits major lateral variations and different penetration depths along its strike (Hall & Spakman 2015), which can locally affect the topographies of MTZ discontinuities.

Despite extensive global studies of P and S-waves (Flanagan & Shearer 1998, Gu et al. 2003, Lawrence & Shearer 2006*a*, Andrews & Deuss 2008, Deuss 2009), variations in MTZ discontinuity depths beneath the SE Asia subduction zones have been thinly explored on the regional scale (Saita et al. 2002). In comparison with earlier analyses based on SS precursors (Gu et al. 2003, Houser et al. 2008, Lawrence & Shearer 2008, Deuss 2009), the current study takes advantage of vastly improved data coverage (due to a longer period of recordings) and enhanced resolution by considering scattering from the finer-scale depth perturbations of the discontinuities (Rost & Thomas 2009). The resulting migrated *SS* precursor waveforms provide new constraints on the MTZ structure and the dynamical process therein that are associated with the subducting lithospheric plates beneath SE Asia.

4.4.1 Java Subduction and Slab Gap

Our study reveals significant lateral variations in MTZ discontinuity depth and thickness along the Sunda arc (see Figures 4.9 and 4.11). The thickest part of the MTZ is observed under southwestern Sumatra and eastern Java (approximately 300 km on average), magnified by the contrasting topography of the 410 and 660 in response to the temperature effect of a sinking slab within the MTZ. According to a recent analysis by Fukao & Obayashi (2013), the *P*-wave velocities increase by 1.5% under the southeastern part of the Sunda arc (Figures 4.13a and 4.13b). This anomaly appears to extend into the MTZ at a steep angle, eventually terminating at approximately 1500 km depth in the shallow lower mantle (Puspito & Shimazaki 1995, Widiyantoro & van der Hilst 1997). Assuming an isochemical model, a 20 km topographic variation on the 410 or 660 would require a temperature reduction of ∼250 K within the slab (Akaogi et al. 1989, Weidner & Wang 1998, Saita et al. 2002). Our measurements in western Java are consistent with these earlier findings. However, the depth of the 410 km discontinuity gradually increases toward the east and becomes nearly flat (with less than 5 km elevation compared to its regional average) beneath eastern Java (see Figures 4.13c and 4.13d), where average to weakly positive velocities have been previously documented at 300-500 km depths (Widiyantoro & van der Hilst 1996, 1997, Amaru 2007, Fukao & Obayashi 2013, Huang et al. 2015) (see Figure 4.13b). The apparent absence of the subducting slab in the vicinity of the 410 beneath Eastern Java coincides with a pronounced seismically quiescent zone along the trench at comparable depths (Puspito & Shimazaki 1995, Widiyantoro & van der Hilst 1996). This observation has led to the hypothesis of a "gap" or "tear" at the top of the mantle MTZ (Hall & Spakman 2015).

Different processes have been proposed as possible mechanisms for developing a tear in the slab, which potentially involve 1) local heterogeneity within the subducting lithospheric plate (Hall & Spakman 2015) and 2) necking and thining of the slab in the upper mantle (Widiyantoro & van der Hilst 1996). Hall & Spakman (2015) suggest that a hole has been formed in the sinking slab after a buoyant oceanic plateau reached the Java trench at approximately 8 Ma, which was unable to subduct due to a lower density than the ambient lithosphere (Niu 2014). In this scenario, the oceanic plateau collision blocks subduction and causes the trench to step backward relative to the incoming plate. Over time, the subduction of the oceanic lithosphere will resume behind the plateau and generate a vertical tear (hole) in the downgoing slab (Hall et al. 2009, Widiyantoro et al. 2011*b*). This hypothesis is supported by the discovery of potassium-rich magmatism, which has been linked to reduced fluid flux from the slab into the mantle wedge after the slab window passed beneath the arc in Eastern Java (Edwards et al. 1994, Hall & Spakman 2015). It is worth noting that smaller-sized gaps and tears have also been reported further east in the subducting slab beneath the Timor and Flores islands (Widiyantoro et al. 2011*b*, Hall & Spakman 2015); these features remain below the detection threshold of *SS* precursors from this study.

4.4.2 MTZ Beneath the Banda Trench

The most notable depth anomalies are observed beneath the Banda Sea and its surrounding areas, where a narrow MTZ is detected (see Figure 4.11) due to a substantially elevated 660 (by nearly 40 km; Figure 4.9). An uplifted 410 likely results from the Miocene subduction of the Jurassic oceanic lithosphere at the Banda trench (Spakman & Hall 2010, Fichtner et al. 2010), which deflects and becomes stagnant atop the MTZ (Widiyantoro et al. 2011*a*). The complex geometry of the slab is supported by a spoon-shaped high velocity zone in the asthenosphere beneath the Banda Sea and western Sulawesi (Amaru 2007, Lekić & Romanowicz 2011, Widiyantoro et al. 2011*b*, Fukao & Obayashi 2013) (see Figure 4.12). While the MTZ phase boundaries (i.e., the 410 and 660) are expected to be anti-correlated, especially in the vicinity of the subduction zones (Gossler & Kind 1996, Gu et al. 2003, Li & Yuan 2003), the excess elevation of the 660 in this region requires the consideration of non-vertical dip of the subducting slab (Gu et al. 2012, Dokht et al. 2016). A vertical section of the migrated reflectivity along the west-east direction shows the negative correlation between the 410 and 660 depths along the Wadati-Benioff zone (Figure 4.14a), where the 660 reaches the maximum depth of 682 km directly beneath Southeast Sulawesi (Figure 4.14b). The observed 20 km depression of the 660 is consistent with the response of the post-spinel phase transition from ringwoodite to perovskite and magnesiowustite with a negative Clapeyron slope of approximately -2.8 to -3.0 MPa/K (Ito & Takahashi 1989, Weidner & Wang 1998) to a temperature decrease of 150-200 K in the bottoming part of the slab (see Figure 4.14b).

Beneath the Banda Sea in eastern Indonesia, an elevated 660 is accompanied by the high amplitude *S660S* arrivals in the time domain stacks of precursor waveforms (see Figure 4.7b). These observations consistently suggest an increase in impedance contrast across a relatively shallow 660 due to the presence of a high temperature anomaly at the base of MTZ. A 40 km elevation of the 660 requires a temperature increase of 250-300 K (Ito & Takahashi 1989), assuming that the compositional effects can be neglected compared to thermal effects in the upper mantle (Piazzoni et al. 2007). This will result in a shear wave velocity reduction of approximately 2% (Stixrude & Lithgow-Bertelloni 2005, Houser & Williams 2010), which has been rarely documented by seismic tomography at depths greater than 600 km (Amaru 2007, Fukao & Obayashi 2013) (see Figure 4.12), partly due to limited vertical resolutions and different dependencies of P and S-wave velocities on temperature. The presence of this thermal anomaly may be associated with sub-slab mantle flow (Di Leo et al. 2012, Lynner & Long 2014) parallel to the trench at transition zone depths, which may have been induced by trench migration and exhibits a higher temperature than the ambient mantle (Long & Silver 2008) (Figure 4.15). Plate tectonic reconstruction of SE Asia provides further supports for the rapid eastward trench rollback of the Jurassic slab into the oceanic embayment within the Australian plate (Spakman & Hall 2010). Alternately, the presence of a sub-slab low velocity anomaly above the 660 due to the deep dehydration process of the old oceanic slab (similar to that of suggested by Zhao & Ohtani (2009) beneath the Pacific slab), together with a temperature increase of >200 K, can explain the enhanced *S660S* amplitudes at a depth close to 620 km (see Figure 4.15).

4.5 Conclusions

This study examines the depth and amplitude of the MTZ seismic discontinuities near the Sunda-Banda arc using *SS* precursors. Through migration imaging, we observe small-scale depth variations on the 410 and 660 across the SE Asia subduction zones. Beneath eastern Sumatra and western Java, a strong negative correlation between the 410 (elevated) and 660 (depressed) depths suggests significantly reduced temperature within the steeply dipping Indo-Australian slab. A flat 410 beneath eastern Java coincides with the absence of deep-focus earthquakes over the depth interval from 300 km to 500 km. These observations may be associated with the arrival of a buoyant plateau in the trench in the Late Miocene, which formed a vertical tear in the subducting slab.

Beneath the Banda Sea, the enhanced amplitude of the 660 and a 40 km elevation are evidence of low seismic velocities within the MTZ due to an increase in its temperature. The low velocity anomaly above the 660 can be associated with 1) trench-parallel mantle flow beneath the slab driven by the trench migration and 2) deep dehydration of the oceanic lithosphere. The results presented in this study provide a more detailed image of the mantle reflectivity structure beneath SE Asia, which cab be strongly affected by the dynamics of the subducting slab.

In short, improving the resolution of mantle imaging can provide critical insights into the complex morphology, temperature and dynamic process beneath the Java-Banda Sea region.

The research presented in this Chapter is original to this thesis and will be published at a later date.

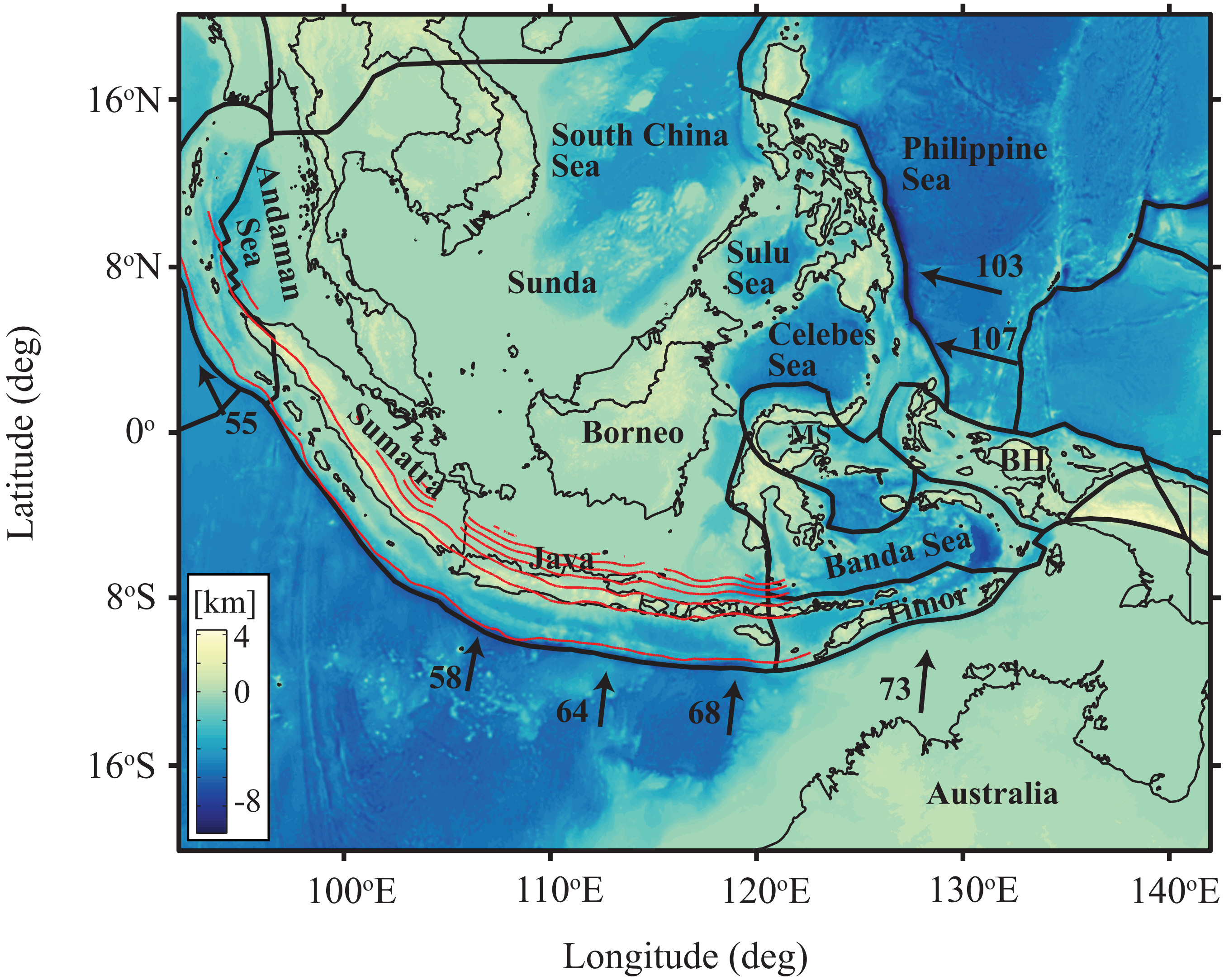

Figure 4.1: A topographic map of the study area. The thick black lines indicate the major plate boundaries after Bird (2003). The black arrows shows the direction of plate motion with respective to the Sunda block and their relative convergence rates are measured in cm/year. The red lines denote the slab contours taken at a constant interval of 100 km (Hayes et al. 2012). Abbreviations: MS, Molucca Sea; BH, Birds Head.

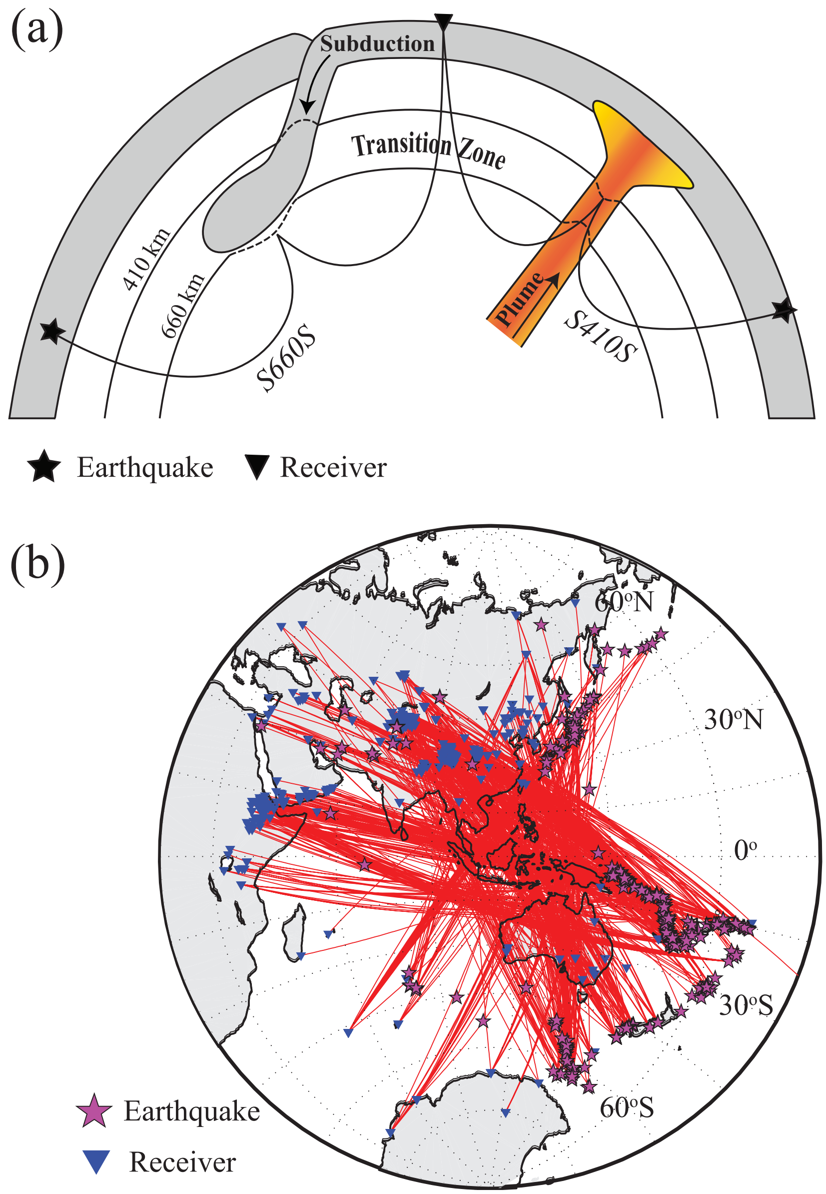

Figure 4.2: (a) The schematic diagram illustrates the *SS* precursor raypaths and the expected perturbations on the discontinuity depths in the presence of a cold subducting slab and a hot mantle plume in an isochemical mantle. (b) Distribution of the earthquake (stars) and seismic station (inverted triangles) locations used in this study. The lines segments indicate the geometrical paths of *SS* precursors.

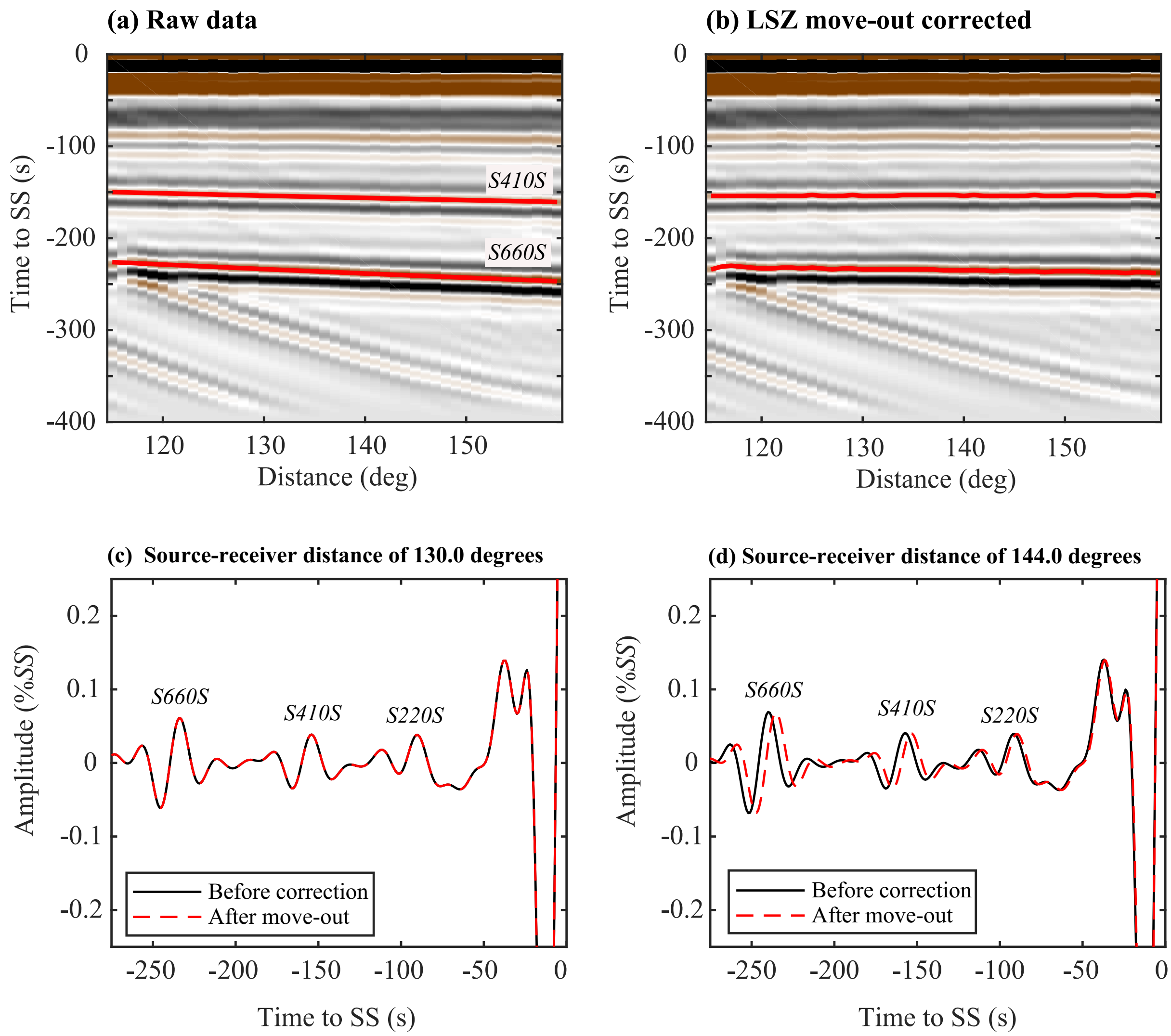

Figure 4.3: A synthetic test to demonstrate the effectiveness of the LSZ method for move-out correction. (a) A synthetic record section of *SS* precursors calculated based on PREM (Dziewonski & Anderson 1981) before move-out correction. (b) Move-out corrected data using the LSZ method. The thick red lines indicate the S410S and S660S precursors. (c) and (d) A comparison between the precursor waveforms before (solid black lines) and after (dashed red lines) move-out correction for epicentral distances of 130 and 140 degrees, respectively. The differential time shifts associated with the three major interfaces (i.e., the 220, 410 and 660) are accurately computed using the LSZ method.

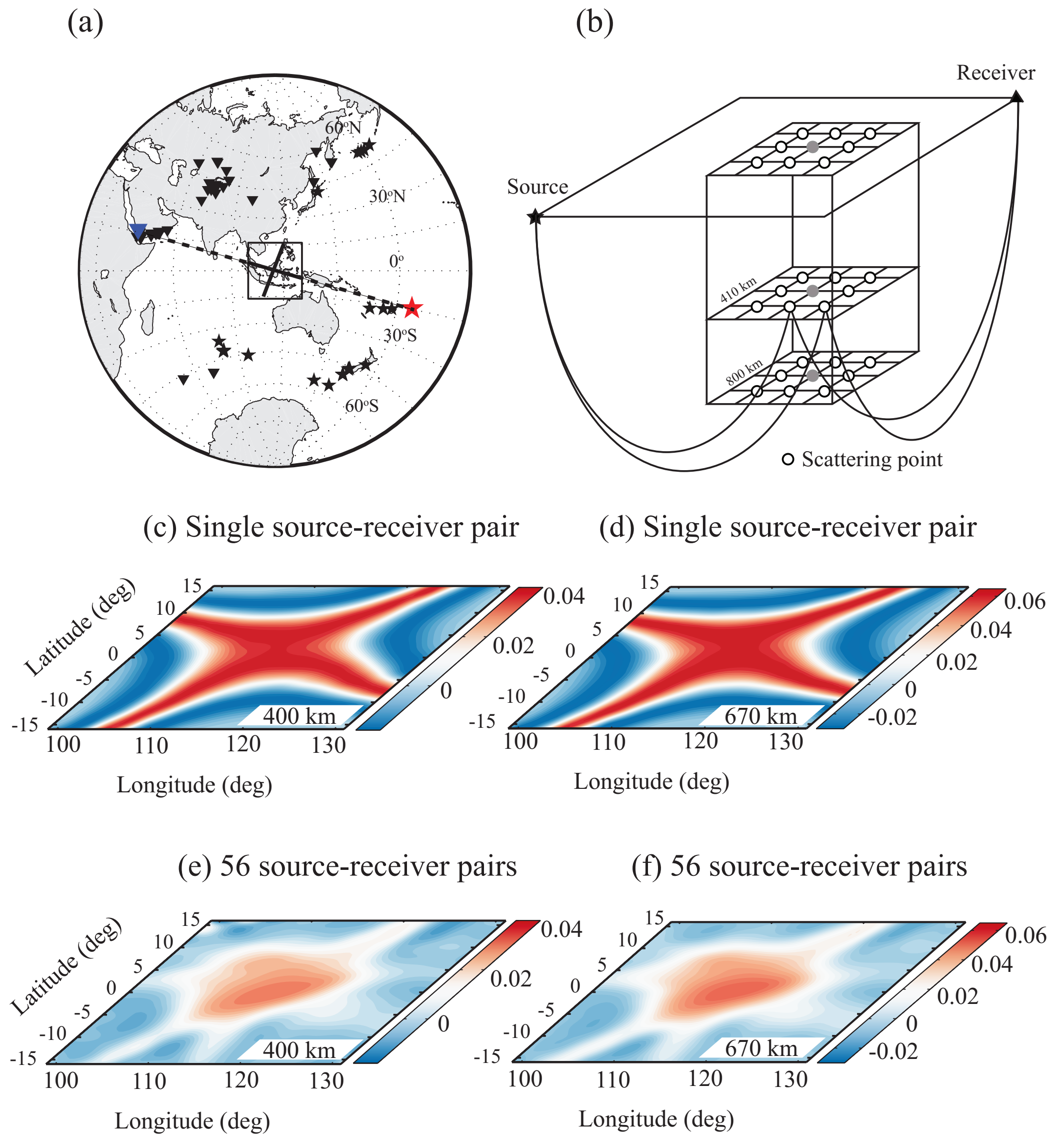

Figure 4.4: An array migration example showing the reflections at 400 and 670 km depths. (a) Distributions of the 56 source-receiver pairs that sample the area outlined by the black box. The stars and triangles represent the locations of the sources and receivers, respectively. (b) A schematic drawing of *SS* precursors reflected off the scattering points (open circles). The gray circles represent the reflection points half-way between the source and receiver. (c) and (d) Fresnel zones of *SS* reflections at the respective depths of 400 and 670 km for a given source-receiver pair (indicated by the red star and blue triangle in panel (a)). (e) and (f) Same as (c) and (d) but consider the contributions from all source-receiver pairs. The color bars indicate the stacked amplitude of the migrated energy.

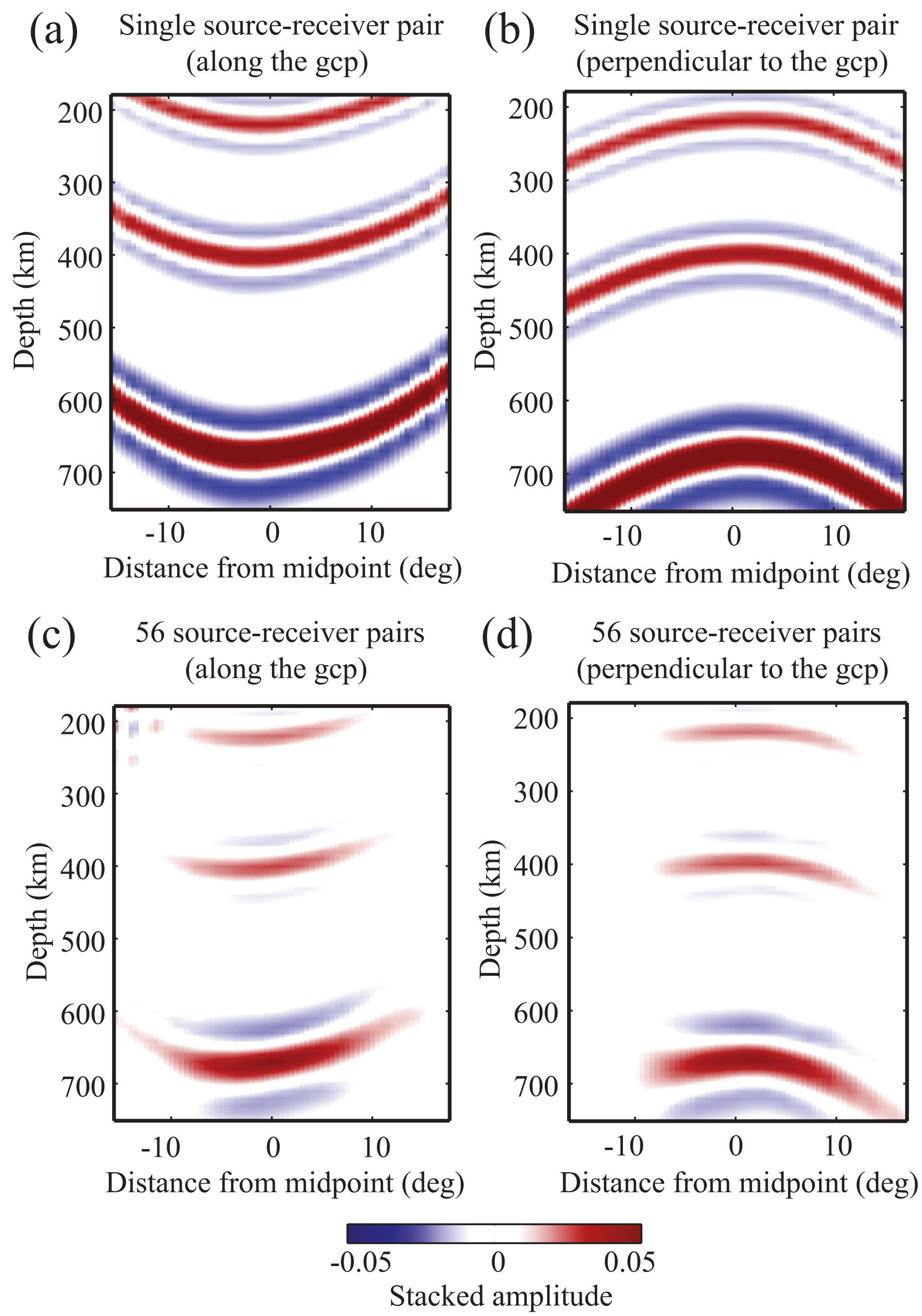

Figure 4.5: Array migration results using a single source-receiver pair (top panels) and 56 source-receiver pairs (bottom panels). (a) and (b) Vertical cross-sections along and perpendicular to, respectively, the great circle path connecting a given source-receiver pair indicated in Figure 4.4a. (c) and (d) Similar to (a) and (b) but for all source-receiver pairs. The color bar indicates the stacked amplitude of the migrated energy.

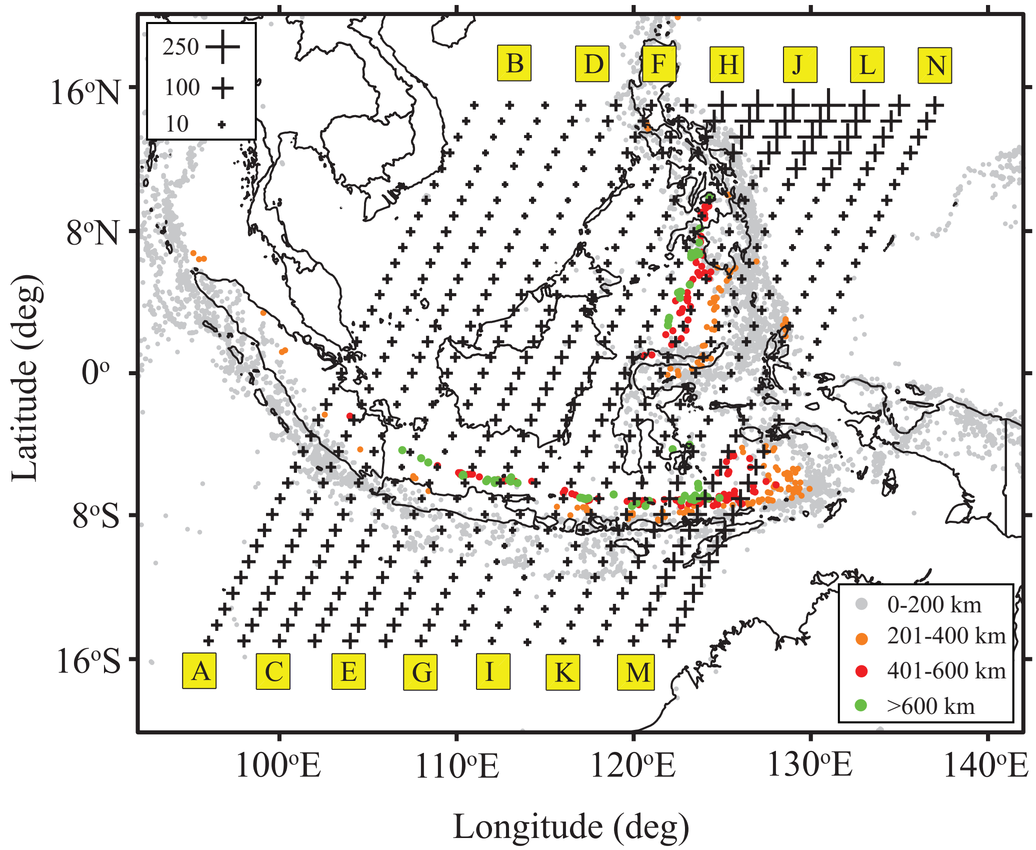

Figure 4.6: A map of the study area showing the locations of the imaging points (black crosses), which are sorted along 14 parallel profiles (A-N) oriented approximately perpendicular to the arc. The sizes of the crosses correspond to the total number of contributing traces to each point. The colored circles indicate the deep focal earthquakes that are grouped into the four different depth intervals (0-200 km: gray circles; 201-400 km: orange circles; 401-600 km: red circles; >600 km: green circles).

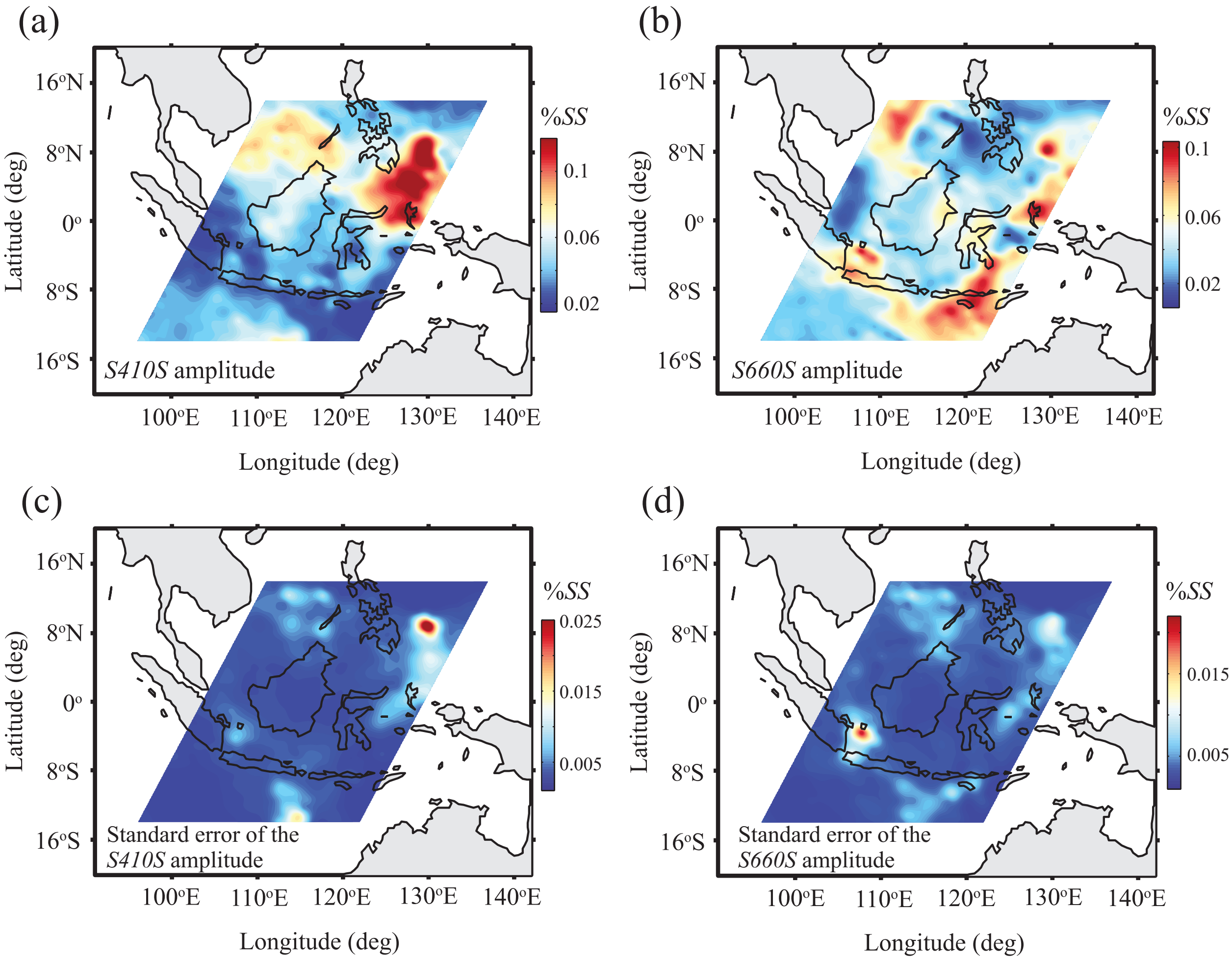

Figure 4.7: Interpolated reflection amplitudes of the (a) *S410S* and (b) *S660S*. The precursor amplitudes are normalized to that of *SS*. (c) and (d) The standard errors of the reflection amplitudes based on a bootstrapping analysis. The red and blue colors indicate the high and low amplitude precursory arrivals, respectively.

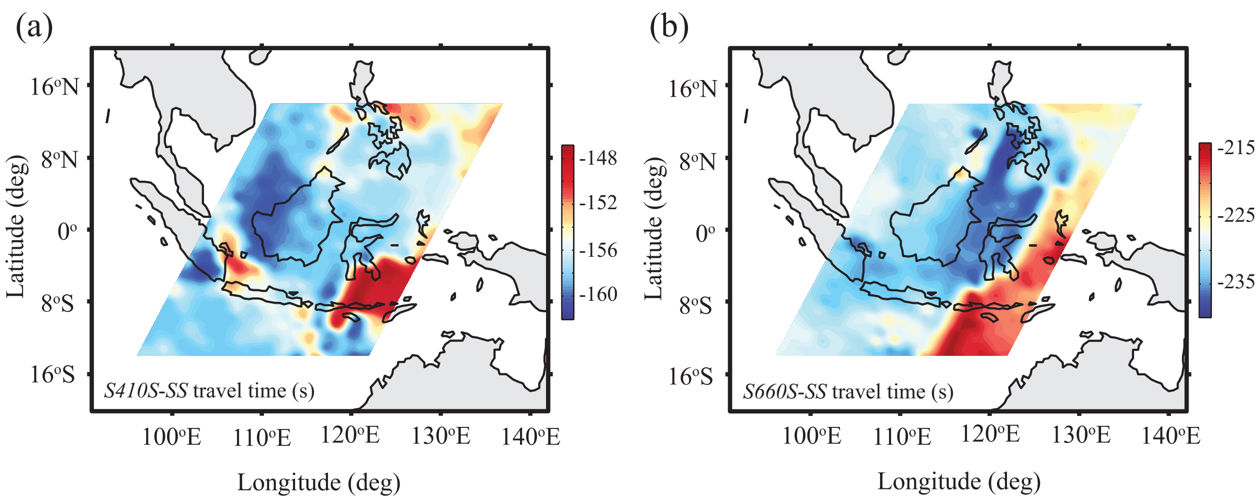

Figure 4.8: Interpolated differential times of (a) *S410S-SS* and (b) *S660S-SS*. The red and blue colors represent early and delayed *SS* precursor arrivals, respectively.

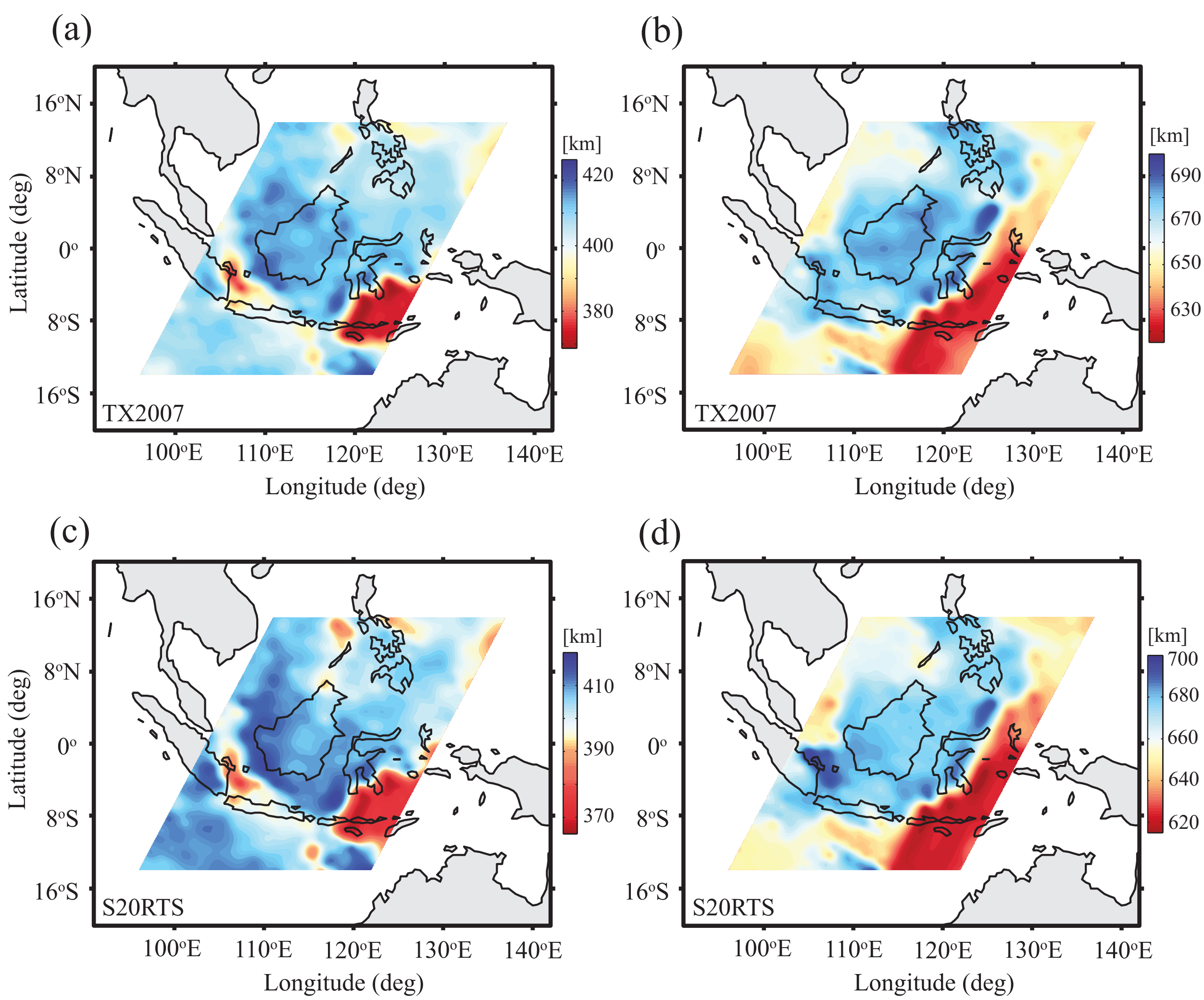

Figure 4.9: (a) and (b) Topography of the 410 and 660, respectively, calculated from the depth migration of SS precursors using the S-wave model of TX2007 (Simmons et al. 2007). (c) and (d) Similar to panels (a) and (b), but using the S-wave model S20RTS (Ritsema et al. 1999). The red and blue colors indicate elevation and depression, respectively.

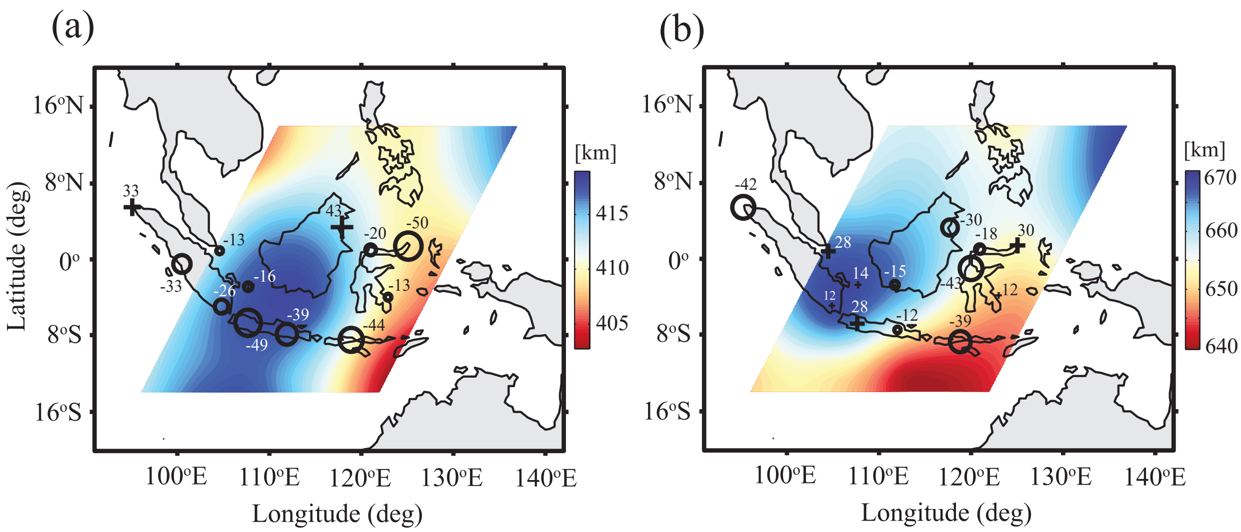

Figure 4.10: Discontinuity Topography. The color contours show the (a) 410 and (b) 660 topography from Gu et al. (2003). The red and blue colors show the discontinuity elevation and depression, respectively. The open circles and crosses denote the elevation and depression, respectively, of the MTZ discontinuities from Saita et al. (2002). The depth anomalies from Saita et al. (2002) are plotted relative to the corresponding global averages of 418 km and 660 km for the 410 and 660 (Flanagan & Shearer 1998).

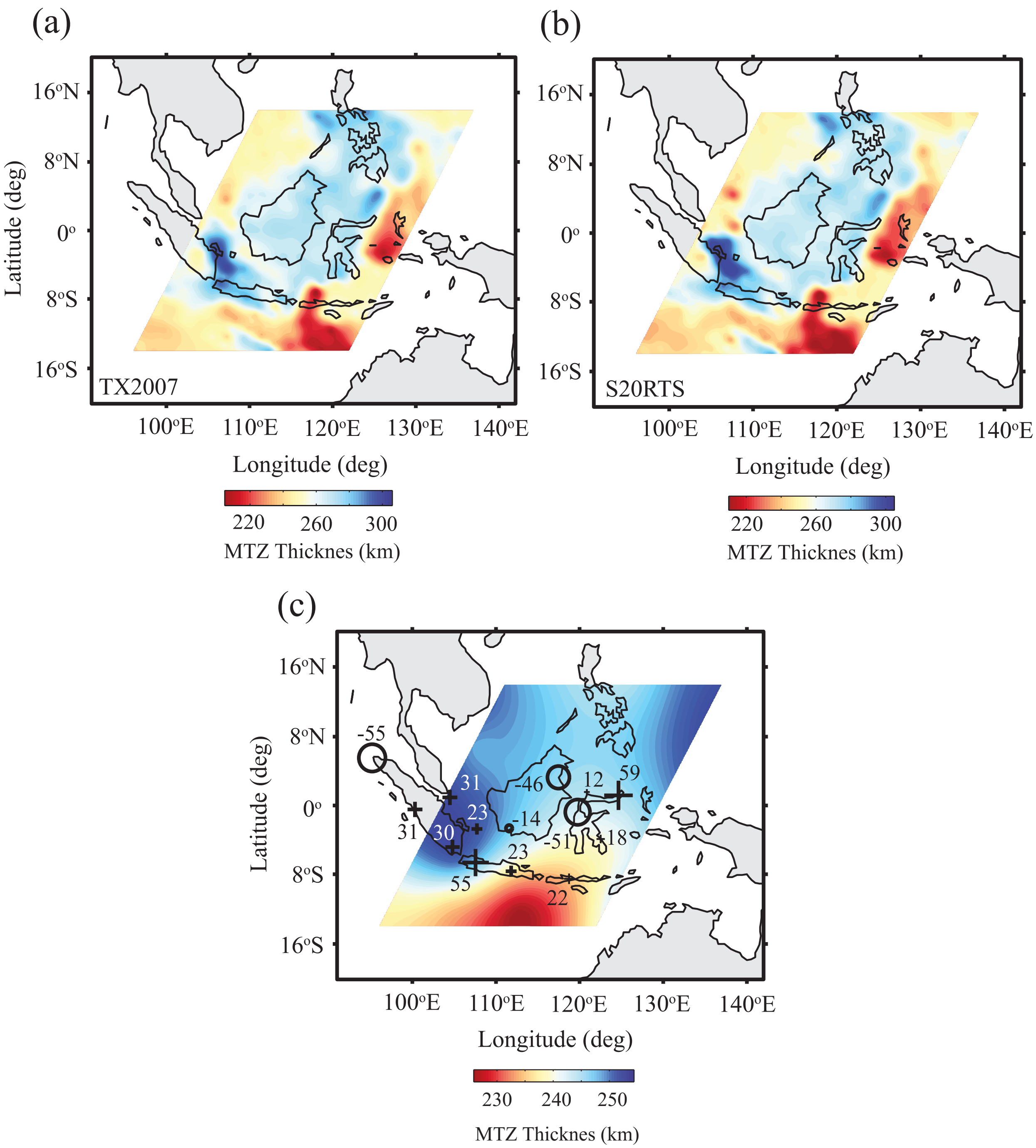

Figure 4.11: (a) MTZ thickness variations calculated from the migrated depths of the 410 and 660 km discontinuities using TX2007 (Simmons et al. 2007). (b) Similar to (a) but using S20RTS (Ritsema et al. 1999). (c) The color contours represent the MTZ thickness measurements from Gu et al. (2003). The open circles and crosses show thinner and thicker transition zone regions, respectively, from Saita et al. (2002) relative to the global average of 241 km (Flanagan & Shearer 1998).

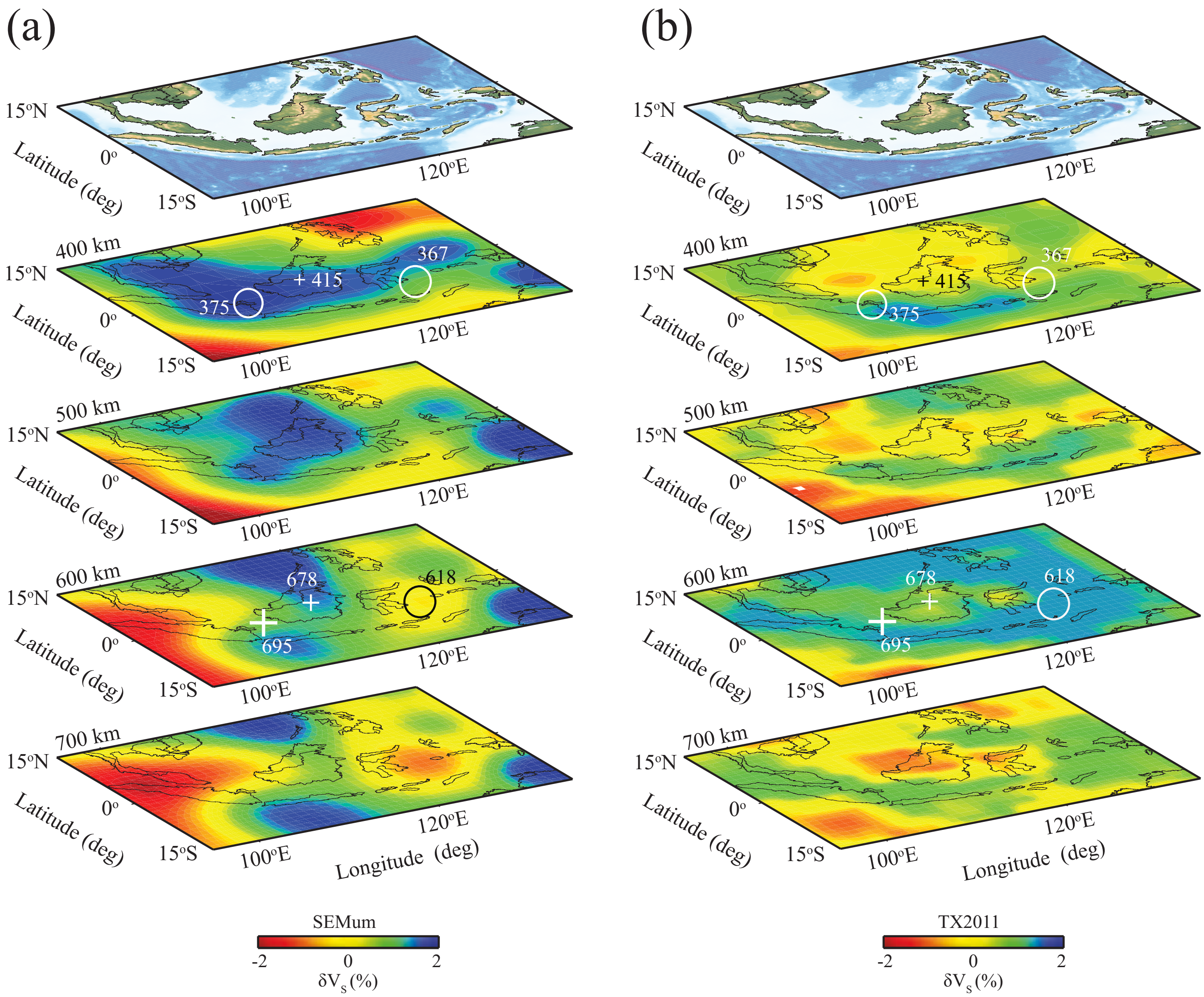

Figure 4.12: *S*-wave velocity perturbations from (a) SEMum (Lekić & Romanowicz 2011) and (b) TX2011 (Grand 2002) at 400 km, 500 km, 600 km, and 700 km depths (IRIS, DMC 2013). The open circles and crosses indicate the major depth anomalies of the 410 and 660 from this study. The blue and red colors denote fast and slow seismic anomalies, respectively.

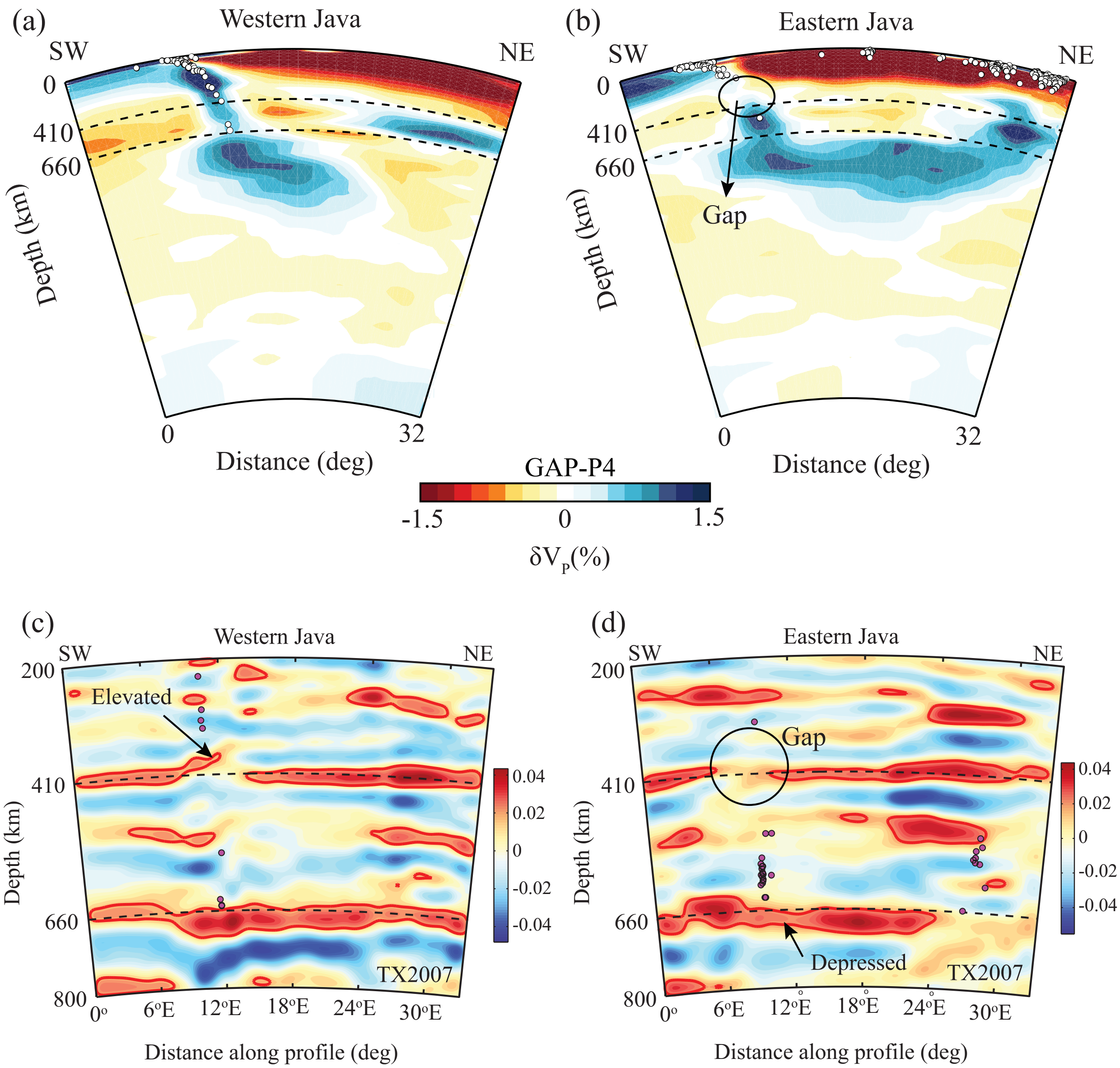

Figure 4.13: Vertical cross-sections of variations in P-wave velocities beneath (a) western (along profile D of Figure 4.6) and (b) eastern (along profile H of Figure 4.6) Java from Fukao & Obayashi (2013). (c) Reflectivity cross-sections of the migrated SS precursors beneath western Java using TX2007 (Simmons et al. 2007). (d) Similar to (c) but beneath eastern Java. The white (top panels) and magenta (bottom panels) circles indicate the locations of deep earthquakes.

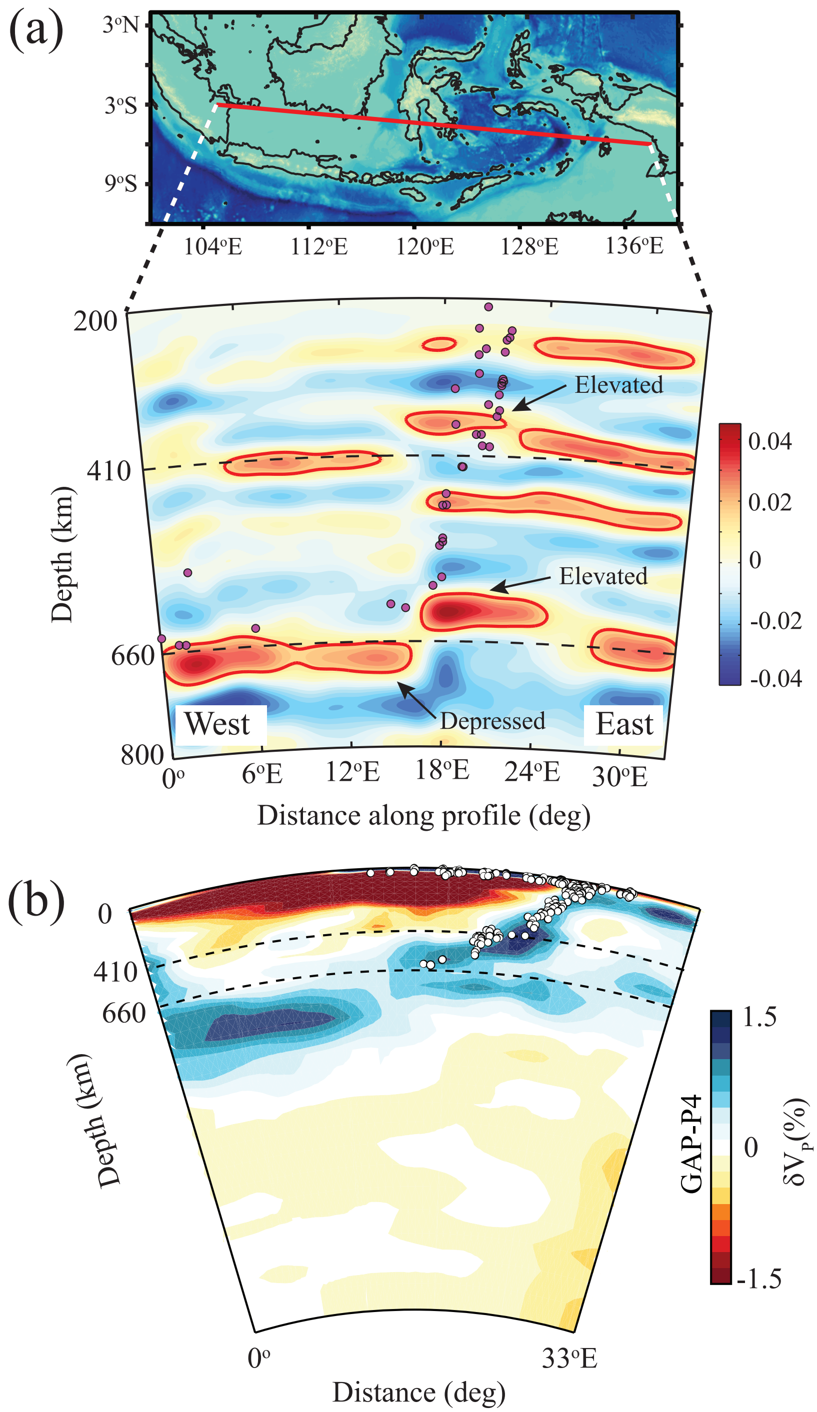

Figure 4.14: (a) A reflectivity cross-section of the migrated *SS* precursors along W-E direction using TX2007 (Simmons et al. 2007). The red and blue colors represent high and low reflection amplitudes, respectively. (b) A vertical cross-section *P*-wave velocity perturbations along the profile indicated in panel (a). The magenta (in panel a) and white (in panel b) circles indicate the locations of deep-focus earthquakes.

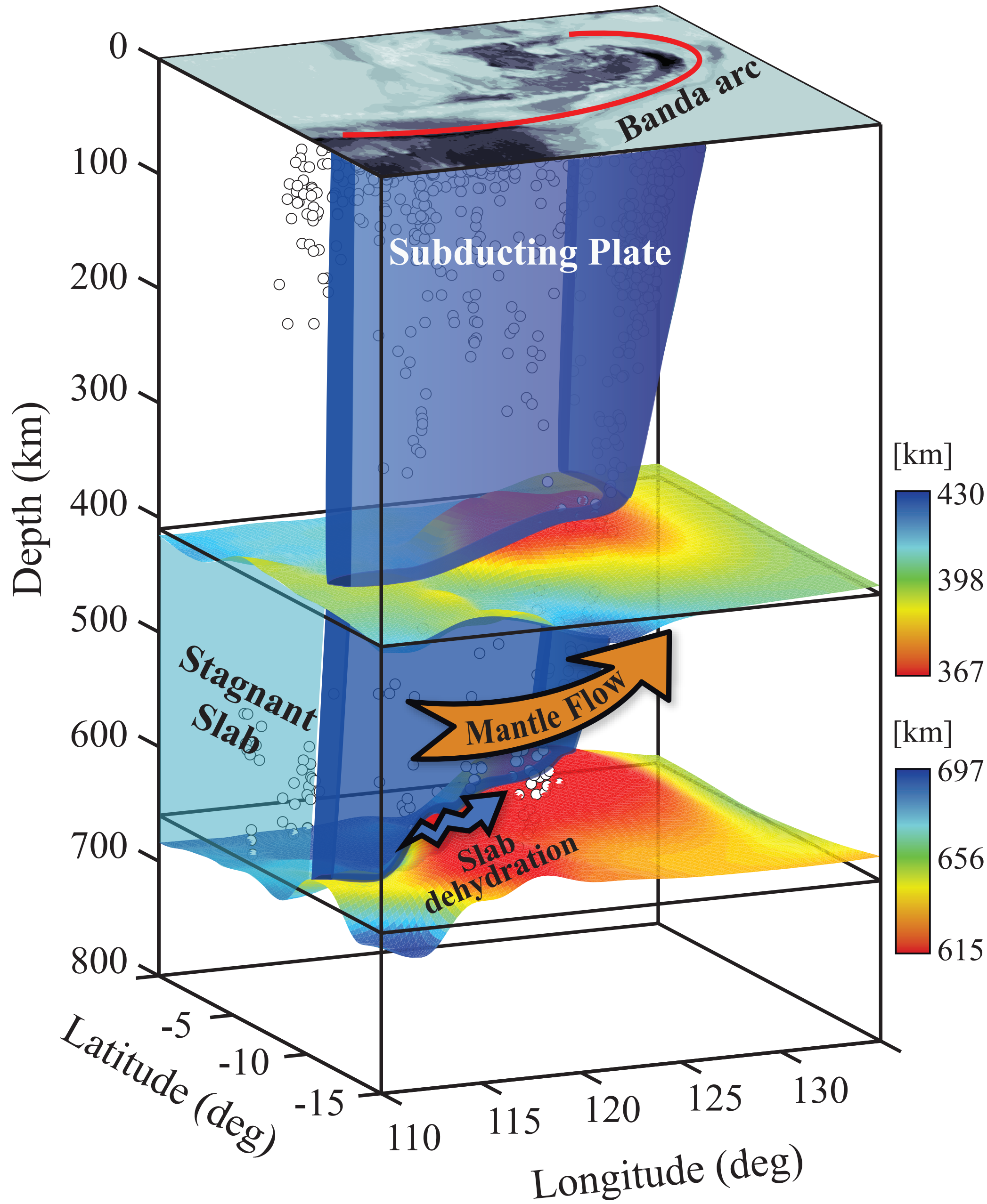

Figure 4.15: A schematic drawing of the subduction along the Banda arc. The presence of a low velocity zone within the MTZ beneath the slab can be explained by the 1) sub-slab mantle flow induced by trench migration, and 2) deep dehydration of the oceanic slab. The topography of the 410 and 660 beneath the Banda trench are color-coded and plotted at the respective depths. The white circles indicate the locations of deep-focus earthquakes.

Chapter 5

Summary, conclusion and future work

5.1 Summary

In this thesis we studied the characteristics of the MTZ discontinuities using the shear-wave underside reflections and P-to-S converted waves. In each chapter we utilized a different imaging technique to improve the resolution of the upper mantle reflectivity structure.

Careful analyses of both the arrival times and amplitudes of SS precursors from the seismic discontinuities are crucial for improving our understanding of mantle dynamics and composition. In Chapter 2, we introduced a nonlinear waveform inversions technique to simultaneously constrain shear velocities and discontinuity depths beneath the northwestern Pacific subduction system. Based exclusively on a large SS precursor waveform data-set, we are able to clearly delineate the morphology of the descending Pacific plate, which flattens at the base of the upper mantle and extends westward by at least 1500 km toward northeastern China. Our grid search over a range of angles indicates a maximum correlation between shear velocity and transition zone thickness at $\sim$30 degrees, consistent with the reported average slab dip beneath the study region. The strongly positive correlation suggests predominantly thermal, rather than compositional, variations along the descending Pacific plate. Our joint depth-velocity solutions also suggest a 5-10 km depression of the 410 km discontinuity and an average decrease of 1.2% in upper mantle shear velocity beneath the intraplate volcanic fields in northeastern China. This anomaly, which reaches the middle of the upper mantle transition zone beneath the Changbai hotspot, initiate at a significantly shallower ($\sim$320 km) depth beneath the Wudalianchi region. The high amplitude reflection at depths greater than 410 km suggests a water-poor melt layer in possible association with 1) decomposition melting from passive upwelling and/or 2) active upwelling through a slab window.

Key challenges in the analysis and interpretation using secondary seismic phases are incomplete data coverage, high noise levels and interfering seismic arrivals, especially near tectonically complex regions. In Chapter 3 we applied Singular Spectrum Analysis (SSA) to remove random noise, reconstruct missing data traces, and enhance the robustness of SS precursors and P-to-S converted waves (also knows as the receiver function) from mantle discontinuities. Our method takes advantage of the predictability of time series in the frequency-space domain and performs rank reduction using the singular value decomposition of the trajectory matrix. We applied SSA to synthetic record sections as well as observations of 1) SS precursors from NE China, and 2) receiver functions from southwestern Canada. In comparison with raw data, the SSA enhanced results show greater resolution attributable to the suppression of incoherent noise, which tends to reduce the signal amplitude during standard averaging procedure, through rank reduction. In the case of underside reflections, SSA enables an effective separation of the SS precursors and the postcursors S-wave core diffractions. This method will greatly benefit future analyses of weak crustal and mantle seismic phases, especially when data coverage is less than ideal.

A key motivation of this thesis research is to improve the image resolution, which can only be achieved through the combination of dense network data and effective resolution enhancement technique. Conventional array methods in the analysis of SS precursors stack the waveforms to obtain the average discontinuity depth throughout the staking area. Smearing due to large Fresnel zones (>1000 km) can degrade the fine-scale topography of the discontinuity. To provide a partial solution, we introduce a depth migration algorithm in Chapter 4 based on the common scattering point method while considering non-specular diffractions from the MTZ discontinuities. Beneath the Sunda arc, the depths of the 410 (elevated by nearly 30 km) and 660 (depressed by 20-40 km) are correlated with the morphology of the subducting

Indo-Asutralian slab. In western Java, a "flat" 410 coincides with a documented slab gap, showing length scales of >400 km laterally and >200 km vertically. This can be explained by the arrival of a buoyant oceanic plateau at the Java trench at approximately 8 Ma ago, which may have caused a temporary cessation of subduction and formed a tear in the subducting slab. Our results highlight the contrasting depths of the 410 and 660 along the shallow-dipping slab at the Banda trench. The 660, however, becomes significantly uplifted toward the east beneath the Banda Sea, which accompanied by significantly enhanced reflection amplitudes. These observations consistently suggest the existence of a sub-slab low velocity (high temperature) zone, possibly related to the deposition of old oceanic lithospheres.

5.2 Future work

We studied the detailed structure of the upper mantle discontinuities beneath the NW Pacific subduction zones (Chapter 2) and SE Asia (Chapter 4) using dense regional data-sets of *SS* precursors. Due to the rapidly growing number of seismic stations, the methods introduced in thisNo prob thesis can be successfully applied to other regions around the globe. Additionally, these imaging techniques could potentially be applied to other seismological observations, such as triplicated body waves (e.g., Song et al. 2004, Wang et al. 2006, Chen & Tseng 2007) and *ScS* reverberations (e.g., Revenaugh & Jordan 1991, Gaherty et al. 1996), which are sensitive to the velocity structure near the discontinuities and their depths.

We portrayed the application of the SSA filtering of 2-D time series to enhance the robustness of seismic arrivals from mantle discontinuities (see Chapter 3). To overcome the limitations of the SSA interpolation (especially in removing the regular gaps in the data), other data reconstruction techniques, such as anti-alias Cadzow filtering (Naghizadeh & Sacchi 2013), can be employed. A multichannel SSA approach can also be utilized for further improvement of the spatial and temporal resolution of mantle imaging (see Oropeza & Sacchi 2011).

Bibliography

Abma, R. & Claerbout, J. (1995), 'Lateral prediction for noise attenuation by tx and fx techniques', *Geophysics* **60**(6), 1887–1896.

Agee, C. B. (1998), 'Phase transformations and seismic structure in the upper mantle and transition zone', *Reviews in Mineralogy and Geochemistry* **37**(1), 165–203.

Ai, Y. & Zheng, T. (2003), 'The upper mantle discontinuity structure beneath eastern China', *Geophysical research letters* **30**(21).

Akaogi, M., Ito, E. & Navrotsky, A. (1989), 'Olivine-modified spinel–spinel transitions in the system Mg_2SiO_4–Fe_2SiO_4: calorimetric measurements, thermochemical calculation, and geophysical application', *Journal of Geophysical Research* **94**, 15671–15685.

Akaogi, M., Takayama, H., Kojitani, H., Kawaji, H. & Atake, T. (2007), 'Low-temperature heat capacities, entropies and enthalpies of Mg_2SiO_4 polymorphs, and α- β- γ and post-spinel phase relations at high pressure', *Physics and Chemistry of Minerals* **34**(3), 169–183.

Akaogi, M., Tanaka, A. & Ito, E. (2002), 'Garnet–ilmenite–perovskite transitions in the system $Mg_4Si_4O_{12}$–$Mg_3Al_2Si_3O_{12}$ at high pressures and high temperatures: phase equilibria, calorimetry and implications for mantle structure', *Physics of the Earth and Planetary Interiors* **132**(4), 303–324.

Amante, C. & Eakins, B. (2009), 'ETOPO1 1 Arc-Minute Global Relief Model: Procedures', *Data Sources and Analysis. NOAA Technical Memorandum NESDIS NGDC-24. National Geophysical Data Center, NOAA.* .

Amaru, M. (2007), Global travel time tomography with 3-D reference models, Geol. Traiectina, PhD thesis, PhD thesis, Utrecht Univ. 1–174.

Ammon, C. J., Randall, G. E. & Zandt, G. (1990), 'On the nonuniqueness of receiver function inversions', *Journal of Geophysical Research: Solid Earth* **95**(B10), 15303–15318.

An, Y., Gu, Y. J. & Sacchi, M. D. (2007), 'Imaging mantle discontinuities using least squares radon transform', *Journal of Geophysical Research* **112:B10303**.

Anderson, D. L. (1967), 'Phase changes in the upper mantle', *Science* **157**(3793), 1165–1173.

Anderson, D. L. (1989), *Theory of the Earth*, Blackwell Scientific Publications.

Andrews, J. & Deuss, A. (2008), 'Detailed nature of the 660 km region of the mantle from global receiver function data', *Journal of Geophysical Research: Solid Earth* **113**(B6).

Auvergne, M. (1988), 'Singular value analysis applied to phase space reconstruction of pulsating stars', *Astronomy and Astrophysics* **204**, 341–348.

Bassin, C. (2000), 'The current limits of resolution for surface wave tomography in North America', *Eos Trans. AGU* .

Basu, A. R., Junwen, W., Wankang, H., Guanghong, X. & Tatsumoto, M. (1991), 'Major element, REE, and Pb, Nd and Sr isotopic geochemistry of Cenozoic volcanic rocks of eastern China: implications for their origin from suboceanic-type mantle reservoirs', *Earth and Planetary Science Letters* **105**(1), 149–169.

Baysal, E., Kosloff, D. D. & Sherwood, J. W. (1983), 'Reverse time migration', *Geophysics* **48**(11), 1514–1524.

Bercovici, D. & Karato, S.-i. (2003), 'Whole-mantle convection and the transition-zone water filter', *Nature* **425**(6953), 39–44.

Bijwaard, H., Spakman, W. & Engdahl, E. R. (1998), 'Closing the gap between regional and global travel time tomography', *Journal of Geophysical Research* **103**, 30055–30078.

Bina, C. (2003), 'Seismological constraints upon mantle composition', *Treatise on Geochemistry* **2**, 568.

Bina, C. R. & Helffrich, G. (1994), 'Phase transition Clapeyron slopes and transition zone seismic discontinuity topography', *Journal of Geophysical Research: Solid Earth* **99**(B8), 15853–15860.

Biondi, B., Shan, G. et al. (2002), Prestack imaging of overturned reflections by reverse time migration, *in* 'SEG Technical Program Expanded Abstracts', Vol. 21, pp. 1284–1287.

Bird, P. (2003), 'An updated digital model of plate boundaries', *Geochemistry, Geophysics, Geosystems* **4**(3).

Bock, Y., Prawirodirdjo, L., Genrich, J., Stevens, C., McCaffrey, R., Subarya, C., Puntodewo, S. & Calais, E. (2003), 'Crustal motion in Indonesia from global positioning system measurements', *Journal of Geophysical Research: Solid Earth* **108**(B8).

Bolfan-Casanova, N. (2005), 'Water in the Earths mantle', *Mineralogical Magazine* **69**(3), 229–257.

Braña, L. & Helffrich, G. (2004), ‘A scattering region near the core-mantle boundary under the North Atlantic’, *Geophysical Journal International* **158**(2), 625–636.

Broomhead, D. S. & King, G. P. (1986), ‘Extracting qualitative dynamics from experimental data’, *Physica D: Nonlinear Phenomena* **20**(2-3), 217–236.

Cadzow, J. A. (1988), ‘Signal enhancement-a composite property mapping algorithm’, *Acoustics, Speech and Signal Processing, IEEE Transactions on* **36**(1), 49–62.

Campbell, I. H. (2007), ‘Testing the plume theory’, *Chemical Geology* **241**(3), 153–176.

Canales, L. (1984), ‘Random noise reduction: 54th Annual International Meeting’, *SEG, Expanded Abstracts* .

Cao, Q., Van der Hilst, R., De Hoop, M. & Shim, S.-H. (2011), ‘Seismic imaging of transition zone discontinuities suggests hot mantle west of Hawaii’, *Science* **332**(6033), 1068–1071.

Cao, Q., Wang, P., Van der Hilst, R., De Hoop, M. & Shim, S.-H. (2010), ‘Imaging the upper mantle transition zone with a generalized Radon transform of SS precursors’, *Physics of the Earth and Planetary Interiors* **180**(1), 80–91.

Cardwell, R. K. & Isacks, B. L. (1978), ‘Geometry of the subducted lithosphere beneath the Banda Sea in eastern Indonesia from seismicity and fault plane solutions’, *Journal of Geophysical Research: Solid Earth* **83**(B6), 2825–2838.

Cassidy, J. F. (1995), ‘A comparison of the receiver structure beneath stations of the Canadian National Seismograph Network’, *Canadian Journal of Earth Sciences* **32**(7), 938–951.

Castle, J. C. & Creager, K. C. (2000), 'Local sharpness and shear wave speed jump across the 660 km discontinuity', *Journal of Geophysical Research: Solid Earth* **105**, 6191–6200.

Chambers, K., Deuss, A. & Woodhouse, J. (2005), 'Reflectivity of the 410-km discontinuity from PP and SS precursors', *Journal of Geophysical Research* **110:B02301**.

Chang, W.-F. & McMechan, G. A. (1994), '3-D elastic prestack, reverse-time depth migration', *Geophysics* **59**(4), 597–609.

Chen, K. & Sacchi, M. D. (2015), 'Robust reduced-rank filtering for erratic seismic noise attenuation', *Geophysics* pp. V1–V11.

Chen, W.-P. & Tseng, T.-L. (2007), 'Small 660-km seismic discontinuity beneath Tibet implies resting ground for detached lithosphere', *Journal of Geophysical Research: Solid Earth* **112**(B5).

Chen, Y., Gu, Y. J., Dokht, R. M. & Sacchi, M. D. (2015), 'Crustal imprints of Precambrian orogenesis in western Laurentia', *Journal of Geophysical Research: Solid Earth* **120**(10), 6993–7012.

Chen, Y. & Ma, J. (2014), 'Random noise attenuation by f-x empirical mode decomposition predictive filtering', *Geophysics* pp. V81–V91.

Claerbout, J. F. & Doherty, S. M. (1972), 'Downward continuation of moveout-corrected seismograms', *Geophysics* **37**(5), 741–768.

Courtier, A. M. & Revenaugh, J. (2006), 'A water-rich transition zone beneath the eastern United States and Gulf of Mexico from multiple ScS reverberations', *Earth's Deep Water Cycle* pp. 181–193.

Creager, K. C. & Jordan, T. H. (1986), 'Slab penetration into the lower mantle beneath the Mariana and other island arcs of the northwest Pacific', *Journal of Geophysical Research* **91**, 3573–3589.

Curray, J., Moore, D., Lawver, L., Emmel, F., Raitt, R., Henry, M. & Kieckhefer, R. (1979), 'Tectonics of the Andaman Sea and Burma: convergent margins', *AAPG Special Volumes* **29**, 189–198.

DeMets, C., Gordon, R. G. & Argus, D. F. (2010), 'Geologically current plate motions', *Geophysical Journal International* **181**(1), 1–80.

Deon, F., Koch-Müller, M., Rhede, D. & Wirth, R. (2011), 'Water and iron effect on the P–T–x coordinates of the 410-km discontinuity in the Earth upper mantle', *Contributions to Mineralogy and Petrology* **161**(4), 653–666.

Deuss, A. (2007), 'Seismic observations of transition-zone discontinuities beneath hotspot locations', *Geological Society of America Special Papers* **430**, 121–136.

Deuss, A. (2009), 'Global observations of mantle discontinuities using SS and PP precursors', *Surveys in Geophysics* **30**(4-5), 301–326.

Deuss, A. & Woodhouse, J. (2001), 'Seismic observations of splitting of the mid-transition zone discontinuity in Earth's mantle', *Science* **294**(5541), 354–357.

Deuss, A. & Woodhouse, J. H. (2002), 'A systematic search for mantle discontinuities using SS-precursors', *Geophysical Research Letters* **29**(8).

Di Leo, J., Wookey, J., Hammond, J., Kendall, J.-M., Kaneshima, S., Inoue, H., Yamashina, T. & Harjadi, P. (2012), 'Mantle flow in regions of complex tectonics: Insights from Indonesia', *Geochemistry, Geophysics, Geosystems* **13**(12).

Dokht, R. M., Gu, Y. J. & Sacchi, M. D. (2016), 'Waveform inversion of SS precursors: An investigation of the northwestern Pacific subduction zones and intraplate volcanoes in China', *Gondwana Research* **40**, 77–90.

Dueker, K. G. & Sheehan, A. F. (1997), 'Mantle discontinuity structure from midpoint stacks of converted P to S waves across the Yellowstone hotspot track', *Journal of Geophysical Research: Solid Earth* **102**(B4), 8313–8327.

Duffy, T. S. & Anderson, D. L. (1989), 'Seismic velocities in mantle minerals and the mineralogy of the upper mantle', *Journal of Geophysical Research: Solid Earth* **94**(B2), 1895–1912.

Dziewonski, A. M. & Anderson, D. L. (1981), 'Preliminary reference Earth model', *Physics of the Earth and Planetary Interiors* **25**(4), 297–356.

Edwards, C. M., Menzies, M. A., Thirwall, M. F., Morris, J. D., Leeman, W. P. & Harmon, R. S. (1994), 'The Transition to Potassic Alkaline Volcanism in Island Arcs: The RinggitBeser Complex, East Java, Indonesia', *Journal of Petrology* **35**(6), 1557–1595.

Efron, B. & Tibshirani, R. (1991), 'Statistical data analysis in the computer age', *Science* **253**(5018), 390–395.

Etgen, J., Gray, S. H. & Zhang, Y. (2009), 'An overview of depth imaging in exploration geophysics', *Geophysics* **74**(6), WCA5–WCA17.

Faccenna, C., Becker, T. W., Lallemand, S., Lagabrielle, Y., Funiciello, F. & Piromallo, C. (2010), 'Subduction-triggered magmatic pulses: A new class of plumes?', *Earth and Planetary Science Letters* **299**(1), 54–68.

Farra, V. & Vinnik, L. (2000), 'Upper mantle stratification by P and S receiver functions', *Geophysical Journal International* **141**(3), 699–712.

Fee, D. & Dueker, K. (2004), 'Mantle transition zone topography and structure beneath the Yellowstone hotspot', *Geophysical Research Letters* **31**(18).

Fei, Y. & Bertka, C. M. (1999), 'Phase transitions in the Earth's mantle and mantle mineralogy', *Mantle petrology: field observations and high pressure experimentation* **6**, 189–207.

Fichtner, A., De Wit, M. & van Bergen, M. (2010), 'Subduction of continental lithosphere in the Banda Sea region: Combining evidence from full waveform tomography and isotope ratios', *Earth and Planetary Science Letters* **297**(3), 405–412.

Fichtner, A. & Igel, H. (2008), 'Efficient numerical surface wave propagation through the optimization of discrete crustal models – a technique based on non-linear dispersion curve matching (DCM)', *Geophysical Journal International* **173**(2), 519–533.

Flanagan, M. P. & Shearer, P. M. (1998), 'Global mapping of topography on transition zone velocity discontinuities by stacking SS precursors', *Journal of Geophysical Research* **103**(B2), 2673–2692.

Fraedrich, K. (1986), 'Estimating the dimensions of weather and climate attractors', *Journal of the atmospheric sciences* **43**(5), 419–432.

Frederiksen, A. & Revenaugh, J. (2004), 'Lithospheric imaging via teleseismic scattering tomography', *Geophysical Journal International* **159**(3), 978–990.

Freire, S. L. & Ulrych, T. J. (1988), 'Application of Singular value decomposition to vertical seismic profiling', *Geophysics* **53**, 778–785.

Friederich, W. (1999), 'Propagation of seismic shear and surface waves in a laterally heterogeneous mantle by multiple forward scattering', *Geophysical Journal International* **136**(1), 180–204.

Friederich, W. (2003), 'The S-velocity structure of the East Asian mantle from inversion of shear and surface waveforms', *Geophysical Journal International* **153**(1), 88–102.

Friederich, W. & Dalkolmo, J. (1995), 'Complete synthetic seismograms for a spherically symmetric earth by a numerical computation of the Green's function in the frequency domain', *Geophysical Journal International* **122**(2), 537–550.

Frost, D. J. (2008), 'The upper mantle and transition zone', *Elements* **4**(3), 171–176.

Frost, D. J. & Dolejš, D. (2007), 'Experimental determination of the effect of H_2O on the 410-km seismic discontinuity', *Earth and Planetary Science Letters* **256**(1), 182–195.

Fukao, Y. & Obayashi, M. (2013), 'Subducted slabs stagnant above, penetrating through, and trapped below the 660 km discontinuity', *Journal of Geophysical Research: Solid Earth* **118**(11), 5920–5938.

Fukao, Y., Obayashi, M., Inoue, H. & Nenbai, M. (1992), 'Subducting slabs stagnant in the mantle transition zone', *Journal of Geophysical Research: Solid Earth* **97**(B4), 4809–4822.

Fukao, Y., Obayashi, M. & Nakakuki, T. (2009), 'Stagnant slab: a review', *Annual Review of Earth and Planetary Sciences* **37**, 19–46.

Fukao, Y., Widiyantoro, S. & Obayashi, M. (2001), 'Stagnant slabs in the upper and lower mantle transition region', *Reviews of Geophysics* **39**(3), 291–323.

Gaherty, J. B., Jordan, T. H. & Gee, L. S. (1996), 'Seismic structure of the upper mantle in a central Pacific corridor', *Journal of Geophysical Research: Solid Earth* **101**(B10), 22291–22309.

Gazdag, J. (1978), 'Wave equation migration with the phase-shift method', *Geophysics* **43**(7), 1342–1351.

Gazdag, J. & Sguazzero, P. (1984), 'Migration of seismic data', *Proceedings of the IEEE* **72**(10), 1302–1315.

Ghil, M., Allen, M., Dettinger, M., Ide, K., Kondrashov, D., Mann, M., Robertson, A. W., Saunders, A., Tian, Y., Varadi, F. et al. (2002), 'Advanced spectral methods for climatic time series', *Reviews of geophysics* **40**(1).

Golub, G. H. & Van Loan, C. F. (1996), *Matrix computations, 3rd ed.*, Johns Hopkins University Press, Baltimore, MD,.

Golyandina, N., Nekrutkin, V. & Zhigljavsky, A. (2001), *Analysis of Time Series Structure: SSA and Related Techniques*, Chapman & Hall/CRC Monographs on Statistics & Applied Probability, CRC Press.

Gorbatov, A. & Kennett, B. (2003), 'Joint bulk-sound and shear tomography for Western Pacific subduction zones', *Earth and Planetary Science Letters* **210**(3), 527–543.

Gossler, J. & Kind, R. (1996), 'Seismic evidence for very deep roots of continents', *Earth and Planetary Science Letters* **138**(1), 1–13.

Grand, S. P. (2002), 'Mantle shear–wave tomography and the fate of subducted slabs', *Philosophical Transactions of the Royal Society of London A: Mathematical, Physical and Engineering Sciences* **360**(1800), 2475–2491.

Grand, S. P., van der Hilst, R. D. & Widiyantoro, S. (1997), 'Global seismic tomography: a snapshot of convection in the Earth', *GSA Today* **7**(4), 1–7.

Gray, S. H., Etgen, J., Dellinger, J. & Whitmore, D. (2001), 'Seismic migration problems and solutions', *Geophysics* **66**(5), 1622–1640.

Gu, Y., Dziewonski, A. M. & Agee, C. B. (1998), 'Global de-correlation of the topography of transition zone discontinuities', *Earth and Planetary Science Letters* **157**(1), 57–67.

Gu, Y. J. & Dziewonski, A. M. (2002), 'Global variability of transition zone thickness', *Journal of Geophysical Research* **107:2135**(B7).

Gu, Y. J., Dziewoński, A. M. & Ekström, G. (2003), 'Simultaneous inversion for mantle shear velocity and topography of transition zone discontinuities', *Geophysical Journal International* **154**(2), 559–583.

Gu, Y. J., Okeler, A. & Schultz, R. (2012), 'Tracking slabs beneath northwestern Pacific subduction zones', *Earth and Planetary Science Letters* **331**, 269–280.

Gu, Y. J., Okeler, A., Shen, L. & Contenti, S. (2011), 'The Canadian Rockies and Alberta network (CRANE): new constraints on the Rockies and western Canada sedimentary basin', *Seismological Research Letters* **82**(4), 575–588.

Gu, Y. J. & Sacchi, M. (2009), 'Radon transform methods and their applications in mapping mantle reflectivity structure', *Surveys in Geophysics* **30**(4-5), 327–354.

Gu, Y. J. & Shen, L. (2015), 'Noise correlation tomography of Southwest Western Canada Sedimentary Basin', *Geophysical Journal International* **202**(1), 142–162.

Gu, Y. J., Zhang, Y., Sacchi, M. D., Chen, Y. & Contenti, S. (2015), 'Sharp mantle transition from cratons to Cordillera in southwestern Canada', *Journal of Geophysical Research: Solid Earth* **120**(7), 5051–5069.

Gudmundsson, Ó. & Sambridge, M. (1998), 'A regionalized upper mantle (RUM) seismic model', *Journal of Geophysical Research* **103**, 7121–7136.

Gulunay, N. et al. (1986), FXDECON and complex Wiener prediction filter, *in* '1986 SEG Annual Meeting', Society of Exploration Geophysicists.

Gung, Y. & Romanowicz, B. (2004), 'Q tomography of the upper mantle using three-component long-period waveforms', *Geophysical Journal International* **157**(2), 813–830.

Hall, R., Cross, L., Clements, B. & Spakman, W. (2009), Neogene subduction beneath Java: slab tearing, arc deformation and arc magmatism, and their causes, *in* 'Southeast Asian Gateway Evolution Conference (abstract). Royal Holloway University of London, United Kingdom'.

Hall, R. & Spakman, W. (2015), 'Mantle structure and tectonic history of SE Asia', *Tectonophysics* **658**, 14–45.

Hamilton, W. B. (1974), Earthquake map of the Indonesian region, Technical report.

Hanitzsch, C. (1997), 'Comparison of weights in prestack amplitude-preserving Kirchhoff depth migration', *Geophysics* **62**(6), 1812–1816.

Hassani, H. & Thomakos, D. (2010), 'A review on singular spectrum analysis for economic and financial time series', *Statistics and its Interface* **3**(3), 377–397.

Haupt, R. L. & Haupt, S. E. (2004), *Practical Genetic Algorithm, Second Edition*, John Wiley & Sons, New Jersey.

Hayes, G. P., Wald, D. J. & Johnson, R. L. (2012), 'Slab1.0: A three-dimensional model of global subduction zone geometries', *Journal of Geophysical Research* **117**.

Heit, B., Yuan, X., Bianchi, M., Kind, R. & Gossler, J. (2010), 'Study of the lithospheric and upper-mantle discontinuities beneath eastern Asia by SS precursors', *Geophysical Journal International* **183**(1), 252–266.

Helmberger, D. & Wiggins, R. A. (1971), 'Upper mantle structure of midwestern United States', *Journal of Geophysical Research* **76**(14), 3229–3245.

Honda, S., Morishige, M. & Orihashi, Y. (2007), 'Sinking hot anomaly trapped at the 410 km discontinuity near the Honshu subduction zone, Japan', *Earth and Planetary Science Letters* **261**(3), 565–577.

Houser, C., Masters, G., Flanagan, M. & Shearer, P. (2008), 'Determination and analysis of long-wavelength transition zone structure using SS precursors', *Geophysical Journal International* **174**(1), 178–194.

Houser, C. & Williams, Q. (2010), 'Reconciling Pacific 410 and 660km discontinuity topography, transition zone shear velocity patterns, and mantle phase transitions', *Earth and Planetary Science Letters* **296**(3), 255–266.

Huang, J. & Zhao, D. (2006), 'High-resolution mantle tomography of China and surrounding regions', *Journal of Geophysical Research* **111:B09305**.

Huang, Z., Zhao, D. & Wang, L. (2015), 'P wave tomography and anisotropy beneath Southeast Asia: Insight into mantle dynamics', *Journal of Geophysical Research: Solid Earth* **120**(7), 5154–5174.

Ichiki, M., Baba, K., Obayashi, M. & Utada, H. (2006), 'Water content and geotherm in the upper mantle above the stagnant slab: Interpretation of electrical conductivity and seismic P-wave velocity models', *Physics of the Earth and Planetary Interiors* **155**(1), 1–15.

Inoue, T., Yurimoto, H. & Kudoh, Y. (1995), 'Hydrous modified spinel, Mg1. 75SiH0. 5O4: a new water reservoir in the mantle transition region', *Geophysical Research Letters* **22**(2), 117–120.

IRIS, DMC (2013), 'Data Services Products', *SEMum, a high-resolution global model of upper mantle structure* .

Ita, J. & Stixrude, L. (1992), 'Petrology, elasticity, and composition of the mantle transition zone', *Journal of Geophysical Research: Solid Earth* **97**(B5), 6849–6866.

Ito, E. & Takahashi, E. (1989), 'Postspinel transformations in the system Mg_2SiO_4-Fe_2SiO_4 and some geophysical implications', *Journal of Geophysical Research* **94**(B8), 10637–10646.

Jackson, M. G. & Dasgupta, R. (2008), 'Compositions of HIMU, EM1, and EM2 from global trends between radiogenic isotopes and major elements in ocean island basalts', *Earth and Planetary Science Letters* **276**(1), 175–186.

Jeanloz, R. & Thompson, A. B. (1983), 'Phase transitions and mantle discontinuities', *Reviews of Geophysics* **21**(1), 51–74.

Jordan, T. (1977), 'Lithospheric slab penetration into the lower mantle beneath the Sea of Okhotsk', *Journal of Geophysics* **43**, 473–496.

Karato, S.-I., Bercovici, D., Leahy, G., Richard, G. & Jing, Z. (2006), 'The Transition-Zone Water Filter Model for Global Material Circulation: Where Do We stand?', *Earth's Deep Water Cycle* pp. 289–313.

Katili, J. A. (1975), 'Volcanism and plate tectonics in the Indonesian island arcs', *Tectonophysics* **26**(3-4), 165–188.

Katsura, T. & Ito, E. (1989), 'The system Mg_2SiO_4-Fe_2SiO_4 at high pressures and temperatures: Precise determination of stabilities of olivine, modified spinel, and spinel', *Journal of Geophysical Research* **94**(B11), 15663–15670.

Kazemi, N. & Siahkoohi, H. (2012), 'Local stretch zeroing NMO correction', *Geophysical Journal International* **188**(1), 123–130.

Kennett, B. (1983), 'Seismic wave propagation in stratified media, Cambridge Univ.', *Pres., Cambridge* .

Kennett, B. & Engdahl, E. (1991), 'Traveltimes for global earthquake location and phase identification', *Geophysical Journal International* **105**(2), 429–465.

Kind, R., Ni, J., Zhao, W., Wu, J. et al. (1996), 'Evidence from earthquake data for a partially molten crustal layer in southern Tibet', *Science* **274**(5293), 1692.

Kind, R., Yuan, X., Saul, J., Nelson, D., Sobolev, S., Mechie, J., Zhao, W., Kosarev, G., Ni, J., Achauer, U. et al. (2002), 'Seismic images of crust and upper mantle beneath Tibet: evidence for Eurasian plate subduction', *Science* **298**(5596), 1219–1221.

Kühl, H. & Sacchi, M. D. (2003), 'Least-squares wave-equation migration for AVP/AVA inversion', *Geophysics* **68**(1), 262–273.

Kumar, U. & Jain, V. (2010), 'Time series models (Grey-Markov, Grey Model with rolling mechanism and singular spectrum analysis) to forecast energy consumption in India', *Energy* **35**(4), 1709–1716.

Kuritani, T., Kimura, J.-I., Miyamoto, T., Wei, H., Shimano, T., Maeno, F., Jin, X. & Taniguchi, H. (2009), 'Intraplate magmatism related to deceleration of upwelling asthenospheric mantle: Implications from the Changbaishan shield basalts, northeast China', *Lithos* **112**(3), 247–258.

Langston, C. A. (1979), 'Structure under Mount Rainier, Washington, inferred from teleseismic body waves', *Journal of Geophysical Research: Solid Earth* **84**(B9), 4749–4762.

Larson, R. (1991), 'Latest pulse of Earth: Evidence for a mid-Cretaceous superplume', *Geology* **19**(6), 547–550.

Laske, G., Masters, G., Ma, Z. & Pasyanos, M. (2013), 'Update on CRUST1.0 - A 1-degree global model of Earth's crust', **15**, Abstract EGU2013–2658.

Lawrence, J. F. & Shearer, P. M. (2006*a*), 'A global study of transition zone thickness using receiver functions', *Journal of Geophysical Research* **111:B06307**.

Lawrence, J. F. & Shearer, P. M. (2006*b*), 'Constraining seismic velocity and density for the mantle transition zone with reflected and transmitted waveforms', *Geochemistry, Geophysics, Geosystems* **7**(10).

Lawrence, J. F. & Shearer, P. M. (2008), 'Imaging mantle transition zone thickness with SdS-SS finite-frequency sensitivity kernels', *Geophysical Journal International* **174**(1), 143–158.

Lebedev, S., Chevrot, S. & Van Der Hilst, R. (2003), 'Correlation between the shear-speed structure and thickness of the mantle transition zone', *Physics of the Earth and Planetary Interiors* **136**(1), 25–40.

Lebedev, S. & van der Hilst, R. D. (2008), 'Global upper-mantle tomography with the automated multimode inversion of surface and S-wave forms', *Geophysical Journal International* **173**(2), 505–518.

Lei, J. & Zhao, D. (2005), 'P-wave tomography and origin of the Changbai intraplate volcano in Northeast Asia', *Tectonophysics* **397**(3), 281–295.

Lekić, V. & Romanowicz, B. (2011), 'Inferring upper-mantle structure by full waveform tomography with the spectral element method', *Geophysical Journal International* **185**(2), 799–831.

Lessing, S., Thomas, C., Rost, S., Cobden, L. & Dobson, D. P. (2014), 'Mantle transition zone structure beneath India and Western China from migration of PP and SS precursors', *Geophysical Journal International* **197**(1), 396–413.

Lessing, S., Thomas, C., Saki, M., Schmerr, N. & Vanacore, E. (2015), 'On the difficulties of detecting PP precursors', *Geophysical Journal International* **201**(3), 1666–1681.

Li, A., Fischer, K. M., van der Lee, S. & Wysession, M. E. (2002), 'Crust and upper mantle discontinuity structure beneath eastern North America', *Journal of Geophysical Research: Solid Earth* **107**(B5).

Li, A., Fischer, K. M., Wysession, M. E. & Clarke, T. J. (1998), 'Mantle discontinuities and temperature under the North American continental keel', *Nature* **395**(6698), 160–163.

Li, C. & van der Hilst, R. D. (2010), 'Structure of the upper mantle and transition zone beneath Southeast Asia from traveltime tomography', *Journal of Geophysical Research* **115**.

Li, C., van der Hilst, R. D., Engdahl, E. R. & Burdick, S. (2008), 'A new global model for P wave speed variations in Earth's mantle', *Geochemistry, Geophysics, Geosystems* **9**(5).

Li, X., Sobolev, S., Kind, R., Yuan, X. & Estabrook, C. (2000), 'A detailed receiver function image of the upper mantle discontinuities in the Japan subduction zone', *Earth and Planetary Science Letters* **183**(3), 527–541.

Li, X. & Yuan, X. (2003), 'Receiver functions in northeast China–implications for slab penetration into the lower mantle in northwest Pacific subduction zone', *Earth and Planetary Science Letters* **216**(4), 679–691.

Ligorria, J. P. & Ammon, C. J. (1999), 'Iterative deconvolution and receiver-function estimation', *Bulletin of the seismological Society of America* **89**(5), 1395–1400.

Liu, Q. & Gu, Y. (2012), 'Seismic imaging: From classical to adjoint tomography', *Tectonophysics* **566**, 31–66.

Liu, Z., Niu, F., Chen, Y. J., Grand, S., Kawakatsu, H., Ning, J., Tanaka, S., Obayashi, M. & Ni, J. (2015), 'Receiver function images of the mantle transition zone beneath NE China: New constraints on intraplate volcanism, deep subduction and their potential link', *Earth and Planetary Science Letters* **412**, 101–111.

Long, M. D. & Silver, P. G. (2008), 'The subduction zone flow field from seismic anisotropy: A global view', *science* **319**(5861), 315–318.

Lynner, C. & Long, M. D. (2014), 'Sub-slab anisotropy beneath the Sumatra and circum-Pacific subduction zones from source-side shear wave splitting observations', *Geochemistry, Geophysics, Geosystems* **15**(6), 2262–2281.

Marone, F., Gung, Y. & Romanowicz, B. (2007), 'Three-dimensional radial anisotropic structure of the North American upper mantle from inversion of surface waveform data', *Geophysical Journal International* **171**(1), 206–222.

Mégnin, C. & Romanowicz, B. (2000), 'The three-dimensional shear velocity structure of the mantle from the inversion of body, surface and higher-mode waveforms', *Geophysical Journal International* **143**(3), 709–728.

Minster, J. B. & Jordan, T. H. (1978), 'Present-day plate motions', *Journal of Geophysical Research: Solid Earth* **83**(B11), 5331–5354.

Naghizadeh, M. (2012), 'Seismic data interpolation and denoising in the frequency-wavenumber domain', *Geophysics* **77**(2), V71–V80.

Naghizadeh, M. & Sacchi, M. (2013), 'Multidimensional de-aliased Cadzow reconstruction of seismic records', *Geophysics* **78**(1), A1–A5.

Navrotsky, A. (1980), 'Lower mantle phase transitions may generally have negative pressure-temperature slopes', *Geophysical Research Letters* **7**(9), 709–711.

Neele, F., de Regt, H. & Van Decar, J. (1997), 'Gross errors in upper-mantle discontinuity topography from underside reflection data', *Geophysical Journal International* **129**(1), 194–204.

Niu, Y. (2005), 'Generation and evolution of basaltic magmas: some basic concepts and a new view on the origin of Mesozoic–Cenozoic basaltic volcanism in eastern China', *Geological Journal of Chine Universities* **11**, 9–46.

Niu, Y. (2014), 'Geological understanding of plate tectonics: basic concepts, illustrations, examples and new perspectives.', *Global tectonics and metallogeny.* **10**(1), 23–46.

Obayashi, M., Sugioka, H., Yoshimitsu, J. & Fukao, Y. (2006), 'High temperature anomalies oceanward of subducting slabs at the 410-km discontinuity', *Earth and Planetary Science Letters* **243**(1), 149–158.

Ohtani, E., Litasov, K., Hosoya, T., Kubo, T. & Kondo, T. (2004), 'Water transport into the deep mantle and formation of a hydrous transition zone', *Physics of the Earth and Planetary Interiors* **143**, 255–269.

Oropeza, V. & Sacchi, M. (2011), 'Simultaneous seismic data denoising and reconstruction via multichannel singular spectrum analysis', *Geophysics* **76**, V25–V32.

Piazzoni, A., Steinle-Neumann, G., Bunge, H.-P. & Dolejš, D. (2007), 'A mineralogical model for density and elasticity of the Earth's mantle', *Geochemistry, Geophysics, Geosystems* **8**(11).

Priestley, K., Debayle, E., McKenzie, D. & Pilidou, S. (2006), 'Upper mantle structure of eastern Asia from multimode surface waveform tomography', *Journal of Geophysical Research: Solid Earth* **111 (B10)**.

Puspito, N. T. & Shimazaki, K. (1995), 'Mantle structure and seismotectonics of the sunda and banda arcs', *Tectonophysics* **251**(1), 215–228.

Puspito, N. T., Yamanaka, Y., Miyatake, T., Shimazaki, K. & Hirahara, K. (1993), 'Three-dimensional P-wave velocity structure beneath the Indonesian region', *Tectonophysics* **220**(1), 175–192.

Replumaz, A., Kárason, H., van der Hilst, R. D., Besse, J. & Tapponnier, P. (2004), '4-D evolution of SE Asias mantle from geological reconstructions and seismic tomography', *Earth and Planetary Science Letters* **221**(1), 103–115.

Revenaugh, J. & Jordan, T. H. (1991), 'Mantle layering from ScS reverberations: 2. The transition zone', *Journal of Geophysical Research* **96**(B12), 19763–19780.

Revenaugh, J. & Sipkin, S. (1994*a*), 'Seismic evidence for silicate melt atop the 410-km mantle discontinuity', *Nature* **369**(6480), 474–476.

Revenaugh, J. & Sipkin, S. A. (1994*b*), 'Mantle discontinuity structure beneath China', *Journal of Geophysical Research* **99**(B11), 21911–21927.

Ringwood, A. E. (1975), *Composition and petrology of the earth's mantle*, McGraw-Hill.

Ritsema, J., Deuss, A., Van Heijst, H. & Woodhouse, J. (2011), 'S40RTS: a degree-40 shear-velocity model for the mantle from new Rayleigh wave dispersion, teleseismic traveltime and normal-mode splitting function measurements', *Geophysical Journal International* **184**, 1223–1236.

Ritsema, J., van Heijst, H. J. & Woodhouse, J. H. (1999), 'Complex shear wave velocity structure imaged beneath Africa and Iceland', *Science* **286**(5446), 1925–1928.

Rondenay, S. (2009), 'Upper mantle imaging with array recordings of converted and scattered teleseismic waves', *Surveys in geophysics* **30**(4-5), 377–405.

Rost, S. & Thomas, C. (2009), 'Improving seismic resolution through array processing techniques', *Surveys in Geophysics* **30**(4-5), 271–299.

Sacchi, M. D. (1998), 'A bootstrap procedure for high-resolution velocity analysis', *Geophysics* **63**(5), 1716–1725.

Sacchi, M. D. (2009), 'FX Singular Spectrum Analysis', *CSPG CSEG CWLS Convention* pp. 392–395.

Sacchi, M. D. & Ulrych, T. J. (1995), 'High-resolution velocity gathers and offset space reconstruction', *Geophysics* **60**(4), 1169–1177.

Saita, T., Suetsugu, D., Ohtaki, T., Takenaka, H., Kanjo, K. & Purwana, I. (2002), 'Transition zone thickness beneath Indonesia as inferred using the receiver function method for data from the JISNET regional broadband seismic network', *Geophysical research letters* **29**(7).

Schaeffer, A. & Bostock, M. (2010), 'A low-velocity zone atop the transition zone in northwestern Canada', *Journal of Geophysical Research: Solid Earth* **115**(B6).

Schmandt, B. & Humphreys, E. (2010), ‘Complex subduction and small-scale convection revealed by body-wave tomography of the western United States upper mantle’, *Earth and Planetary Science Letters* **297**(3), 435–445.

Schmerr, N. & Garnero, E. (2006), ‘Investigation of upper mantle discontinuity structure beneath the central Pacific using SS precursors’, *Journal of Geophysical Research* **111:B08305**.

Schmerr, N. & Garnero, E. J. (2007), ‘Upper mantle discontinuity topography from thermal and chemical heterogeneity’, *Science* **318**(5850), 623–626.

Schmerr, N. & Thomas, C. (2011), ‘Subducted lithosphere beneath the Kuriles from migration of PP precursors’, *Earth and Planetary Science Letters* **311**(1), 101–111.

Schneider, W. (1978), ‘Integral formulation for migration in 2 and 3 dimensions’, *Geophysics* **43**(1), 49–76.

Schultz, R. & Gu, Y. J. (2013), ‘Multiresolution imaging of mantle reflectivity structure using SS and P′ P′ precursors’, *Geophysical Journal International* p. ggt266.

Shearer, P. (1990), ‘Seismic imaging of upper-mantle structure with new evidence for a n520-Km discontinuity’, *Nature* **344**(6262), 121–126.

Shearer, P. M. (1991), ‘Constraints on upper mantle discontinuities from observations of long-period reflected and converted phases’, *Journal of Geophysical Research* **96**, 18147–18182.

Shearer, P. M. (1993), ‘Global mapping of upper mantle reflectors from long-period SS precursors’, *Geophysical Journal International* **115**(3), 878–904.

Shearer, P. M. (2009), *Introduction to seismology*, Cambridge University Press.

Shearer, P. M., Flanagan, M. P. & Hedlin, M. A. (1999), 'Experiments in migration processing of SS precursor data to image upper mantle discontinuity structure', *Journal of Geophysical Research: Solid Earth* **104**(B4), 7229–7242.

Shearer, P. M. & Masters, T. G. (1992), 'Global mapping of topography on the 660-km discontinuity', *Nature* **355**(6363), 791–796.

Sheriff, R. E. & Geldart, L. P. (1995), *Exploration seismology*, Cambridge university press.

Simmons, N. A., Forte, A. M., Boschi, L. & Grand, S. P. (2010), 'GyPSuM: A joint tomographic model of mantle density and seismic wave speeds', *Journal of Geophysical Research: Solid Earth* **115**(B12).

Simmons, N. A., Forte, A. M. & Grand, S. P. (2007), 'Thermochemical structure and dynamics of the African superplume', *Geophysical Research Letters* **34**(2).

Simons, W., Socquet, A., Vigny, C., Ambrosius, B., Haji Abu, S., Promthong, C., Subarya, C., Sarsito, D., Matheussen, S., Morgan, P. et al. (2007), 'A decade of GPS in Southeast Asia: Resolving Sundaland motion and boundaries', *Journal of Geophysical Research: Solid Earth* **112**(B6).

Song, T.-R. A., Helmberger, D. V. & Grand, S. P. (2004), 'Low-velocity zone atop the 410-km seismic discontinuity in the northwestern United States', *Nature* **427**(6974), 530–533.

Spakman, W. & Hall, R. (2010), 'Surface deformation and slab–mantle interaction during Banda arc subduction rollback', *Nature Geoscience* **3**(8), 562–566.

Spitz, S. (1991), 'Seismic trace interpolation in the FX domain', *Geophysics* **56**(6), 785–794.

Stixrude, L. & Lithgow-Bertelloni, C. (2005), 'Thermodynamics of mantle mineralsI. Physical properties', *Geophysical Journal International* **162**(2), 610–632.

Stoffa, P. L. & Sen, M. K. (1991), 'Nonlinear multiparameter optimization using genetic algorithms: Inversion of plane-wave seismograms', *Geophysics* **56**(11), 1794–1810.

Tang, Y., Obayashi, M., Niu, F., Grand, S. P., Chen, Y. J., Kawakatsu, H., Tanaka, S., Ning, J. & Ni, J. F. (2014), 'Changbaishan volcanism in northeast China linked to subduction-induced mantle upwelling', *Nature Geoscience* **7**, 470–475.

Tatsumi, Y., Maruyama, S. & Nohda, S. (1990), 'Mechanism of backarc opening in the Japan Sea: role of asthenospheric injection', *Tectonophysics* **181**(1), 299–306.

Tatsumi, Y., Shinjoe, H., Ishizuka, H., Sager, W. W. & Klaus, A. (1998), 'Geochemical evidence for a mid-Cretaceous superplume', *Geology* **26**(2), 151–154.

Tauzin, B., Debayle, E. & Wittlinger, G. (2008), 'The mantle transition zone as seen by global Pds phases: no clear evidence for a thin transition zone beneath hotspots', *Journal of Geophysical Research: Solid Earth* **113:B08309**.

Thomas, C. & Billen, M. I. (2009), 'Mantle transition zone structure along a profile in the SW Pacific: thermal and compositional variations', *Geophysical Journal International* **176**(1), 113–125.

Thomas, C., Kendall, J.-M. & Lowman, J. (2004), 'Lower-mantle seismic discontinuities and the thermal morphology of subducted slabs', *Earth and Planetary Science Letters* **225**(1), 105–113.

Tibi, R., Wiens, D. A., Shiobara, H., Sugioka, H. & Yuan, X. (2007), 'Double seismic discontinuities at the base of the mantle transition zone near the Mariana slab', *Geophysical Research Letters* **34**(16).

Trad, D. O., Ulrych, T. J. & Sacchi, M. D. (2002), 'Accurate interpolation with high-resolution time-variant Radon transforms', *Geophysics* **67**(2), 644–656.

Trickett, S. & Burroughs, L. (2009), 'Prestack rank-reduction-based noise suppression', *CSEG Recorder* **34**(9), 24–31.

Trickett, S. R. (2003), 'F-xy eigenimage noise suppression', *Geophysics* pp. 751–759.

Trickett, S. et al. (2008), F-xy Cadzow noise suppression, *in* '2008 SEG Annual Meeting', Society of Exploration Geophysicists.

Vacher, P., Mocquet, A. & Sotin, C. (1998), 'Computation of seismic profiles from mineral physics: the importance of the non-olivine components for explaining the 660 km depth discontinuity', *Physics of the Earth and Planetary Interiors* **106**(3), 275–298.

van der Hilst, R., Engdahl, E. & Spakman, W. (1993), 'Tomographic inversion of P and pP data for aspherical mantle structure below the northwest Pacific region', *Geophysical Journal International* **115**, 264–302.

van der Hilst, R., Engdahl, E., Spakman, W. & Nolet, G. (1991), 'Tomographic imaging of subducted lithosphere below northwest Pacific island arcs', *Nature* **353**, 37–42.

Varadi, F., Pap, J., Ulrich, R., Bertello, L. & Henney, C. (1999), 'Searching for signal in noise by random-lag singular spectrum analysis', *The Astrophysical Journal* **526**(2), 1052.

Vautard, R. & Ghil, M. (1989), 'Singular spectrum analysis in nonlinear dynamics, with applications to paleoclimatic time series', *Physica D: Nonlinear Phenomena* **35**, 395–424.

Vinnik, L. (1977), 'Detection of waves converted from P to SV in the mantle', *Physics of the Earth and planetary interiors* **15**(1), 39–45.

Vinnik, L. & Farra, V. (2002), 'Subcratonic low-velocity layer and flood basalts', *Geophysical Research Letters* **29**(4).

Wang, Y., Wen, L. & Weidner, D. (2008), 'Upper mantle SH-and P-velocity structures and compositional models beneath southern Africa', *Earth and Planetary Science Letters* **267**(3), 596–608.

Wang, Y., Wen, L., Weidner, D. & He, Y. (2006), 'SH velocity and compositional models near the 660-km discontinuity beneath South America and northeast Asia', *Journal of Geophysical Research: Solid Earth* **111**(B7).

Weidner, D. J. & Wang, Y. (1998), 'Chemical-and Clapeyron-induced buoyancy at the 660 km discontinuity', *Journal of geophysical research* **103**(134), 7431–7441.

Weidner, D. J. & Wang, Y. (2000), 'Phase transformations: implications for mantle structure', *Earth's Deep Interior: Mineral Physics and Tomography From the Atomic to the Global Scale* pp. 215–235.

Wicks, C. W. & Richards, M. A. (1993), 'A detailed map of the 660-kilometer discontinuity beneath the Izu-Bonin subduction zone', *Science* **261**(5127), 1424–1427.

Widiyantoro, S., Pesicek, J. D. & Thurber, C. H. (2011*a*), 'Complex structure of the lithospheric slab beneath the Banda arc, eastern Indonesia depicted by a seismic tomographic model', *Research in Geophysics* **1**(1), 1.

Widiyantoro, S., Pesicek, J. & Thurber, C. (2011*b*), 'Subducting slab structure below the eastern Sunda arc inferred from non-linear seismic tomographic imaging', *Geological Society, London, Special Publications* **355**(1), 139–155.

Widiyantoro, S. & van der Hilst, R. (1996), 'Structure and evolution of lithospheric slab beneath the sunda arc, indonesia', *Science* **271**(5255), 1566.

Widiyantoro, S. & van der Hilst, R. (1997), 'Mantle structure beneath Indonesia inferred from high-resolution tomographic imaging', *Geophysical Journal International* **130**(1), 167–182.

Yang, H. H. & Hua, Y. (1996), 'On rank of block Hankel matrix for 2-D frequency detection and estimation', *Signal Processing, IEEE Transactions on* **44**(4), 1046–1048.

Ye, L., Li, J., Tseng, T.-L. & Yao, Z. (2011), 'A stagnant slab in a water-bearing mantle transition zone beneath northeast China: implications from regional SH waveform modelling', *Geophysical Journal International* **186**(2), 706–710.

Yuan, H. & Romanowicz, B. (2010), 'Lithospheric layering in the North American craton', *Nature* **466**(7310), 1063–1068.

Yuan, S. & Wang, S. (2011), 'A local f-x Cadzow method for noise reduction of seismic data obtained in complex formations', *Petroleum Science* **8**, 269–277.

Zhao, D. (2007), 'Seismic images under 60 hotspots: Search for mantle plumes', *Gondwana Research* **12**, 335–355.

Zhao, D., Lei, J. & Tang, R. (2004), 'Origin of the Changbai intraplate volcanism in Northeast China: evidence from seismic tomography', *Chinese Science Bulletin* **49**(13), 1401–1408.

Zhao, D. & Liu, L. (2010), 'Deep structure and origin of active volcanoes in China', *Geoscience Frontiers* **1**(1), 31–44.

Zhao, D. & Ohtani, E. (2009), 'Deep slab subduction and dehydration and their geodynamic consequences: evidence from seismology and mineral physics', *Gondwana Research* **16**(3), 401–413.

Zhao, D. & Tian, Y. (2013), 'Changbai intraplate volcanism and deep earthquakes in East Asia: a possible link?', *Geophysical Journal International* **195**(2), 706–724.

Zhao, D., Yanada, T., Hasegawa, A., Umino, N. & Wei, W. (2012), 'Imaging the subducting slabs and mantle upwelling under the Japan Islands', *Geophysical Journal International* **190**(2), 816–828.

Zheng, Z. & Romanowicz, B. (2012), 'Do double SS precursors mean double discontinuities?', *Geophysical Journal International* **191**(3), 1361–1373.

Zheng, Z., Ventosa, S. & Romanowicz, B. (2015), 'High resolution upper mantle discontinuity images across the Pacific Ocean from SS precursors using local slant stack filters', *Geophysical Journal International* **202**(1), 175–189.

Appendix A
Effect of Attenuation on the Precursor Amplitudes beneath the NW Pacific Subduction Zones

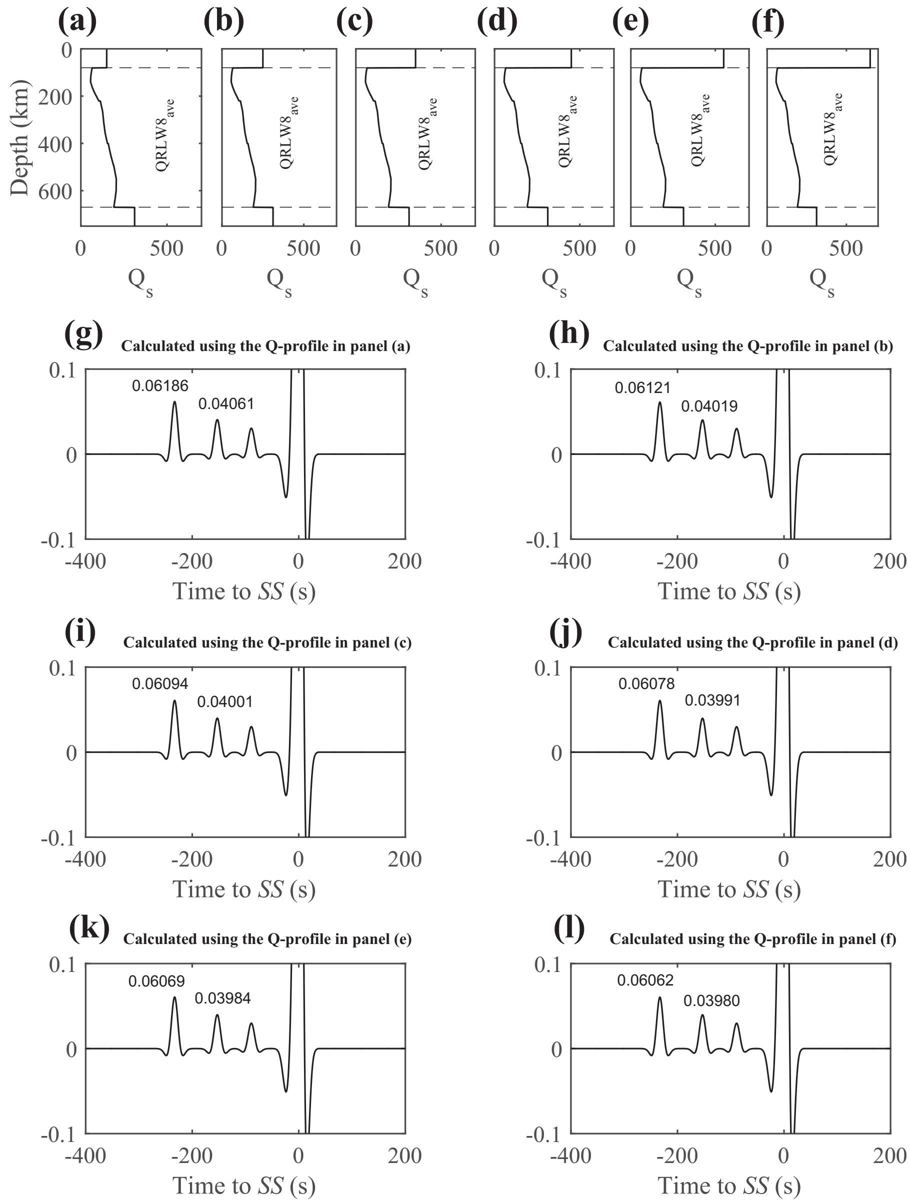

Figure A.1: Synthetic *SS* precursor waveforms calculated using different attenuation models. The input attenuation structure is taken from PREM (Dziewonski & Anderson 1981), which is then replaced by the average of model QRLW8 for the NW Pacific subduction zones (Gung & Romanowicz 2004) at depths from 80 to 670 km. In the depth range from 0 to 80 km, constant Q values starting from 150 (corresponding to the slow mantle wedge) up to 650 (corresponding to the fast subducting slab) at increments of 100 are employed (panels a to f). The synthetic *SS* precursor waveforms in panels (g) to (l) are calculated using the corresponding attenuation models in panels (a) to (f), respectively, and PREM density and shear wave velocity models. The reflection amplitudes of the *S410S* and *S660S* phases, normalized to that of *SS*, are also indicated for each synthetic waveform.

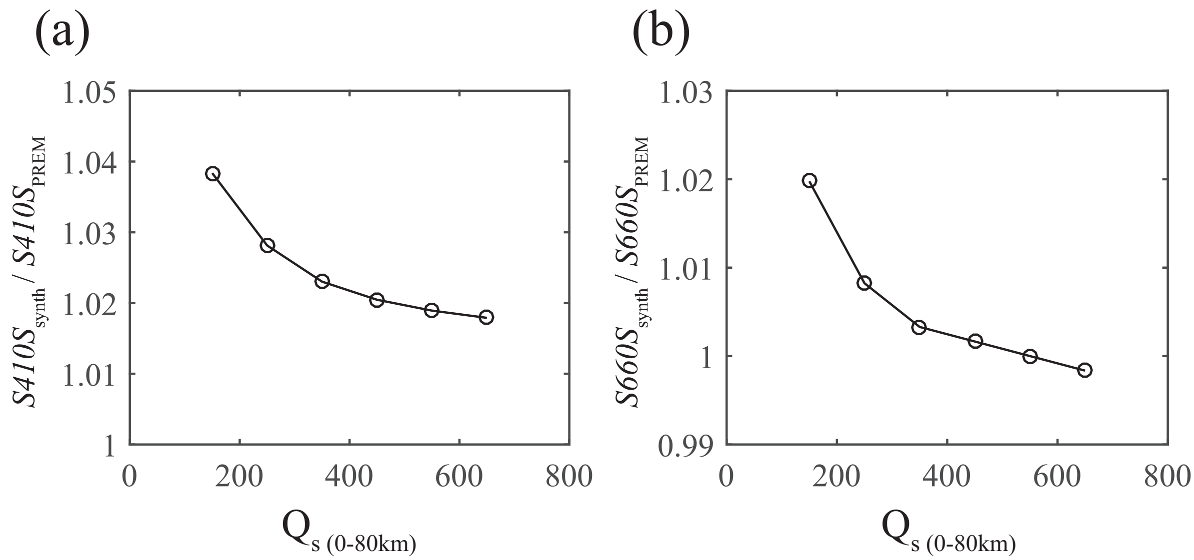

Figure A.2: Reflection amplitudes of (a) *S410S* and (b) *S660S* calculated for varying values of Q at shallower depths. The reflection amplitudes are normalized to those of calculated form PREM to examine the effect of deviation from PREM on the reflection amplitudes and consequently on the inverted shear velocities. The amplitudes of precursors decrease with increasing Q values. The results show absolute increases of up to 4% and 2% for the amplitudes of *S410S* and *S660S*, respectively. Based on the theoretical calculations, these translate into the velocity perturbation of 0.13% (or less). In other words, the velocity at the discontinuity depth has to decrease by 0.13% (or less) to account for the effect of high attenuating mantle wedge.

Appendix B
Challenges in the Application of SSA

To explore the robustness of SSA reconstruction under different conditions, we conduct three additional synthetic experiments. In the first experiment, we apply a 5 s time shift to a few selected traces (the dashed box in Figure B.1 indicates the time-shifted input traces) and reconstruct the entire data-set using scaling parameter (α) ranging from 0.2 to 0.6 (see Figures B.1b-B.1g). As expected from the Equation 7, a reduction in α lowers the dependency of the reconstructed data on the input data and the linearity of the move-out curve increases as α decreases (see Figure B.1). In other words, a subjective choice of parameter α can have noticeable effects on the quality of the reconstruction. Due to the uncertainties associated with the arrival times of long-period waves and their timing corrections (e.g., for surface topography), fkdhn lga α value of 0.4 (adopted from the reconstructions of P-to-S conversions and SS precursors, see Figures 3.2 and 3.6) offers a reasonable compromise between reconstruction fidelity and simplicity.

To examine the effects of large amplitude arrivals in the vicinity of the data gap (Figure B.2), we perform SSA on a decimated seismic section using different values of α. The average recovered amplitudes of the missing traces (see Figures B.2c and B.2e) are up to 70% of the original amplitudes. To further gauge the effect of noise levels on SSA reconstruction, we construct a synthetic record section containing two linear events (with different velocities) that are contaminated by a spurious outlier (Figure B.3a). Then the input data are reconstructed using the first two largest singular values ($k = 2$) and $\alpha = 0.2$, 0.4, and 0.6 (see Figures B.3b-B.3d). The recovered amplitude of the outlier increases with α, reaching nearly 50% of the input at $\alpha = 0.6$. However, the effects of the outlier are local (i.e., minimal at other distances) in all cases, which suggest that localized, high-amplitude noise is unlikely to alter the main observations and interpretations.

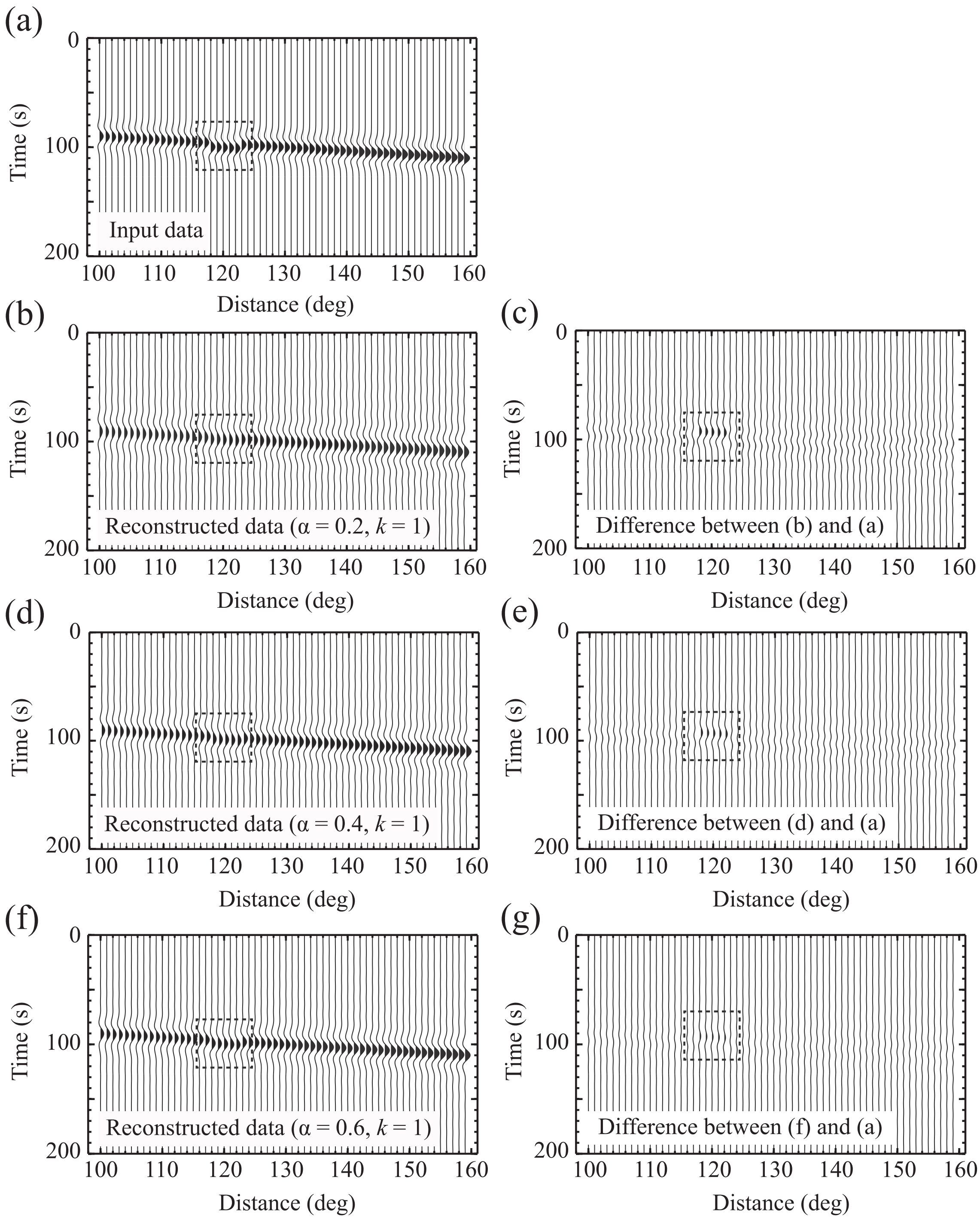

Figure B.1: Application of SSA when arrivals are locally delayed by 5 s. (a) Input data. (b), (d) and (f) Reconstructed data using $k = 1$ and $\alpha = 0.2$, 0.4, and 0.6, respectively. (c), (e) and (g) The corresponding differences between the reconstructed and input data. The dashed box outlines the time-shifted signals.

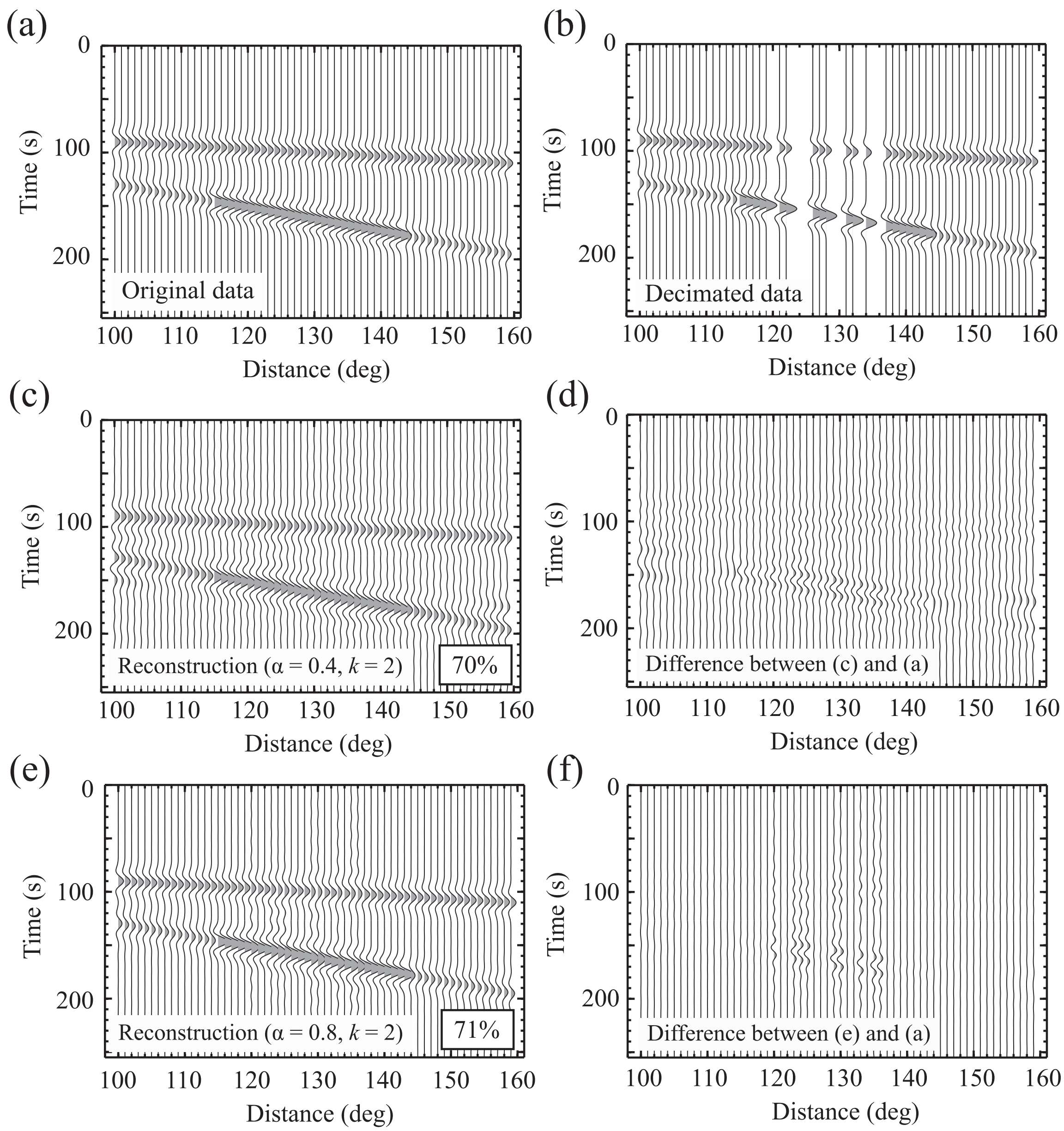

Figure B.2: Effect of large amplitude arrivals on the SSA interpolated data. (a) Original data consisting of two linear events. The steeper event shows higher amplitude signals in the middle of section. (b) Decimated input data. (c) and (e) Reconstructed images using $\alpha = 0.4$ and 0.8, respectively. Only the first two singular values are used to reconstruct the data. The average amplitude recovery of the missing traces is shown on the reconstructed sections. (d) and (f) Differences between the SSA interpolated and original data.

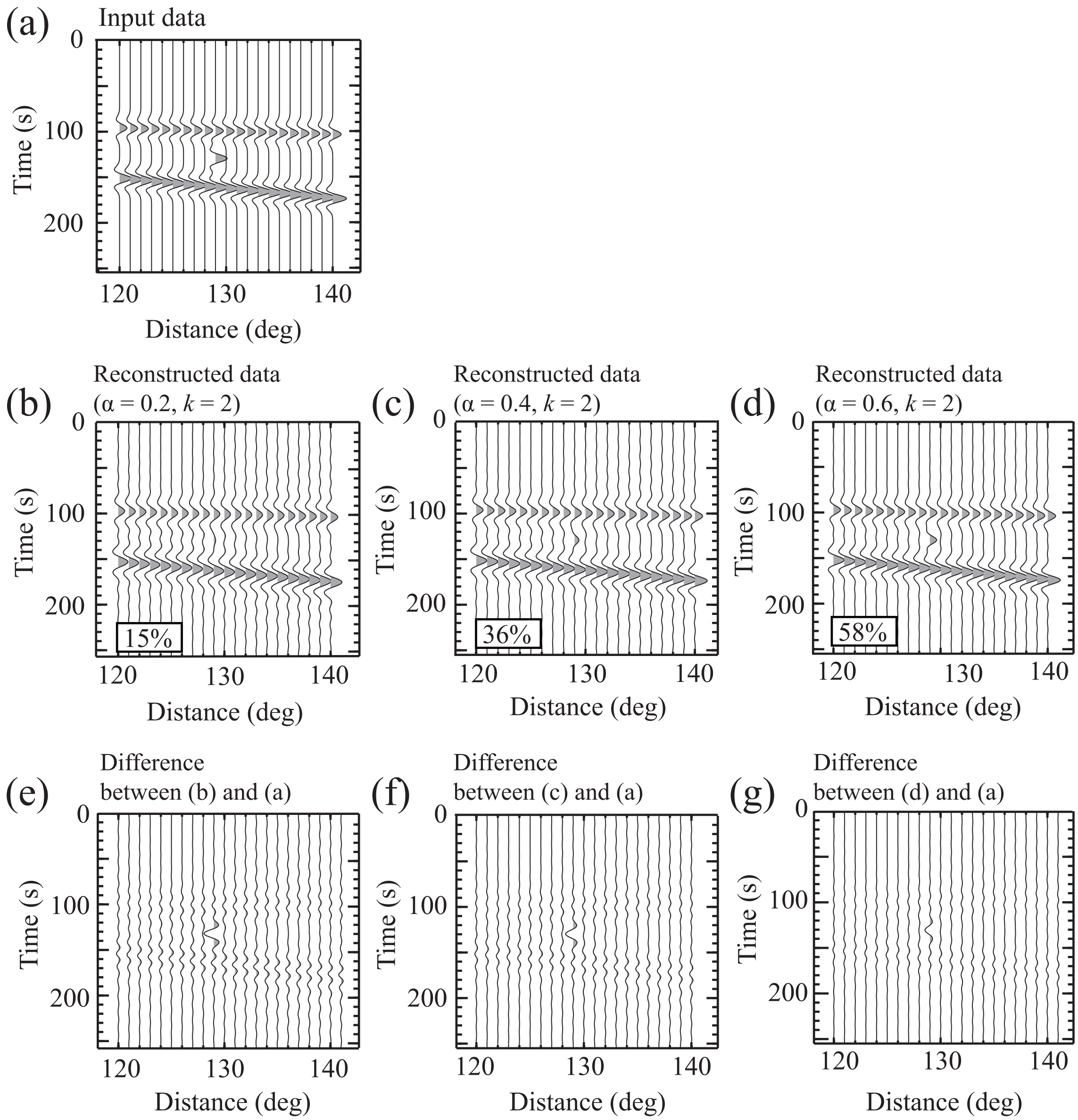

Figure B.3: Effect of a high amplitude outlier on the SSA reconstructed results. (a) Input section containing two linear events with a large amplitude outlier in between. (b), (c) and (d) The SSA interpolated sections using $k = 2$ and $\alpha = 0.2$, 0.4 and 0.6, respectively. The amplitude recovery of the input outlier is shown on the reconstructed sections. (e), (f) and (g) The corresponding differences between the interpolated and input data.